AD_____

GRANT NUMBER DAMD17-93-J-3003

TITLE: Wavelet Representation for Digital Mammography

PRINCIPAL INVESTIGATOR: Andrew F. Laine, D.Sc.

CONTRACTING ORGANIZATION: University of Florida
Gainesville, Florida 32611-6120

REPORT DATE: December 1995

TYPE OF REPORT: Annual

PREPARED FOR: Commander
U.S. Army Medical Research and Materiel Command
Fort Detrick, Frederick, Maryland 21702-5012

DISCLAIMER NOTICE

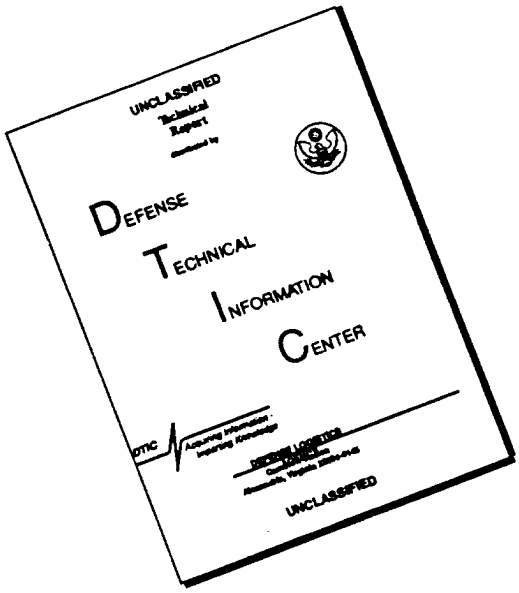

THIS DOCUMENT IS BEST QUALITY AVAILABLE. THE COPY FURNISHED TO DTIC CONTAINED A SIGNIFICANT NUMBER OF PAGES WHICH DO NOT REPRODUCE LEGIBLY.

REPORT DOCUMENTATION PAGE

Form Approved
OMB No. 0704-0188

1. AGENCY USE ONLY *(Leave blank)*	2. REPORT DATE	3. REPORT TYPE AND DATES COVERED
	December 1995	Annual (16 Nov 94 - 15 Nov 95)

4. TITLE AND SUBTITLE Wavelet Representation for Digital Mammography

5. FUNDING NUMBERS
DAMD17-93-J-3003

6. AUTHOR(S)
Andrew F. Laine, D.Sc.

7. PERFORMING ORGANIZATION NAME(S) AND ADDRESS(ES)
University of Florida
Gainesville, Florida 32611-6120

8. PERFORMING ORGANIZATION REPORT NUMBER

9. SPONSORING/MONITORING AGENCY NAME(S) AND ADDRESS(ES)
U.S. Army Medical Research and Materiel Command
Fort Detrick
Frederick, Maryland 21702-5012

10. SPONSORING/MONITORING AGENCY REPORT NUMBER

11. SUPPLEMENTARY NOTES

12a. DISTRIBUTION / AVAILABILITY STATEMENT
Approved for public release; distribution unlimited

12b. DISTRIBUTION CODE

13. ABSTRACT *(Maximum 200*

This report describes significant progress in the development of a methodology for accomplishing adaptive contrast enhancement by multiscale representations. Our studies have demonstrated that features extracted from multiresolution representations can provide an adaptive mechanism for the local emphasis of salient and subtle features of importance to mammography.

We show that subtle features characteristic of mammographic findings required a finer parameterization of scale space than provided by traditional methods of wavelet analysis carried out at dyadic scales.

The improved contrast of mammographic features make these techniques appealing for computed aided diagnosis (CAD) and screening mammography. Screening mammography examinations are certain to grow substantially in the next few years, and analytic methods that can assist general radiologists in reading mammograms shall be of great importance.

14. SUBJECT TERMS Breast Cancer, Mammography, Digital Image Processing, Multiscale Wavelet Analysis, Contrast Enhancement, Feature Extraction, Computer Aided Diagnosis.

15. NUMBER OF PAGES
130

16. PRICE CODE

17. SECURITY CLASSIFICATION OF REPORT	18. SECURITY CLASSIFICATION OF THIS PAGE	19. SECURITY CLASSIFICATION OF ABSTRACT	20. LIMITATION OF ABSTRACT
Unclassified	Unclassified	Unclassified	Unlimited

FOREWORD

Opinions, interpretations, conclusions and recommendations are those of the author and are not necessarily endorsed by the US Army.

__✓__ Where copyrighted material is quoted, permission has been obtained to use such material.

____ Where material from documents designated for limited distribution is quoted, permission has been obtained to use the material.

__✓__ Citations of commercial organizations and trade names in this report do not constitute an official Department of Army endorsement or approval of the products or services of these organizations.

____ In conducting research using animals, the investigator(s) adhered to the "Guide for the Care and Use of Laboratory Animals," prepared by the Committee on Care and Use of Laboratory Animals of the Institute of Laboratory Resources, National Research Council (NIH Publication No. 86-23, Revised 1985).

____ For the protection of human subjects, the investigator(s) adhered to policies of applicable Federal Law 45 CFR 46.

____ In conducting research utilizing recombinant DNA technology, the investigator(s) adhered to current guidelines promulgated by the National Institutes of Health.

____ In the conduct of research utilizing recombinant DNA, the investigator(s) adhered to the NIH Guidelines for Research Involving Recombinant DNA Molecules.

____ In the conduct of research involving hazardous organisms, the investigator(s) adhered to the CDC-NIH Guide for Biosafety in Microbiological and Biomedical Laboratories.

Andrea James 5/27/96

PI - Signature Date

Table of Contents

List of Figures

1 Introduction

Screen/film mammography is widely recognized as being the only effective imaging modality for the early detection of breast cancer in asymptomatic women [1]. Screening asymptomatic women using screen/film mammography has been shown to significantly reduce breast cancer mortality [2].

Breast cancer currently accounts for 32 % of cancer incidence and 18 % of cancer mortality for women in the United States. There were 182,000 new cases of breast cancer in the United States in 1993 and 46,000 deaths. Five year survival rates are generally very high (93 %) for breast cancer staged as being localized, falling to 72 % for regional disease and only 18 % for distant disease [3]. The early detection of breast cancer is clearly a key ingredient of any strategy designed to reduce breast cancer mortality.

Major advances in screen/film mammography have occurred over the past decade [4] which have resulted in significant improvements in image resolution and film contrast. Of major importance is that these improvements have been achieved at reduced radiation doses. Despite these advances, however, screen/film mammography remains a diagnostic imaging modality where image interpretation remains very difficult. Breast radiographs are generally examined for the presence of malignant masses and indirect signs of malignancy such as the presence of microcalcifications and skin thickening. Unfortunately, it is unlikely that major improvements in imaging performance will be achieved by technical advances in screen/film radiography alone.

The major reason for poor visualization of small malignant masses is the minor difference in x-ray attenuation between normal glandular tissues and malignant disease [5]. This fact makes the detection of small malignancies problematical, especially in younger women who have denser breast tissue. Although calcifications have high inherent attenuation properties, their small size also results in a low subject contrast [6]. As a result, the visibility of small tumors, and any associated microcalcifications, will always be a problem in mammography as it is currently performed using analog film.

Improvements in the ability of screen/film mammography to detect small tumors and microcalcifications is more likely to occur by improving the visibility of these features. It has been suggested that as normally viewed, mammograms display only about 3 % of the information they detect! [7].

Our approach to feature analysis and classification is motivated in part by recently discovered biological mechanisms of the human visual system [8]. Both multiorientation and multiresolution are known features of the human visual system. There exist cortical neurons which respond specifically to stimuli within certain orientations and frequencies.

In this report we describe exciting new results accomplished during our third year of study. In addition, we have continued our efforts in the development of wavelet transforms that exploit orientation and frequency selectivity to make mammographic features more obvious through localized contrast gain. Below, we describe in executive summary, recent accomplishments related to the objectives stated in Phase III and Phase IV of our Statement of Work (SOW). The methodology, approach and experimental studies are reported in detail in the body of this report.

1.1 Overview of Contents

In the next section, we describe in detail our wavelet processing algorithms, experimental methods and example results obtained. In addition, we list and summarize publications of our researchers during the past year of our investigation.

We present our underlying criteria for designing a database of 105 abnormal cases which are used in the evaluation of our computer-based methods for enhancement, detection and analysis of masses. We take into consideration a number of issues related to image acquisition, image selection, and image annotation, and discuss how each of these points affects our design criteria.

We present a fast implementation of the discrete dyadic wavelet transform, which we have extensively used for the enhancement of digital mammograms [9, 10, 11, 12]. The algorithm takes advantage of symmetries of filter coefficients in the filter bank implementation of the transform, and of the symmetry of a mirror extended input signal. The described approach is not limited to image sizes that are powers of two, and therefore allows extraction of arbitrarily sized rectangular regions from digital mammograms. We derive a second derivative analog to Mallat's "first derivative of a spline" wavelet [13] and compute filter coefficients for a discrete filter bank implementation.

In our earlier report, a discrete dyadic wavelet transform was applied successfully for enhancement of mammographic features. This was an octave-based transform with its scales increasing as a power of 2, and had limited capability for charaterizing signal details at scales between two consecutive levels, including band-limited features, such as microcalcification clusters, spicular lesions, and circular (arterial) calcifications. To alleviate this problem, and to more reliably identify features while isolating noise through scale space, we have developed a sub-octave wavelet transform. This is a generalization of a dyadic wavelet transform and has a better time-frequency resolution for mammographic feature analysis. Our experimental results demonstrate advantages over traditional dyadic wavelet transforms for mammogram enhancement. We also describe a noise reduction mechanism to avoid amplifying noise, such as scatter or digitization noise, during image

enhancement processing.

Linear phase filters have proven advantageous in signal and image processing because they limit image artifacts. We applied complex Daubechies wavelets, with symmetric compact support, for extracting mammographic features. Also, we present a novel approach for denoising using complex Daubechies wavelets. We trace the evolution of features across distinct scales by their wavelet coefficients. By virtue of linear phase and dual representations of scaling functions, we show how noise can be removed while features preserved.

Most image processing and computer vision algorithms assume knowledge of the proper spatial scale in the image. We describe an automatic technique that adaptively sets the proper spatial scale based on the size of local features in an image. Our current implementation automatically determines the proper scale based on a dynamic system model (motivated by analog circuit concepts) that continuously searches scale space. In the discussion below, we discretize and oversample a scale space representation and perform an optimization over this finite set.

We show that regions corresponding to masses can be identified reliably through multiscale features of a continuous wavelet transform. In contrast to traditional methods of wavelet analysis, which compute transform coefficients at dyadic levels of scale, we show that subtle characteristics of mammographic features require a finer parameterization of scale space.

Next, in this report, we show the derivation of a scheme to calculate the wavelet transform for an arbitrary scale. In addition, closed contours of zero-crossing features are extracted from a continuous scale frame representation, providing precise spatial localization for supporting local processing such as segmentation and adaptive contrast enhancement.

Digital radiographs of mammographic features (fibrils and masses) within an RMI phantom were processed for demonstration. Our results show that a mass and fibril known to exist in the physical RMI phantom but not visible via traditional image processing techniques (including window and leveling, histogram equalization, contrast stretching, etc.) are made clearly visible after processing.

We present results of local enhancement experiments applying hard thresholding of wavelet coefficients. The images used were synthetically generated. Care was taken for realistic modeling of: i) noise, ii) Point Spread Function (blurring of the image), and iii) masses that may exist in a digital mammogram. Our enhancement techniques were assessed using both analytic and psychophysical methods.

2 Body

2.1 Database Development

2.1.1 Introduction

In this section we describe our strategy for the design of a database of digitized mammograms. The database can take a number of forms, from a simple structured file system to a content-addressable database providing intelligent access to the data. In order to determine the type of database to construct we took into consideration its utility in the scope of the project and the availability of local resources, as well as a number of issues related to image acquisition, image selection, and image annotation. Below, we discuss each of these points and how they affected our design criteria.

2.1.2 Motivation

The first step in designing an image database is determining its intended use, as this has direct impact on the database design criteria. Our motivation for the development of a database of digitized mammograms was the need for evaluating our computer-based methods for enhancement, detection, and analysis of mammographic abnormalities on representative cases.

2.1.3 Image Acquisition

Good quality mammograms are essential for the construction of a database of digitized mammograms. Kimme-Smith [14] suggests that as a minimum requirement, films for a database of digitized mammograms should be supplied by facilities accredited by the American College of Radiology (ACR). In addition, Rangayyan *et al.* [15] recommend that films should come from institutions such as teaching hospitals where audits of all aspects of mammography are performed on a regular basis.

In addition to quality mammograms, selection of a suitable spatial and contrast resolution is fundamental for the adequate acquisition of digitized mammograms. The digitizer has to be capable of measuring accurately the complete range of optical densities found in mammographic images. Nishikawa [16] recommends that the number of bits per pixel should be chosen so that image noise is adequately measured. A digitizer measuring optical densities in the range of 0.05–3.0 with 12 bits of quantization is generally accepted as a suitable choice [17, 18, 16].

The selection of acceptable spatial resolution for a digitizer depends on the underlying task, e.g., detection of microcalcifications and detection of masses. It is widely accepted

[17, 18, 16] that mammograms with microcalcifications should be digitized with a pixel size of 50 microns or smaller and mammograms with masses should be digitized with a pixel size of 100 microns or perhaps larger.

Other general recommendations are to digitize all cases on the same digitizer or on digitizers with identical or correctable characteristics [16] and to provide calibration data such as the transfer function from X-ray exposure to pixel values [18].

In our database, mammograms were digitized with a Lumiscan 75 scanner (Sunnyvale, California) at 116-micron pixel resolution, 12-bit gray scale resolution and optical density range of 0.05–3.00. Cases in our database were supplied by Shands Hospital at the University of Florida, an ACR accredited and FDA certified institution.

2.1.4 Image Selection and Annotation

It has been suggested by several researchers [19, 17, 16, 15] that a database which is to be used for enhancement, detection and analysis of mammographic abnormalities should contain a collection of images in which a wide range of variation of normal, benign and malignant conditions are adequately represented. In addition, a database of digitized mammograms should provide annotated images showing the location, and boundaries of all abnormalities [19, 17, 18, 16, 15]. Furthermore, cases in the database should be unequivocally categorized as normal or abnormal [18, 14, 16]. Abnormal cases, benign or malignant, can be obtained through biopsy [18, 14, 16]. Mammograms regarded as normal can be obtained by selecting cases for which it is known that no cancer has developed for two or more years following mammographic screening [18, 14, 16]. Image annotations should be made by multiple radiologists experienced in reading mammograms and a subjective evaluation of the detectability of the lesion should be provided [19, 16]. It has also been suggested [19] that annotations should be hierarchically organized, e.g., individual microcalcifications, clusters of microcalcifications, and the overall extent of the abnormality should all be recorded and related. Also, Astley [19] suggests that criteria for classifying images within the database be established and standardized, and recommends that radiographic projection, glandular pattern type, diagnosis, size, location and subtlety of abnormalities be included as part of such criteria.

Another issue of importance is the views that should be stored in the database. In standard mammographic screening, a case consists of two views of each breast (craniocaudal (CC) and mediolateral oblique (MLO)), for a total of four images. There is considerable evidence that the combination of the craniocaudal view and the mediolateral oblique projection detect more cancers than a single view [20]. In fact, two views per breast are the only accepted norm in the United States. Two views per breast allow for the

detection of cancer through right/left asymmetry and/or the confirmation or dismissal of cancer by finding its presence in the other view. Researchers [17, 21, 16, 15] have recognized that computer algorithms for the detection of mammographic abnormalities must use more than a single view and that a practical mammography database ought to contain at least the four views of a standard mammographic screening exam and perhaps previous and subsequent examinations of the same patient.

Consideration must also be given to the distribution of normal, benign, and malignant occurrences within the database [14, 16, 15]. Nishikawa [16] recommends that in a mammography database the number of normal cases should approximately be the same as the number of cases for each lesion type. Also, within each lesion category, there should be approximately an equal number of benign and malignant cases.

As a starting point we have confined the lesion type to masses (mainly due to the pixel resolution (116 microns) of our scanner and constructed a database of 105 abnormal cases (420 images) with a total of 118 biopsy proven masses. Following the recommendations outlined above we have established criteria for including cases in the database based on the American College of Radiology Breast Imaging Reporting and Data System (ACR-BIRADS). Cases are included according to the location, shape, margins, density, size, and surrounding glandular pattern of the underlying abnormality, and the mammography finding (screening assessment), and diagnosis (biopsy), see Figure 1. This information allows us to retrieve cases that have similar characteristics in terms of location, lesion appearance and diagnosis. We have annotated all abnormalities using `XMam` (see Figure 2) with the assistance of a radiologist experienced in reading mammograms and included a subjective evaluation of the detectability of each lesion based on the following scale:

1. Extremely subtle: Dense or heterogeneously dense tissue with the margins of the mass not visible. Asymmetry or architectural distortion may be present.

2. Very subtle: Dense or heterogeneously dense tissue with the margins of the mass partially visible on one view.

3. Subtle: Heterogeneously dense with the margins of the mass partially visible. Calcifications may or may not be present.

4. Relatively obvious: Heterogeneously dense with all margins of the mass visible or clustered microcalcifications present with margins of the mass only partially visible.

5. Obvious: Fatty tissue with all margins of the mass easily visible on two views.

MAM___ (Age___)

Right	Left
Location: 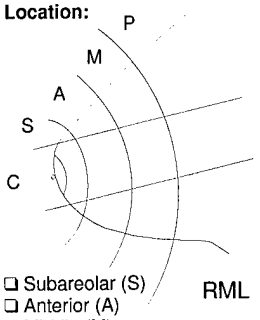 ❑ Subareolar (S) ❑ Anterior (A) ❑ Middle (M) ❑ Posterior (P) ❑ Central (C) RML 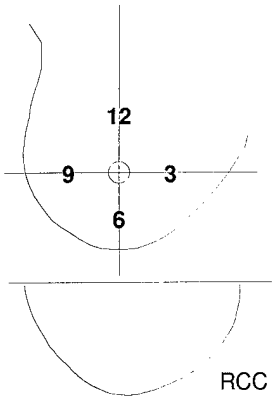 RCC	**Location:** 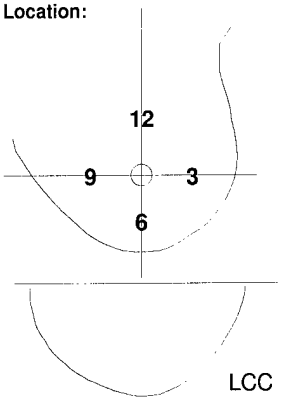 LCC 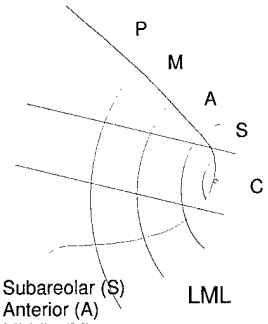 ❑ Subareolar (S) ❑ Anterior (A) ❑ Middle (M) ❑ Posterior (P) ❑ Central (C) LML
Shape: ❑ Round (R) ❑ Oval (O) ❑ Lobulated (L) ❑ Irregular (I) **Margins:** ❑ Circumscribed Well-defined (D) ❑ Microlobulated (M) ❑ Indistinct or Ill-defined (I) ❑ Obscured (O) ❑ Spiculated (S) **Density:** ❑ High (+) ❑ Equal (=) ❑ Low (-) ❑ Fat containing Radiolucent (0) **Size:** ____ (mm) **Surrounding Tissue Density:** ❑ Fatty ❑ Scattered Fibroglandular Densities ❑ Heterogeneously Dense ❑ Extremely Dense	**Mammography Finding:** ❑ Negative (N) ❑ Benign (B) ❑ Probably Benign (P) ❑ Suspicious (S) ❑ Malignancy (M) **Biopsy:** ❑ Benign (B) ❑ Malignancy (M) **Microcalcifications:** ❑ Present ❑ Not Present **Palpable:** ❑ Yes ❑ No **Comments:** _____ _____ _____
Shape: ❑ Round (R) ❑ Oval (O) ❑ Lobulated (L) ❑ Irregular (I) **Margins:** ❑ Circumscribed Well-defined (D) ❑ Microlobulated (M) ❑ Indistinct or Ill-defined (I) ❑ Obscured (O) ❑ Spiculated (S) **Density:** ❑ High (+) ❑ Equal (=) ❑ Low (-) ❑ Fat containing Radiolucent (0) **Size:** ____ (mm) **Surrounding Tissue Density:** ❑ Fatty ❑ Scattered Fibroglandular Densities ❑ Heterogeneously Dense ❑ Extremely Dense	**Mammography Finding:** ❑ Negative (N) ❑ Benign (B) ❑ Probably Benign (P) ❑ Suspicious (S) ❑ Malignancy (M) **Biopsy:** ❑ Benign (B) ❑ Malignancy (M) **Microcalcifications:** ❑ Present ❑ Not Present **Palpable:** ❑ Yes ❑ No **Comments:** _____ _____ _____

Figure 1: Case characterization form.

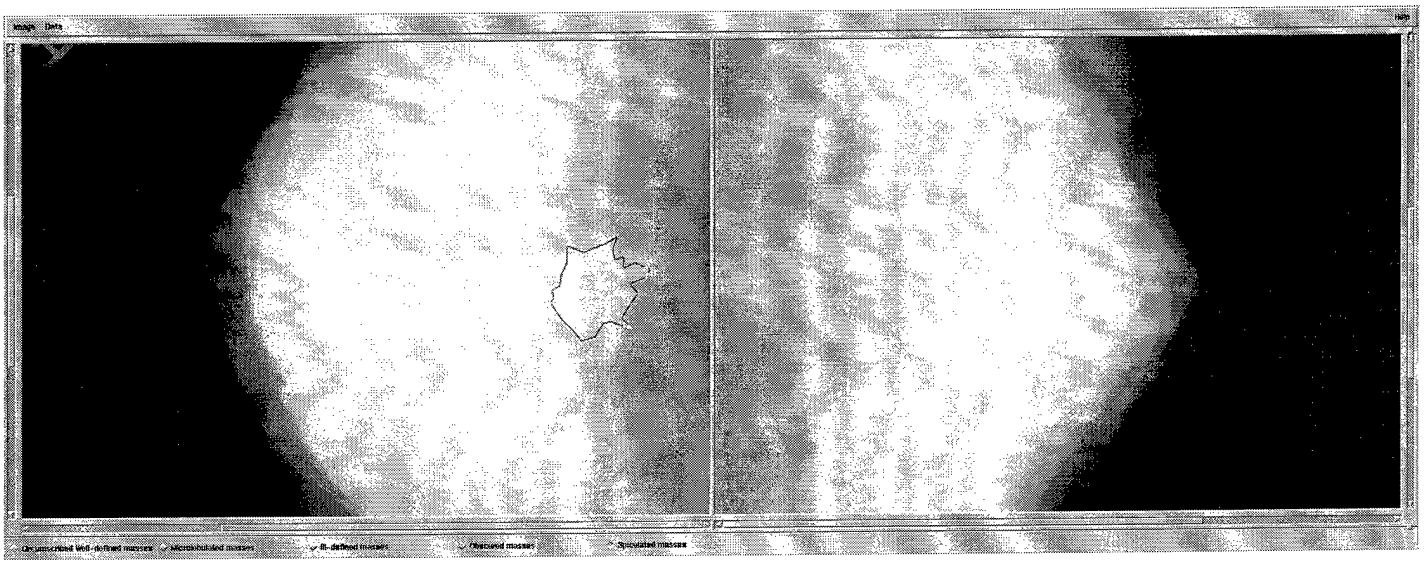

CC window

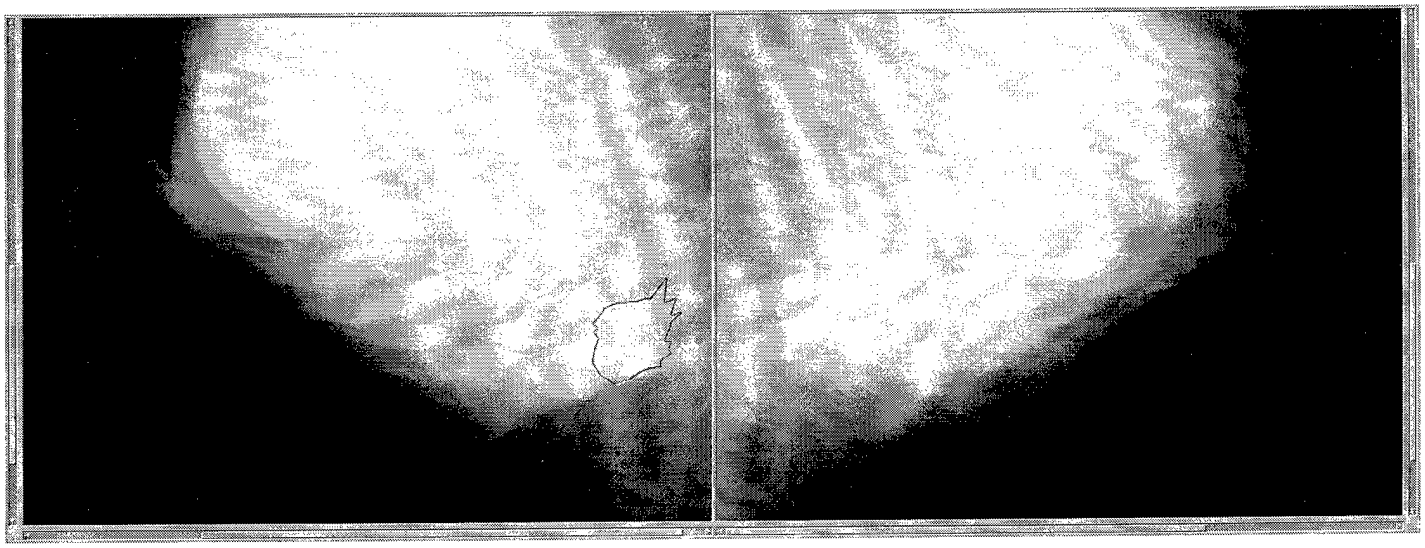

MLO window

Figure 2: XMam showing a malignant tumor with spiculated margins.

Using XMam capabilities, annotations were organized hierarchically by recording individual masses on each view and relating instances of the same mass across views.

Currently our database consists of 78 malignant masses (66.1 %) and 40 benign masses (33.9 %) distributed according to subtlety as follows: 28.8 % obvious, 28 % relatively obvious, 25.4 % subtle, 14.4 % very subtle, and 3.4 % extremely subtle. During the current year we will collect more cases in the very subtle and extremely subtle categories as well as cases of normal mammographic occurrences.

2.1.5 Summary

We have described some underlying criteria to be followed when designing a database of digitized mammograms. Respecting these criteria we constructed a database of 105 abnormal cases (420 images) with a total of 118 biopsy proven masses. All cases were supplied by Shands Hospital at the University of Florida, an ACR accredited and FDA certified institution. Mammograms were digitized with a Lumiscan 75 scanner (Sunnyvale, California) at 116-micron pixel resolution, 12-bit gray scale resolution and optical density range of 0.05–3.00. All abnormalities were annotated hierarchically by a radiologist from Shands Hospital experienced in reading mammograms using an inhouse tool called XMam described previously in our 1994 annual report. Annotations include the location, shape, margins, density, size, surrounding glandular pattern, mammography finding and diagnosis based on the standardized American College of Radiology Breast Imaging Reporting and Data System. In addition, we developed a subjective evaluation of the detectability of a lesion and evaluated all lesions based on this scale. The current database consists of 78 malignant masses (66.1 %) and 40 benign masses (33.9 %) distributed according to subtlety as follows: 28.8 % obvious, 28 % relatively obvious, 25.4 % subtle, 14.4 % very subtle, and 3.4 % extremely subtle.

2.2 A Discrete Dyadic Wavelet Transform Implementation

2.2.1 Introduction

Discrete non-redundant wavelet transforms have been successfully applied previously in image compression applications [22, 23]. However, existing problems in the analysis of medical signals and images motivate the use of redundant wavelet decompositions presented in this report.

The discrete dyadic wavelet transform discussed below is one example of a redundant representation. As originally proposed, the wavelet was a first derivative of a smoothing function, and was used as a multiscale edge detector to obtain a translation-invariant

representation consisting of edges [13]. A reconstruction algorithm to approximate an original signal from its multiscale edge coefficients alone was described in [13, 24].

In comparison, our previous work [9, 10, 11, 12] made no attempt to obtain a parsimonious representation from a discrete dyadic wavelet transform. Rather, the transform was intentionally highly redundant. This redundancy was exploited for image enhancement by modifying the transform coefficients and reconstructing. Here, we describe an efficient implementation of the discrete dyadic wavelet transform, in which we present a tool for contrast enhancement in digital mammography.

When digital filtering of a finite-duration discrete signal is performed via circular convolution the filter will act on both ends of the signal simultaneously. This may lead to artifacts near both ends of the result. In image processing, mirror extension of an input signal is a very popular method for alleviating such boundary effects. Here, we present a fast filter bank implementation of the discrete dyadic wavelet transform which takes advantage of the fact that the input signal to the filter bank is mirror extended. For clarity, we describe both one and two-dimensional transforms. An extension to higher dimensions is given in [25].

2.2.2 One-Dimensional Discrete Dyadic Wavelet Transform

A discrete wavelet transform is obtained from a continuous representation by discretizing dilation and translation parameters such that the resulting set of wavelets constitutes a *frame*. The dilation parameter is typically discretized by fixed dilation steps and the translation parameter by integer multiples of a fixed step [26]. Unfortunately, the resulting transform is variant under translations, a property which makes it less attractive for the analysis of signals, including digital mammography.

Sampling the translation parameter with the same sampling period as the input function results in a translation-invariant, but redundant representation. The dyadic wavelet transform proposed by Mallat and Zhong [13] is one such representation. Let us begin with a brief review of the properties of a dyadic wavelet transform as described in [13], included here for completeness.

The dyadic wavelet transform of a function $f(x) \in L^2(\boldsymbol{R})$ is defined as a sequence of functions

$$\{W_m f(x)\}_{m \in \boldsymbol{Z}},$$

where $W_m f(x) = f * \psi_m(x) = \int_{-\infty}^{\infty} f(t)\, \psi_m(x-t)\, dt$, $\psi(x)$ is a wavelet, and $\psi_m(x) = 2^{-m}\psi(2^{-m}x)$ is a wavelet expanded by a dilation parameter (or scale) 2^m. Note the use of convolution instead of an inner product.

To ensure coverage of the frequency axis the requirement on the Fourier transform of $\psi_m(x)$ is the existence of $A_1 > 0$ and $B_1 < \infty$ such that

$$A_1 \leq \sum_{m=-\infty}^{\infty} |\hat{\psi}(2^m\omega)|^2 \leq B_1$$

is satisfied almost everywhere. The constraint on the Fourier transform of the (nonunique) reconstructing function $\chi(x)$ is [13]

$$\sum_{m=-\infty}^{\infty} \hat{\psi}(2^m\omega)\,\hat{\chi}(2^m\omega) = 1.$$

A function $f(x)$ can then be completely reconstructed from its dyadic wavelet transform using the identity

$$f(x) = \sum_{m=-\infty}^{\infty} W_m f * \chi_m(x),$$

where $\chi_m(x) = 2^{-m}\chi(2^{-m}x)$.

In our application, processing is performed on discrete rather than continuous functions. When the function to be transformed is in the discrete form, the scale 2^m can no longer vary over all $m \in \boldsymbol{Z}$; a finite sampling rate constrains the window size from being arbitrarily small, while computational resources may restrict the use of an arbitrarily large window. Let the finest scale be normalized to 1 and the coarsest scale be set to 2^M.

The smoothing of a function $f(x) \in L^2(\boldsymbol{R})$ is defined as

$$S_m f(x) = f * \phi_m(x),$$

where $\phi_m(x) = 2^{-m}\phi(2^{-m}x)$ with $m \in \boldsymbol{Z}$, and $\phi(x)$ is a smoothing function (i.e., its integral is equal to 1 and $\phi(x) \to 0$ as $|x| \to \infty$ [13]).

In Mallat *et al.* [13], a purely real smoothing function $\phi(x)$ was selected, whose Fourier transform satisfied

$$|\hat{\phi}(\omega)|^2 = \sum_{m=1}^{\infty} \hat{\psi}(2^m\omega)\,\hat{\chi}(2^m\omega). \tag{1}$$

In addition, it was shown that any discrete function of finite energy ($g(n) \in l^2(\boldsymbol{Z})$) can be written as the uniform sampling of some function smoothed at scale 1, i.e., $g(n) = S_1 f(n)$, where $f(x) \in L^2(\boldsymbol{R})$ is not unique. Thus, the discrete dyadic wavelet transform of $S_1 f(n)$ for any coarse scale 2^M is defined as a sequence of discrete functions

$$\{S_M f(n+s), \{W_m f(n+s)\}_{m\in[1,M]}\}_{n\in\boldsymbol{Z}},$$

where s is a $\psi(x)$ dependent sampling shift.

For a certain choice of wavelets the discrete dyadic wavelet transform can be implemented within a fast hierarchical digital filtering scheme. Next, we will summarize the relations between filters, wavelets, and smoothing functions.

The Fourier transform of $\phi(x)$ must satisfy [13]

$$\hat{\phi}(\omega) = e^{-j\omega s} \prod_{k=1}^{\infty} H(2^{-k}\omega), \tag{2}$$

where j stands for $\sqrt{-1}$, the lowpass filter frequency response $H(\omega)$ is differentiable, and

$$|H(\omega)|^2 + |H(\omega + \pi)|^2 \leq 1 \text{ with } |H(0)| = 1.$$

Computing Equation 1 for the finest two scales shows that

$$\hat{\psi}(2\omega)\, \hat{\chi}(2\omega) = |\hat{\phi}(\omega)|^2 - |\hat{\phi}(2\omega)|^2, \tag{3}$$

while computing Equation 2 for $\hat{\phi}(2\omega)$ yields

$$\hat{\phi}(2\omega) = e^{-j\omega s} H(\omega)\, \hat{\phi}(\omega). \tag{4}$$

If we choose

$$\hat{\psi}(2\omega) = e^{-j\omega s} G(\omega)\, \hat{\phi}(\omega) \tag{5}$$

and

$$\hat{\chi}(2\omega) = e^{j\omega s} K(\omega)\, \hat{\phi}^*(\omega), \tag{6}$$

where $G(\omega)$ and $K(\omega)$ are digital filter frequency responses, "$*$" denotes complex conjugation, and insert Equations 4, 5, 6 into Equation 3 we observe a relation between the filter frequency responses [13],

$$|H(\omega)|^2 + G(\omega)K(\omega) = 1. \tag{7}$$

Now we are in position to choose filters that will give rise to wavelets and scaling functions for a discrete dyadic wavelet transform. Filters that are associated with a compactly supported orthonormal wavelet basis are certainly a possible choice. However, other choices, as described below, provide distinct advantages for the analysis of digital mammograms.

Suppose we seek a wavelet such that it is compactly supported, antisymmetric or symmetric, exhibits good edge detection capability (i.e., equivalent to a first or a second derivative of some smoothing function), and is as regular as possible. With these additional constraints, orthonormal wavelet bases are almost completely ruled out (the Haar basis being the exception).

In [10, 11], Laine *et al.* proposed an extension to the family of filters described in [13]. In this design, the wavelet could be either antisymmetric and equal to the first derivative of some smoothing function $\theta(x)$, or symmetric and equal to the second derivative of $\theta(x)$.

When the wavelet $\psi(x)$ is antisymmetric around zero (i.e., an odd function) $e^{-j\omega s}G(\omega)$ is an odd imaginary function, and when the wavelet $\psi(x)$ is symmetric around zero (i.e., an even function) $e^{-j\omega s}G(\omega)$ is an even real function. The function $e^{-j\omega s}H(\omega)$ is even and real in both cases.

For the wavelet $\psi(x)$ to be the first (second) derivative of some smoothing function $\theta(x)$, $\hat{\psi}(\omega)$ must have a first-order (second-order) zero at $\omega = 0$, and, therefore, $G(\omega)$ must have a first-order (second-order) zero at $\omega = 0$.

However, even after satisfying all of the above constraints there remains a large number of possible choices for $H(\omega)$. In [10], the class of filters from [13] was extended by choosing

$$H(\omega) = e^{j\frac{\omega}{2}p}\left(\cos\left(\frac{\omega}{2}\right)\right)^{2n+p}, \tag{8}$$

where $2n+p \in \boldsymbol{N}$, $n \in \boldsymbol{Z}$, and $p \in \{0,1\}$. Once $H(\omega)$ is chosen, the product $G(\omega)K(\omega)$ is constrained by Equation 7. For example, choosing

$$G(\omega) = e^{j\frac{\omega}{2}p}\left(4j\sin\left(\frac{\omega}{2}\right)\right)^{2-p} \tag{9}$$

determines

$$K(\omega) = -\frac{1}{16}\left(e^{-j\omega}G(\omega)\right)^{p}\sum_{l=0}^{2n+p-1}\left(\cos\left(\frac{\omega}{2}\right)\right)^{2l}. \tag{10}$$

Note that $H(\omega)$ is a lowpass filter, $G(\omega)$ a highpass filter, and $K(\omega)$ a highpass filter for $p = 1$ and a lowpass filter when $p = 0$.

The filters described in Equations 8 through 10 are finite impulse response (FIR) filters. For implementation, Table 1 and Table 2 list the filter coefficients for the cases $2n+p \in \{1,2\}$ and $2n+p \in \{3,4\}$, respectively.

	$n=0,\ p=1$			$n=1,\ p=0$		
m	h	g	k	h	g	k
-1	0.5	2		0.25	4	-0.015625
0	0.5	-2	-0.125	0.5	-8	-0.09375
1			0.125	0.25	4	-0.015625

Table 1: Impulse responses of filters $H(\omega)$, $G(\omega)$, and $K(\omega)$ for $2n+p \in \{1,2\}$.

For the wavelet to be symmetric/antisymmetric around zero, the sampling shifts for this family of filters must be equal to $\frac{p}{2}$.

	$n=1,\ p=1$			$n=2,\ p=0$		
m	h	g	k	h	g	k
-3						-0.0009765625
-2	0.125		-0.0078125	0.0625		-0.009765625
-1	0.375	2	-0.0546875	0.25	4	-0.0458984375
0	0.375	-2	-0.171875	0.375	-8	-0.13671875
1	0.125		0.171875	0.25	4	-0.0458984375
2			0.0546875	0.0625		-0.009765625
3			0.0078125			-0.0009765625

Table 2: Impulse responses of filters $H(\omega)$, $G(\omega)$, and $K(\omega)$ for $2n+p \in \{3,4\}$.

By inserting Equation 8 into Equation 2 and using $\prod_{k=1}^{\infty} \cos(2^{-k}\omega) = \frac{\sin\omega}{\omega}$ we can obtain

$$\hat{\phi}(\omega) = \left(\frac{\sin(\frac{\omega}{2})}{\frac{\omega}{2}}\right)^{2n+p},$$

while by applying Equation 9 and Equation 5 we see that

$$\hat{\psi}(\omega) = (j\omega)^{2-p}\left(\frac{\sin(\frac{\omega}{4})}{\frac{\omega}{4}}\right)^{2n+2}.$$

Thus, the wavelet $\psi(x)$ is a first ($p=1$) or a second ($p=0$) derivative of a smoothing function $\theta(x)$, whose Fourier transform is

$$\hat{\theta}(\omega) = \left(\frac{\sin(\frac{\omega}{4})}{\frac{\omega}{4}}\right)^{2n+2}.$$

Note that $\theta(x)$ is a spline of degree $2n+1$. By increasing n, $\hat{\theta}(\omega)$ becomes more localized in the frequency domain and has larger support in the spatial domain.

For exposition, Figure 3 shows $\theta(x)$ for $n \in \{0,1,2\}$ and the corresponding wavelets $\psi(x)$ for $2n+p \in \{1,2,3,4\}$. With the exception of the Haar wavelet ($2n+p=1$), these wavelets are not orthogonal in the sense that their binary dilations and dyadic translations generate a basis of $L^2(\boldsymbol{R})$. Their regularity order is $2n+p-1$ (i.e., $\psi(x) \in C^{2n+p-1}$).

Similar to orthogonal and biorthogonal discrete wavelet transforms [26], the discrete dyadic wavelet transform can be implemented within a hierarchical filtering scheme. Using the definition of the discrete dyadic wavelet transform along with Equations 4 and 5 we can formulate the analysis section of such a filter bank. The synthesis section simply follows from Equation 7. Suppose

$$F_s(\omega) = e^{-j\omega s}F(\omega), \tag{11}$$

where $F(\omega)$ is either $H(\omega)$, $G(\omega)$, or $K(\omega)$ (Equations 8 through 10). We may then construct a filter bank implementation of the discrete dyadic wavelet transform as shown in Figure 4.

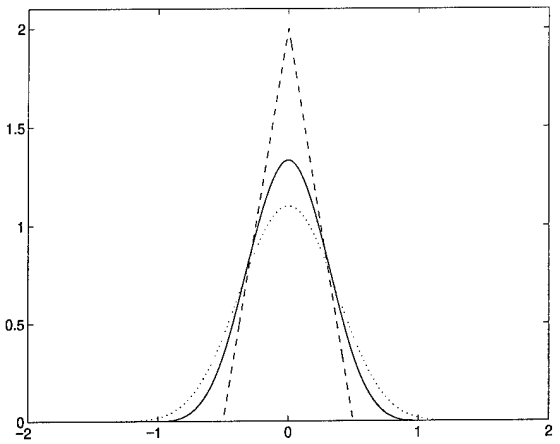

(a)

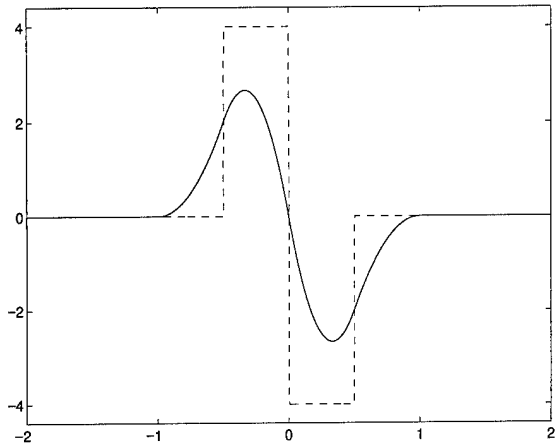

(b)

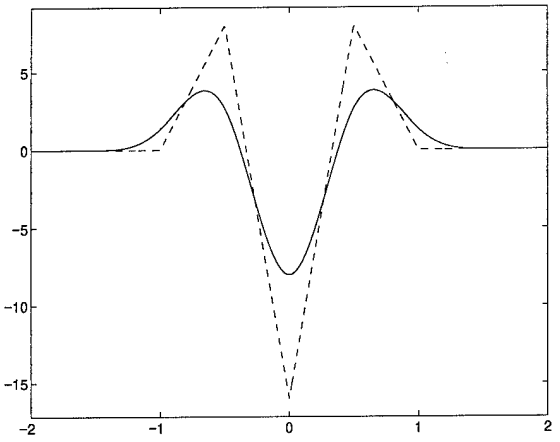

(c)

Figure 3: (a) Primitives $\theta(x)$: piecewise linear spline (dashed), cubic spline (solid), and quintic spline (dotted); (b) wavelets $\psi(x) = \frac{d\theta(x)}{dx}$: the first derivative of the piecewise linear spline (dashed) and the first derivative of the cubic spline (solid); (c) wavelets $\psi(x) = \frac{d^2\theta(x)}{dx^2}$: the second derivative of the cubic spline (dashed) and the second derivative of the quintic spline (solid).

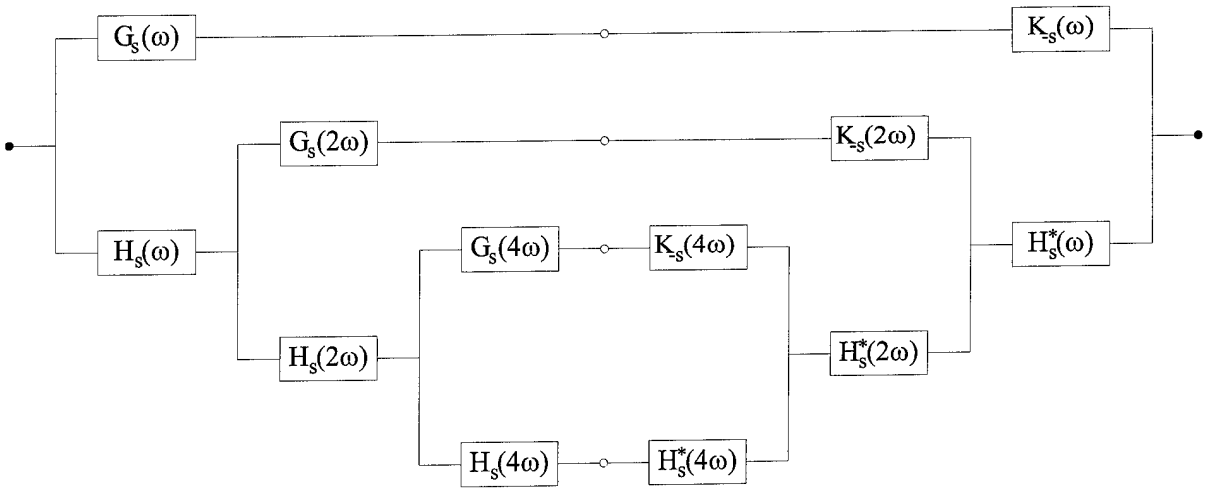

Figure 4: Filter bank implementation of a one-dimensional discrete dyadic wavelet transform decomposition (left) and reconstruction (right) for three levels of analysis. $H_s^*(\omega)$ denotes the complex conjugate of $H_s(\omega)$.

Filters referred to in Equations 8 through 10 at level $m+1$ (i.e., filters applied at some scale 2^m) become $F(2^m\omega)$, where $F(\omega)$ denotes any of the three filters at level 1. In the spatial domain this is equivalent to upsampling the filter impulse response by 2^m (i.e., inserting $2^m - 1$ zeros between subsequent filter coefficients at level 1). Noninteger shifts at level 1 for the class of filters with $p = 1$ are rounded to the nearest integer. An implementation with upsampling of filter impulse responses (called "algorithme à trous") was first proposed by Holschneider *et al.* [27]. The complexity of such a filter bank implementation increases linearly with the number of levels.

Let us refer to the filters at level 1 (Equations 8 through 10) as "original filters," to distinguish them from their upsampled versions. Let an input signal $x(n)$ be real, $x(n) \in l^1(\boldsymbol{Z})$, $n \in [0, N-1]$, and let $X(\omega)$ be its Fourier transform. Depending on the length of each filter impulse response, filtering an input signal may be computed either by multiplying $X(\omega)$ by a filter frequency response or by circularly convolving $x(n)$ with a filter impulse response. Of course, such a periodically extended signal may change abruptly at the boundaries causing artifacts. A common remedy for such a problem is realized by constructing a mirror extended signal

$$x_{me}(n) = \begin{cases} x(-n-1) & \text{if } n \in [-N, -1], \\ x(n) & \text{if } n \in [0, N-1], \end{cases} \tag{12}$$

where we chose the signal $x_{me}(n)$ to be supported in $[-N, N-1]$. As will be evident shortly, mirror extension is particularly elegant in conjunction with symmetric/antisymmetric filters.

Let us first classify symmetric/antisymmetric real even-length signals into four types [28]:

$$\textbf{Type I}\ \ f(n) = f(-n),$$

$$\textbf{Type II}\ \ f(n) = f(-n-1),$$

$$\textbf{Type III}\ \ f(n) = -f(-n),$$

$$\textbf{Type IV}\ \ f(n) = -f(-n-1),$$

where $n \in [-N, N-1]$. Note that for Type I signals the values at $f(0)$ and $f(-N)$ are not paired with any other value, and that for Type III signals the values at $f(0)$ and $f(-N)$ are equal to zero.

Using properties of the Fourier transform it is easy to show that the convolution of symmetric/antisymmetric real signals results in a symmetric/antisymmetric real signal. If a symmetric/antisymmetric real signal has an even length, then there always exists an integer shift such that the shifted signal belongs to one of the above types.

Next we examine the filter bank implementation of a one-dimensional discrete dyadic wavelet transform (Figure 4) with filters derived from Equations 8 through 10 driven by a mirrored signal $x_{me}(n)$ at the input. Let the number of levels M be restricted by

$$M \ \leq\ \log_2 \frac{4N-2}{R_{max}-1}, \tag{13}$$

where R_{max} is the length of the longest "original" filter impulse response.

Each block in the filter bank consists of a filter and a circular shift operator (Equation 11). Equation 13 guarantees that the length of the filter impulse response does not exceed the length of the signal at each block.

Since an input signal $x_{me}(n)$ is of Type II and noninteger shifts at level 1 are rounded to the nearest integer, it follows that a processed signal at any point in the filter bank belongs to one of the types defined above. This means that filtering a signal of length $2N$ can be reduced to filtering a signal of approximately one half of its length. (For Types I and III, $N+1$ samples are needed. However, for Type III one needs to store only $N-1$ values because of zero values always stored at the zeroth and $(-N)$-th position sample).

Implementation is particularly simple for filters designed with $p = 0$ (Equations 8 through 10). Filters are of Type I in this case, so the signal at any point of the filter bank will be of Type II. A block from the filter bank shown in Figure 4 (Equation 11) can therefore be implemented by

$$F_s u(n) = f(0)u_{II}(n) + \sum_{r=1}^{\frac{R-1}{2}} f(r)[u_{II}(n-2^m r) + u_{II}(n+2^m r)], \qquad n \in [0, N-1],$$

where

$$u_{II}(l) = \begin{cases} u(-l-1) & \text{if } l \in [-\frac{N}{2}, -1], \\ u(l) & \text{if } l \in [0, N-1], \\ u(2N-l-1) & \text{if } l \in [N, \frac{3N}{2}], \end{cases} \tag{14}$$

$u(n)$ is an input signal to a block, $m+1$ is a level (i.e., 2^m a scale), $f(n)$ is an impulse response of some original filter, R is the length of the filter, and N is the length of the input signal $x(n)$ to the filter bank.

A filter bank with the above implementation of blocks and signal $x(n)$ at the input yields equivalent results as circular convolution for $x_{me}(n)$ as defined by Equation 12. In addition to requiring one half the amount of memory, the computational savings over a circular convolution implementation of blocks are, depending on the original filter length, three to four times fewer multiplications and one half as many additions.

A similar approach can be used for filters with $p = 1$. However, things get slightly more complicated in this case, because the filters are not of the same type and the signal components within the filter bank are of distinct type. As a consequence, an implementation of blocks that use distinct original filters will not be similar, and the implementation of blocks at level 1 differs from the implementation of blocks at other levels of analysis.

The decomposition blocks at level 1 can be implemented by the two formulas

$$G_s u(n) = g(0)[u_{II}(n-1) - u_{II}(n)], \qquad n \in [1, N-1],$$

and

$$H_s u(n) = \sum_{r=0}^{\frac{R}{2}-1} h(r)[u_{II}(n-r-1) + u_{II}(n+r)], \qquad n \in [0, N],$$

where $u_{II}(l)$ is defined by Equation 14, $g(n)$ and $h(n)$ are impulse responses of the filters computed from Equations 9 and 8, respectively, R is the length of the corresponding impulse response, and N is the length of the input signal $x(n)$ to the filter bank.

Thus decomposition blocks at subsequent levels can be implemented by

$$G_s u(n) = g(0)[u_I(n - 2^m s) - u_I(n + 2^m s)], \qquad n \in [1, N-1],$$

and

$$H_s u(n) = \sum_{r=0}^{\frac{R}{2}-1} h(r)[u_I(n - 2^m(r+s)) + u_I(n + 2^m(r+s))], \qquad n \in [0, N], \tag{15}$$

where

$$u_I(l) = \begin{cases} u(-l) & \text{if } l \in [-\frac{N}{2}, -1], \\ u(l) & \text{if } l \in [0, N], \\ u(2N-l) & \text{if } l \in [N+1, \frac{3N}{2}], \end{cases} \tag{16}$$

$u(n)$ is an input signal to a block, $m+1$ identifies a level of analysis, $g(n)$ and $h(n)$ are impulse responses of the filters from Equations 9 and 8, respectively, R is the length of the corresponding impulse response, $s = \frac{1}{2}$ is the sampling shift, and N is the length of the input signal $x(n)$ to the filter bank.

The outputs from blocks $G_s(2^m\omega)$ and $H_s(2^m\omega)$, $m \in [0, M-1]$, for $p = 1$ are of Types III and I, respectively. Next, the reconstruction blocks at level 1 can be implemented by the two formulas

$$K_{-s}u(n) = \sum_{r=1}^{\frac{R}{2}} k(r)[u_{III}(n-r+1) - u_{III}(n+r)], \qquad n \in [0, N-1],$$

and

$$H_s^*u(n) = \sum_{r=1}^{\frac{R}{2}} h(-r)[u_I(n-r+1) + u_I(n+r)], \qquad n \in [0, N-1],$$

where

$$u_{III}(l) = \begin{cases} -u(-l) & \text{if } l \in [-\frac{N}{2}, -1], \\ 0 & \text{if } l = 0, \\ u(l) & \text{if } l \in [1, N-1], \\ 0 & \text{if } l = N, \\ -u(2N-l) & \text{if } l \in [N+1, \frac{3N}{2}], \end{cases} \tag{17}$$

$u_I(l)$ is as defined by Equation 16, $u(n)$ is the input signal to each block, $k(n)$ and $h(n)$ are impulse responses of the filters from Equations 10 and 8, respectively, R is the length of the corresponding impulse response, and N is the length of the input signal to the filter bank, $x(n)$.

Note that both outputs from blocks $K_{-s}(\omega)$ and $H_s^*(\omega)$ for $p = 1$ are of Type II.

The reconstruction blocks at subsequent levels can be implemented by

$$K_{-s}u(n) = \sum_{r=0}^{\frac{R}{2}-1} k(r+1)[u_{III}(n-2^m(r+s)) - u_{III}(n+2^m(r+s))], \qquad n \in [0, N],$$

and

$$H_s^*u(n) = H_su(n),$$

where $u_{III}(l)$ is given by Equation 17, $m+1$ identifies each level, $k(n)$ is an impulse response of the filter from Equation 10 and R is its length, $s = \frac{1}{2}$ is the sampling shift, N is the length of the input signal to the filter bank, $x(n)$, and $H_su(n)$ is given by Equation 15. For completeness, we mention that the outputs from blocks $K_{-s}(2^m\omega)$ and $H_s^*(2^m\omega)$, $m \in [1, M-1]$, for $p = 1$ are of Type I.

When we compare the above implementation of blocks for $p = 1$ to circular convolution driven by a mirrored signal $x_{me}(n)$ at the input, we observe that approximately twofold less

memory, four times fewer multiplications and one half as many additions are required. (For Type I signals an additional sample has to be saved because two values are without a pair).

The implementation presented in this section performs all operations in the spatial domain. However, one could also implement the structure shown in Figure 4 with the input signal $x_{me}(n)$ (Equation 12) in the frequency domain. For short filter impulse responses, such as those given in Tables 1 and 2, the spatial implementation described in this section is certainly more efficient. For long filter impulse responses, however, filtering is faster if implemented in the frequency domain. Indeed, it makes sense to keep filtering with $G(\omega)$, which has never more than three nonzero coefficients, in the spatial domain. Additional details on alternative implementation strategies can be found in [29].

2.2.3 Two-Dimensional Discrete Dyadic Wavelet Transform

The dyadic wavelet transform of a two-dimensional function $f_2(x_1, x_2) \in L^2(\boldsymbol{R}^2)$ is defined as a set of functions [13]

$$\{W_m^1 f_2(x_1, x_2), W_m^2 f_2(x_1, x_2)\}_{m \in \boldsymbol{Z}},$$

where
$W_m^l f_2(x_1, x_2) = f_2 * \psi_m^l(x_1, x_2) = \int\int_{-\infty}^{\infty} f_2(t_1, t_2)\, \psi_m^l(x_1 - t_1, x_2 - t_2)\, dt_1\, dt_2$ for $l = 1, 2$ and $\psi_m^l(x_1, x_2) = 2^{-2m}\psi^l(2^{-m}x_1, 2^{-m}x_2)$ are wavelets $\psi^l(x_1, x_2)$ expanded by a dilation parameter 2^m.

To ensure coverage of the frequency space there must exist an $A_2 > 0$ and $B_2 < \infty$ such that

$$A_2 \leq \sum_{m=-\infty}^{\infty} \sum_{l=1}^{2} |\hat{\psi}^l(2^m\omega_1, 2^m\omega_2)|^2 \leq B_2$$

is satisfied almost everywhere. If (nonunique) functions $\chi^1(x_1, x_2), \chi^2(x_1, x_2)$ are chosen such that their Fourier transforms satisfy

$$\sum_{m=-\infty}^{\infty} \sum_{l=1}^{2} \hat{\psi}^l(2^m\omega_1, 2^m\omega_2)\, \hat{\chi}^l(2^m\omega_1, 2^m\omega_2) = 1,$$

the function $f_2(x_1, x_2)$ may be reconstructed from its dyadic wavelet transform by

$$f_2(x_1, x_2) = \sum_{m=-\infty}^{\infty} \sum_{l=1}^{2} W_m^l f_2 * \chi_m^l(x_1, x_2),$$

where $\chi_m^l(x_1, x_2) = 2^{-2m}\chi^l(2^{-m}x_1, 2^{-m}x_2)$.

However, when processing discrete functions the scale 2^m may no longer vary over all $m \in \boldsymbol{Z}$. Let the finest scale be normalized to 1 and the coarsest scale set to be 2^M. Let us

introduce a real smoothing function $\phi_2(x_1, x_2)$ such that its Fourier transform satisfies

$$|\hat{\phi}_2(\omega_1, \omega_2)|^2 = \sum_{m=1}^{\infty} \sum_{l=1}^{2} \hat{\psi}^l(2^m\omega_1, 2^m\omega_2)\, \hat{\chi}^l(2^m\omega_1, 2^m\omega_2). \tag{18}$$

Here, as in one dimension, a finite energy discrete function ($g_2(n_1, n_2) \in l^2(\boldsymbol{Z}^2)$) can be written as the uniform sampling of some function smoothed at scale 1: $g_2(n_1, n_2)$ $= S_1 f_2(n_1, n_2)$, where $f_2(x_1, x_2) \in L^2(\boldsymbol{R}^2)$ is not unique, and $S_m f_2(x_1, x_2) = f_2 * \phi_m(x_1, x_2)$. Thus, the discrete dyadic wavelet transform of $S_1 f_2(n_1, n_2)$ for any coarse scale 2^M is defined as

$$\{S_M f_2(n_1 + s, n_2 + s), W_m^1 f_2(n_1 + s, n_2 + s), W_m^2 f_2(n_1 + s, n_2 + s)\}_{m\in[1,M]}\}_{(n_1,n_2)\in\boldsymbol{Z}^2}$$

where s is a wavelet dependent sampling shift.

To implement a two-dimensional discrete dyadic wavelet transform within a fast hierarchical digital filtering scheme the wavelets were chosen to be separable products of one-dimensional functions:

$$\begin{aligned} \psi^1(x_1, x_2) &= \psi(x_1)\, 2\phi(2x_2), \\ \psi^2(x_1, x_2) &= \psi(x_2)\, 2\phi(2x_1). \end{aligned} \tag{19}$$

where $\phi(x)$ and $\psi(x)$ were chosen as described in Section 2.2.2 (recall that the Fourier transforms $\hat{\phi}(\omega)$ and $\hat{\psi}(2\omega)$ were defined by Equations 2 and 5, respectively).

From Equations 19, 5, and 2 we may write

$$\hat{\psi}^l(2\omega_1, 2\omega_2) = e^{-j\omega_l s} G(\omega_l)\, \hat{\phi}(\omega_1)\hat{\phi}(\omega_2), \tag{20}$$

where $G(\omega)$ is the frequency response of a digital filter. Choosing

$$\begin{aligned} \hat{\chi}^1(2\omega_1, 2\omega_2) &= e^{j\omega_l s} K(\omega_1) L_2(\omega_2) \hat{\phi}^*(\omega_1)\hat{\phi}^*(\omega_2), \\ \hat{\chi}^2(2\omega_1, 2\omega_2) &= e^{j\omega_l s} K(\omega_2) L_2(\omega_1) \hat{\phi}^*(\omega_1)\hat{\phi}^*(\omega_2), \end{aligned} \tag{21}$$

where $K(\omega)$ and $L_2(\omega)$ are digital filter frequency responses, we may compute Equation 18 for the finest two scales by

$$\sum_{l=1}^{2} \hat{\psi}^l(2\omega_1, 2\omega_2)\, \hat{\chi}^l(2\omega_1, 2\omega_2) = |\hat{\phi}_2(\omega_1, \omega_2)|^2 - |\hat{\phi}_2(2\omega_1, 2\omega_2)|^2. \tag{22}$$

Inserting the terms defined by Equations 21, 20, and 4 with $\hat{\phi}_2(\omega_1, \omega_2) = \hat{\phi}(\omega_1)\hat{\phi}(\omega_2)$ into Equation 22 results in

$$K(\omega_1)G(\omega_1)L_2(\omega_2) \;+\; K(\omega_2)G(\omega_2)L_2(\omega_1) \;+\; |H(\omega_1)|^2|H(\omega_2)|^2 \;=\; 1. \tag{23}$$

Equation 23 represents a relation between the frequency responses of the digital filters used to implement a two-dimensional discrete dyadic wavelet transform and is a two-dimensional analog to Equation 7.

Solving Equation 23 for $L_2(\omega)$ by substituting $K(\omega)G(\omega)$ from Equation 7 yields the closed formula

$$L_2(\omega) = \frac{1}{2}\left(1 + |H(\omega)|^2\right) \tag{24}$$

In Table 3 we provide the filter coefficients for $L_2(\omega)$ from Equation 24 for $2n+p \in \{1,2,3,4\}$.

	l_2			
m	$n=0$, $p=1$	$n=1$, $p=0$	$n=1$, $p=1$	$n=2$, $p=0$
-4				0.001953125
-3			0.0078125	0.015625
-2		0.03125	0.046875	0.0546875
-1	0.125	0.125	0.1171875	0.109375
0	0.75	0.6875	0.65625	0.63671875
1	0.125	0.125	0.1171875	0.109375
2		0.03125	0.046875	0.0546875
3			0.0078125	0.015625
4				0.001953125

Table 3: Impulse responses of filters $L_2(\omega)$ for $2n+p \in \{1,2,3,4\}$.

As in the one-dimensional case, a two-dimensional discrete dyadic wavelet transform can be implemented within a fast hierarchical filtering scheme. The filter bank implementation follows from Equations 20, 4, and 23, and is shown in Figure 5.

The implementation of filtering with $L_2(\omega)$ in two dimensions (Table 3) is simple.

Suppose our two-dimensional structure is of size $N_1 \times N_2$ and its mirror extension handles boundary effects. The number of levels remains restricted by Equation 13, where $N = \min\{N_l;\ l \in [1,2]\}$ and R_{max} is the length of the impulse response of $|H(\omega)|^2$.

Since only separable filters are used in the filter bank implementation, we can simply apply the one-dimensional implementation as presented in Section 2.2.2. Equations for implementing blocks $G_s(\omega)$, $H_s(\omega)$, $K_{-s}(\omega)$, and $H_s^*(\omega)$ at distinct levels and values of p are then straightforward.

As previously mentioned in Section 2.2.2, the computational savings when $p = 0$ for this implementation over circular convolution and a mirror extended signal are (depending on the original filter length) three to four times fewer multiplications and one half as many

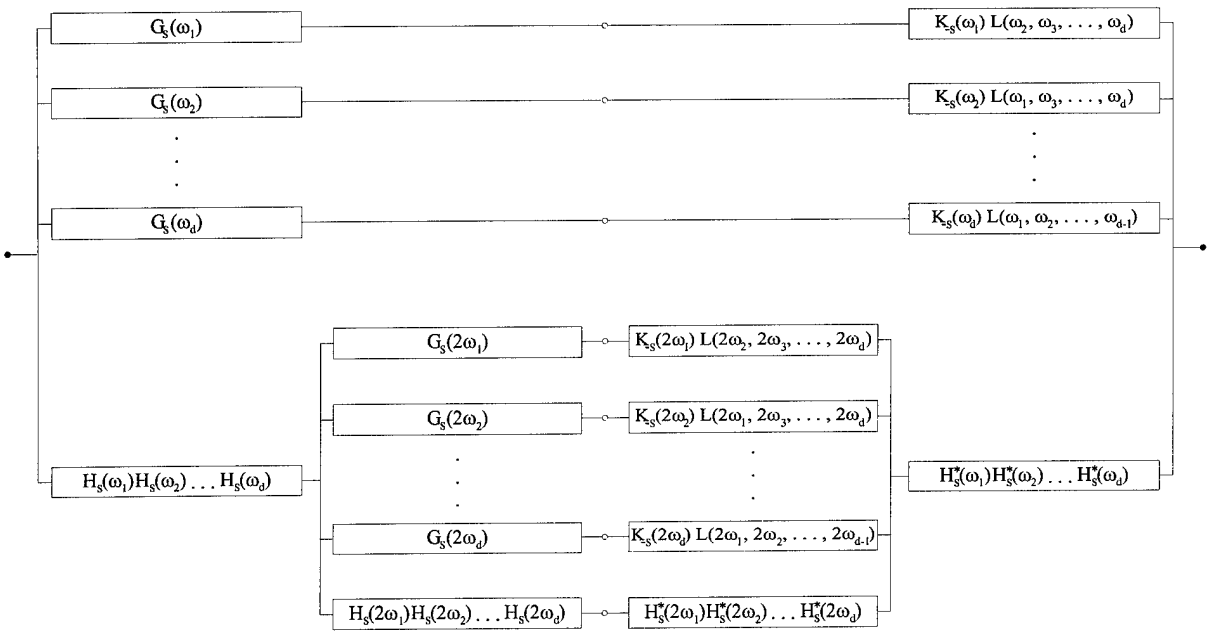

Figure 5: Filter bank implementation of a two-dimensional discrete dyadic wavelet transform decomposition (left) and reconstruction (right) for two levels of analysis. $H_s^*(\omega)$ denotes the complex conjugate of $H_s(\omega)$.

additions. Of course, for longer filters a frequency domain implementation may be more efficient.

2.2.4 Contrast Enhancement in Digital Mammography

In mammography, early detection of breast cancer relies upon the ability to distinguish between malignant and benign mammographic features. The detection of small malignancies and subtle lesions is often difficult. Contrast enhancement can make more obvious unseen or barely seen features of a mammogram without requiring additional radiation.

Within a discrete dyadic wavelet transform, a framework for contrast enhancement was achieved by applying a (possibly nonlinear) function (referred to as "enhancement function") to wavelet coefficients $\{\{W_m^1 f_2(n_1+s, n_2+s), W_m^2 f_2(n_1+s, n_2+s)\}_{m\in[1,M]}\}_{(n_1,n_2)\in \boldsymbol{Z}^2}$ and then reconstructing an enhanced image with modified coefficients [10].

In [9] it was shown that multiscale contrast enhancement techniques based on three multiscale representations: 1) discrete dyadic wavelet transform, 2) φ-transform, and 3) hexagonal wavelet transform, can outperform traditional contrast enhancement techniques such as histogram equalization and unsharp masking [30] when applied to subtle features in digital mammography. Furthermore, in [12, 11, 10], it was shown that unsharp masking

with a Gaussian lowpass filter can be formulated as a special case of contrast enhancement via a discrete dyadic wavelet transform.

The enhancement function was chosen such that: 1) low-contrast areas were treated more aggressively than existing areas of high-contrast, 2) edges were not blurred, 3) monotonically increasing, and 4) antisymmetric (i.e., odd). A simple function that satisfies the above conditions is [11]

$$E(x) = \begin{cases} x - (K-1)T & \text{if } x < -T \\ Kx & \text{if } |x| \leq T \\ x + (K-1)T & \text{if } x > T. \end{cases} \tag{25}$$

Figure 6 shows the enhancement function from Equation 25 for parameter values $K = 20$ and $T = 1$.

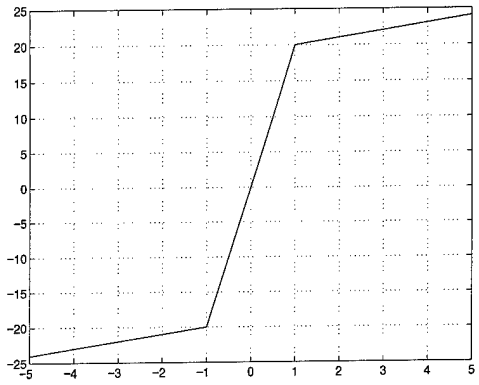

Figure 6: The enhancement function (Equation 25 with $K = 20$ and $T = 1$).

Filters with $p = 0$ (Equations 8 through 10) were found to be more suitable for contrast enhancement than wavelet filters designed with $p = 1$. It has been shown that edges change their position (introduce artifacts) when the wavelet coefficients computed for $p = 1$ are modified by a nonlinear enhancement function [12].

Figure 7 shows an original mammographic image and an enhanced image obtained by using filters and wavelets with $2n+p = 4$ and an enhancement function defined by Equation 25 with $K = 30$ and $T_m = 0.12 \max\{|W_m^l f_2(n_1 + s, n_2 + s)|\,;\ l \in \{1,2\},\ (n_1, n_2) \in \boldsymbol{Z}^2\}$, $m \in \{1, M\}$. The image matrix size was 775 $\times$ 436 pixels, 210 micron spot size, and the analysis was performed up to the fifth level (i.e., $M = 5$).

Enhancement of a suspicious area of a mammogram using wavelets with $2n+p = 2$ and an enhancement function given by Equation 25 is demonstrated in Figure 8. The parameters were: $K = 20$, $T_m = 0.6 \max\{|W_m^l f_2(n_1 + s, n_2 + s)|\,;\ l \in \{1,2\},\ (n_1, n_2) \in \boldsymbol{Z}^2\}$, $m \in \{1, M\}$, and $M = 7$. The image and enhanced area matrix sizes were 655 $\times$ 615 pixels and 175 $\times$ 165 pixels, respectively.

Additional details on contrast enhancement by a discrete dyadic wavelet transform, including incorporation of denoising into the enhancement scheme, can be found in [10, 11, 12].

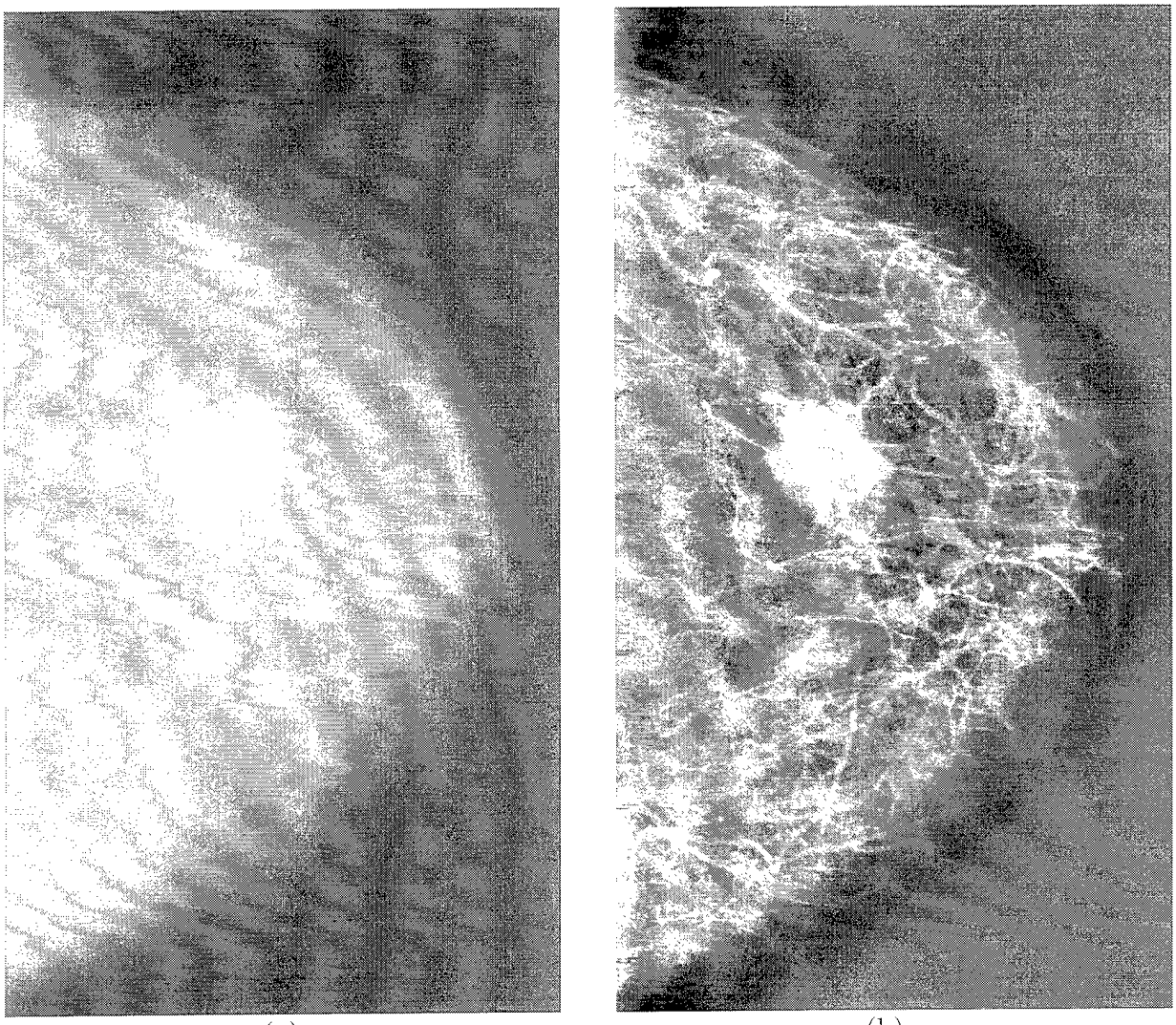

(a) (b)

Figure 7: (a) An original mammographic image containing a spicular mass. (b) An enhanced image with spicular borders well delineated.

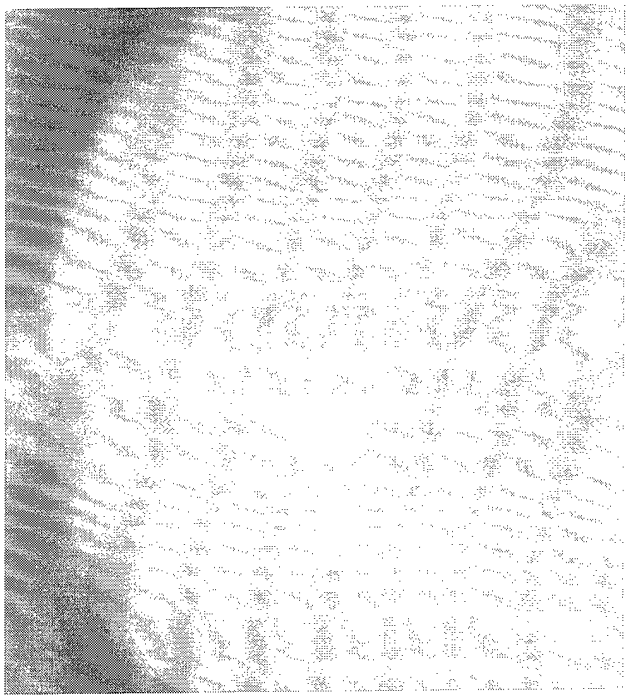

(a)

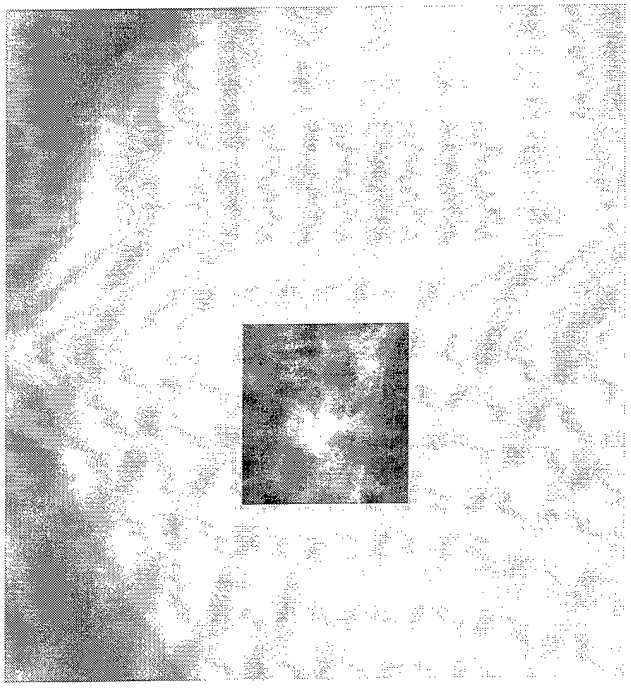

(b)

Figure 8: (a) An original mammographic image containing an ill-defined mass. (b) An image with a suspicious area enhanced.

2.2.5 Summary

We computed the coefficients for filters of low order splines used as smoothing functions in a fast hierarchical digital filtering implementation of a discrete dyadic wavelet transform for both one and two-dimensional processing. A mirror extended input signal to a filter bank implementation of the discrete dyadic wavelet transform enabled us to take advantage of the symmetry/antisymmetry of both signals and filters for an efficient implementation of a dyadic transform. There are no restrictions on the size of the input signal which makes this scheme attractive for extracting arbitrary rectangular regions from digital mammograms. The presented algorithm is iterative across scales: a noniterative scheme suitable for high speed (interactive) parallel processing can be derived easily by using the described approach on each dyadic scale independently.

2.3 Denoising and Enhancement via Multiscale Sub-Octave Analysis

2.3.1 Introduction

Orthonormal wavelet transforms (OWT) and discrete dyadic wavelet transforms (DWT) have been successfully used in various application areas, such as data compression, edge detection, texture analysis, noise reduction, and image enhancement [31, 26, 32, 33, 13, 24]. In this part of our research, both OWT and DWT were studied for denoising and contrast enhancement. Analysis and experiments show that a DWT has several advantages over an OWT for denoising and feature enhancement purposes [34, 35]. A DWT with a wavelet equal to a first order derivative of a smoothing function as its basis can separate feature variational energy (VE) from noise VE [34, 35]. This helps identify which wavelet coefficients to modify to enhance specific features of interest (FOI) without amplifying noise. The mother wavelet was a smooth and antisymmetric function with few oscillations, which kept denoising under a DWT less affected from pseudo-Gibbs phenomenon. This can be clearly seen from the results under an OWT [36, 37] compared with the results obtained from our denoising algorithm under a DWT [35]. The discrete filters used to compute a DWT have compact support requiring few taps. In addition, DWT wavelet coefficients have a clear meaning in that they are proportional to the image intensity changes (gradients). A DWT is a stable and complete representation, which guarantees that a DWT will not cause a loss or gain of energy. By properly modifying signal and noise VE, we can achieve distinct noise reduction and feature enhancement within a digital mammogram.

A framework for multiscale wavelet analysis was implemented as a research tool for denoising and feature enhancement [11, 12]. Here, we address both signal or image restoration and enhancement problems via wavelet shrinkage and feature emphasis. This approach takes advantage of both soft-thresholding and hard-thresholding wavelet shrinkage techniques to eliminate noise while preserving the sharpness of prominent features. It also incorporates local energy gain for nonlinear processing to enhance contrast within structures and along object boundaries. Thus, feature restoration and enhancement were accomplished by modifying the gain of a signal's VE. Methods have been developed for achieving denoising and feature enhancement, such as regulated soft-thresholding and adaptive VE gain processing combined with hard-thresholding to remove small noise perturbations [34, 35].

Even though DWT-based denoising algorithms have produced superior results compared to other methods, we point out that the DWT has limited ability to characterize band-limited features, such as texture, and subtle features of mammographic images. A DWT is an octave-based transform with its scales increasing as powers of 2. We cannot visualize or detect the signal details for scales between two consecutive levels of a DWT. To alleviate this problem, and to more reliably isolate noise and identify features through scale space, we have developed a sub-octave wavelet transform [38], which is the generalization of the DWT. A sub-octave wavelet transform provides a means to visualize signal details within sub-octave frequency bands with equally-spaced division within each octave band and is able to characterize the signal details more precisely. The theoretical development of a sub-octave wavelet transform and efficient implementation were undertaken in this study.

2.3.2 Sub-Octave Wavelet Transform

A wavelet transform can be completely characterized by a family of wavelet bases used for decomposition and reconstruction. If a family of wavelets bases $\{\psi_n(x)\}$ is complete and orthonormal, the wavelet transform is usually called *an orthonormal wavelet transform.* A Haar wavelet is a simple example of orthonormal wavelets. The problems with a Haar wavelet is that it is a discontinuous function and not localized in the frequency domain. The filters $\{H, G\}$ for performing an orthonormal wavelet transform satisfy the following equation

$$|H(\omega)|^2 + |G(\omega)|^2 = 1. \tag{26}$$

If the family of bases $\{\psi_n(x)\}$ is complete and linearly independent, but not orthonormal, the wavelet transform is called *a biorthogonal wavelet transform.* More generally, if the family of wavelets $\{\psi_n(x)\}$ is not linearly independent and redundant, they form *a wavelet frame* [39].

For a discrete dyadic wavelet transform, we relax the orthonormal constraint and can have different decomposition and reconstruction wavelets as long as the corresponding high-pass filters $G(\omega), K(\omega)$ satisfy the following equation

$$|H(\omega)|^2 + G(\omega)K(\omega) = 1. \tag{27}$$

In the section below, we develop a sub-octave wavelet transform (SWT) for denoising and enhancement.

1-D Sub-Octave Wavelet Transform

In this section, we show that if we further divide each octave band into M equally-spaced sub-octave bands, M basis wavelets can be used to capture the detail information of a signal in each sub-octave frequency band. The M wavelet functions are represented as $\psi^m(x) \in L^2(\boldsymbol{R})$, where $m = 1, 2, .., M$. The M-sub-octave wavelet transform of a 1-D function $f(x) \in L^2(\boldsymbol{R})$ at the scale 2^j and location x, and for the m-th sub-octave frequency band is defined as

$$W_{2^j}^m f(x) = f * \psi_{2^j}^m(x), \tag{28}$$

where $\psi_{2^j}^m(x) = \frac{1}{2^j}\psi^m(\frac{x}{2^j})$ is the dilation of the m-th basis wavelet $\psi^m(x)$, sometimes called the m-th analysis wavelet, at scale 2^j, $m = 1, 2, ..., M$, and $j \in Z$. In the frequency domain, we have

$$\hat{W}_{2^j}^m f(\omega) = \hat{f}(\omega)\,\hat{\psi}^m(2^j\omega), \tag{29}$$

by taking the Fourier transform of Equation 28. To have a more flexible choice for the M basis wavelets, we impose that the wavelet functions satisfy a wavelet frame condition (similar to [13])

$$A \leq \sum_{j=-\infty}^{+\infty} \sum_{m=1}^{M} |\hat{\psi}^m(2^j\omega)|^2 \leq B,$$

where A and B are positive constants and $\omega \in R$. In the spatial domain, we have

$$A||f(x)||^2 \leq \sum_{j=-\infty}^{+\infty} \sum_{m=1}^{M} ||W_{2^j}^m f(x)||^2 \leq B||f(x)||^2.$$

The function $f(x)$ can be recovered from its sub-octave wavelet transform by the following formula

$$f(x) = \sum_{j=-\infty}^{+\infty} \sum_{m=1}^{M} W_{2^j}^m f * \gamma_{2^j}^m(x) = \sum_{j=-\infty}^{+\infty} \sum_{m=1}^{M} f * \psi_{2^j}^m * \gamma_{2^j}^m(x), \tag{30}$$

where $\gamma^m(x)$ is the m-th synthesis wavelet for the inverse sub-octave wavelet transform. The frequency response of $\{\psi_{2^j}^m(x) \,|\, m = 1, 2, ..., M\}$ together at any scale 2^j are required to

capture the details within an octave frequency band. For perfect reconstruction of $f(x)$, $\psi_{2^j}^m(x)$ and $\gamma_{2^j}^m(x)$ should satisfy

$$\sum_{j=-\infty}^{+\infty} \sum_{m=1}^{M} \hat{\psi}^m(2^j\omega)\,\hat{\gamma}^m(2^j\omega) \;=\; 1. \tag{31}$$

Equation 31 can be obtained by taking the Fourier transform on both sides of Equation 30. To ensure perfect reconstruction, the whole frequency axis should be covered by the analysis and synthesis wavelets, thus the reconstruction wavelets $\gamma^m(x)$ can be any functions whose Fourier transforms satisfy the above equation. There are, in fact, many choices for the decomposition and reconstruction wavelets to satisfy the above equation. Here we only discuss the class of wavelets which are the first order derivatives of a smoothing function, such as spline functions of any order. A 1-D sub-octave wavelet transform can be easily extended to a 2-D sub-octave transform by computing sub-octave wavelet coefficients along horizontal and vertical directions, as explained in the following section.

2-D Sub-Octave Wavelet Transform

The M-sub-octave wavelet transform of a 2-D function $f(x,y) \in L^2(\boldsymbol{R}^2)$ at the scale 2^j and location (x,y), and for the m-th sub-octave frequency band is defined as

$$W_{2^j}^{i,m} f(x,y) \;=\; f * \psi_{2^j}^{i,m}(x,y), \tag{32}$$

where $\psi_{2^j}^{i,m}(x,y) = \frac{1}{2^{2j}}\psi^{i,m}(\frac{x}{2^j}, \frac{y}{2^j})$, $i = 1,2$ (for horizontal or vertical direction), $m = 1,2,...,M$, and $j \in Z$. In the Fourier domain, Equation 32 becomes

$$\hat{W}_{2^j}^{i,m} f(\omega_x,\omega_y) \;=\; \hat{f}(\omega_x,\omega_y)\,\hat{\psi}^{i,m}(2^j\omega_x, 2^j\omega_y). \tag{33}$$

The function $f(x,y)$ can be recovered from its 2-D sub-octave wavelet transform by the following formula

$$\begin{aligned} f(x,y) &= \sum_{j=-\infty}^{+\infty} \sum_{i=1}^{2} \sum_{m=1}^{M} W_{2^j}^{i,m} f * \gamma_{2^j}^{i,m}(x,y) \\ &= \sum_{j=-\infty}^{+\infty} \sum_{i=1}^{2} \sum_{m=1}^{M} f * \psi_{2^j}^{i,m} * \gamma_{2^j}^{i,m}(x,y). \end{aligned} \tag{34}$$

For perfect reconstruction of $f(x,y)$, $\psi_{2^j}^m(x,y)$ and $\gamma_{2^j}^m(x,y)$ should satisfy

$$\sum_{j=-\infty}^{+\infty} \sum_{i=1}^{2} \sum_{m=1}^{M} \hat{\psi}^{i,m}(2^j\omega_x, 2^j\omega_y)\,\hat{\gamma}^{i,m}(2^j\omega_x, 2^j\omega_y) \;=\; 1. \tag{35}$$

This perfect reconstruction condition can be obtained by taking the Fourier transform of Equation 34.

2.3.3 Discrete Sub-Octave Wavelet Transform

The transform parameters in a sub-octave wavelet transform are continuous variables. This results in a highly redundant representation. It is possible to discretize these parameters and still be able to achieve perfect reconstruction [39]. For digital image processing, the sub-octave wavelet transform of a discrete function can be carried out through a uniform sampling of a continuous sub-octave wavelet transform. Below, we describe the discrete sub-octave wavelet transform.

1-D Discrete Sub-Octave Wavelet Transform

In the discrete domain, we are limited by the finest scale of 1. In general, a discrete function can be decomposed into the details of fine-to-coarse scales, so we let

$$|\hat{\varphi}(\omega)|^2 = \sum_{j=1}^{+\infty} \sum_{m=1}^{M} \hat{\psi}^m(2^j\omega)\,\hat{\gamma}^m(2^j\omega). \tag{36}$$

For a J-level discrete sub-octave wavelet transform, we can write

$$|\hat{\varphi}(\omega)|^2 = \sum_{j=1}^{J} \sum_{m=1}^{M} \hat{\psi}^m(2^j\omega)\,\hat{\gamma}^m(2^j\omega) + |\hat{\varphi}(2^J\omega)|^2. \tag{37}$$

If the scaling approximation of a function $f(x)$ at scale 2^j is represented as

$$S_{2^j} f(x) = f * \varphi_{2^j}(x), \tag{38}$$

then $\{\, W^m_{2^j} f(x_n),\ S_{2^J} f(x_n) \mid n \in Z,\ j = 1, 2, ..., J,$ and $m = 1, 2, ..., M \,\}$ is the wavelet representation of a discrete function $f(x_n)$ under a J-level discrete M-sub-octave wavelet transform. $W^m_{2^j} f(x_n)$ and $S_{2^J} f(x_n)$ are uniform samplings of their continuous counterparts respectively.

If we let $J = 1$, then we have

$$|\hat{\varphi}(\omega)|^2 = \sum_{m=1}^{M} \hat{\psi}^m(2\omega)\,\hat{\gamma}^m(2\omega) + |\hat{\varphi}(2\omega)|^2. \tag{39}$$

Let us assume that for each basis wavelet pair $\hat{\psi}^m(\omega)$ and $\hat{\gamma}^m(\omega)$, there exists a pair of corresponding functions $G^m(\omega)$ and $K^m(\omega)$ which need to be determined and (with certain temporal shift t) satisfy

$$\hat{\psi}^m(2\omega) = \hat{\varphi}(\omega)\, G^m(\omega)\, e^{-it\omega},$$
$$\hat{\gamma}^m(2\omega) = \hat{\varphi}(\omega)\, K^m(\omega)\, e^{it\omega}.$$

For scaling function $\hat{\varphi}(\omega)$, there exists a function $H(\omega)$ which satisfies

$$\hat{\varphi}(2\omega) = \hat{\varphi}(\omega)\, H(\omega)\, e^{-it\omega}.$$

Replacing $\hat{\psi}^m(2\omega)$, $\hat{\gamma}^m(2\omega)$, and $\hat{\varphi}(2\omega)$ in Equation 39, we have the following fundamental relation for a sub-octave wavelet transform (SWT)

$$|H(\omega)|^2 + \sum_{m=1}^{M} G^m(\omega)\, K^m(\omega) = 1. \tag{40}$$

The discrete sub-octave wavelet transform of a function $f(x_n) \in l^2(\boldsymbol{Z})$ can be implemented by using the following recursive relations between two consecutive levels j and $j+1$

$$\hat{W}^m_{2^{j+1}} f(\omega) = \hat{S}_{2^j} f(\omega) G^m(2^j\omega), \tag{41}$$

$$\hat{S}_{2^{j+1}} f(\omega) = \hat{S}_{2^j} f(\omega) H(2^j\omega), \tag{42}$$

where $j \geq 0$, $1 \leq m \leq M$, and $\hat{S}_1 f(\omega) = \hat{f}(\omega_x, \omega_y)$. The reconstruction $\hat{S}_1 f(\omega)$ from the sub-octave wavelet decomposition can be implemented through the following recursive relation

$$\hat{S}_{2^j} f(\omega) = \hat{S}_{2^{j+1}} f(\omega) H^*(2^j\omega) + \sum_{m=1}^{M} \hat{W}^m_{2^{j+1}} f(\omega) K^m(2^j\omega), \tag{43}$$

where H^* is the complex conjugate of H. A 3-level M-sub-octave wavelet decomposition and reconstruction process based on the above recursive relations is shown in Figure 9. The corresponding division of the frequency band is given in Figure 10. In general, for M-sub-octave decomposition and reconstruction of a SWT, we need to have M pairs of decomposition and reconstruction basis wavelets. When M is a power of 2, we can perform the decomposition and reconstruction using a single pair of wavelets similar to the way Daubechies showed in [26]. Figure 11 presents how to carry out a 2-level 4-sub-octave decomposition and reconstruction of a SWT using FIR filters corresponding to a single pair of basis wavelets.

2-D Discrete Sub-Octave Wavelet Transform

For the decomposition of a 2-D discrete function, we let the frequency response of a scaling function be defined in the following formula

$$|\hat{\varphi}(\omega_x, \omega_y)|^2 = \sum_{j=1}^{+\infty} \sum_{i=1}^{2} \sum_{m=1}^{M} \hat{\psi}^{i,m}(2^j\omega_x, 2^j\omega_y)\, \hat{\gamma}^{i,m}(2^j\omega_x, 2^j\omega_y). \tag{44}$$

For a 2-D J-level discrete sub-octave wavelet transform, we can formulate

$$|\hat{\varphi}(\omega_x, \omega_y)|^2 = \sum_{j=1}^{J} \sum_{i=1}^{2} \sum_{m=1}^{M} \hat{\psi}^{i,m}(2^j\omega_x, 2^j\omega_y)\, \hat{\gamma}^{i,m}(2^j\omega_x, 2^j\omega_y) + |\hat{\varphi}(2^J\omega_x, 2^J\omega_y)|^2. \tag{45}$$

If the scaling approximation of a function $f(x, y)$ at scale 2^j is represented by

$$S_{2^j} f(x, y) = f * \varphi_{2^j}(x, y), \tag{46}$$

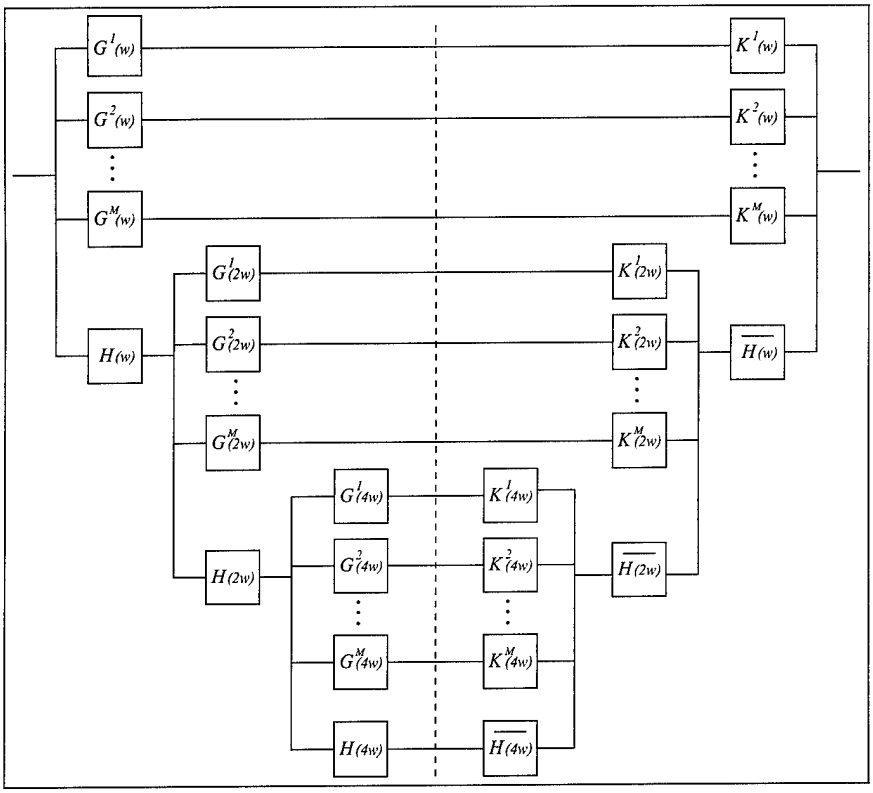

Figure 9: A 3-level SWT decomposition and reconstruction diagram of a 1-D function.

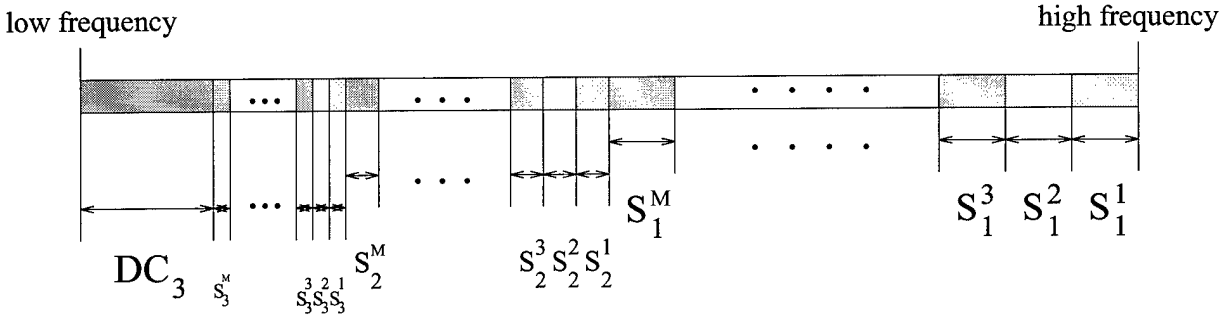

Figure 10: Division of the frequency band under the SWT shown in Figure 9.

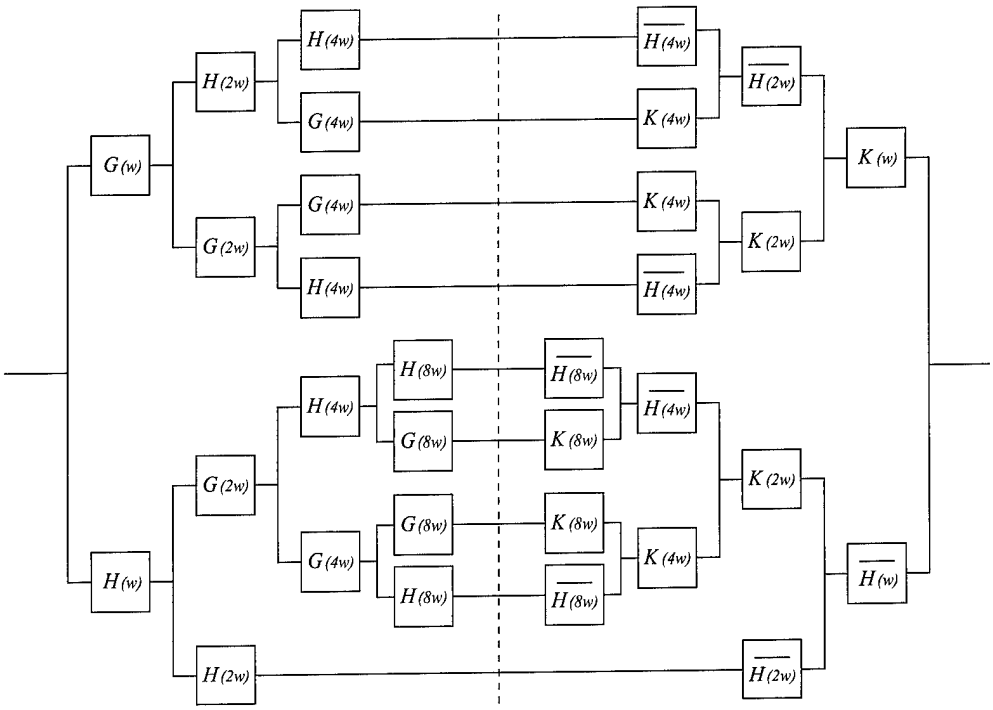

Figure 11: A 2-level 4-sub-octave decomposition and reconstruction of a SWT.

then $\{ W_{2^j}^{i,m} f(x_u, y_v), S_{2^J} f(x_u, y_v) \,|\, u, v \in Z, i = 1, 2,\ j = 1, .., J,$ and $m = 1, .., M \}$ is called the wavelet representation of a discrete function $f(x_u, y_v)$ under a 2-D J-level discrete M-sub-octave wavelet transform. In general, $\varphi(x, y)$ is a 2-D scaling function and $\psi^{i,m}(x, y)$ and $\gamma^{i,m}(x, y)$ are the m-th directional analysis and synthesis wavelets. There are many choices of these functions that satisfy Equation 45. Similar to the way 2-D wavelets are constructed using 1-D wavelets in [13], we use tensor products to construct 2-D sub-octave wavelets using 1-D sub-octave wavelets. Thus we can write

$$\hat{\psi}^{1,m}(2^j\omega_x, 2^j\omega_y) = \hat{\psi}^m(2^j\omega_x)\hat{\varphi}(2^{j-1}\omega_y), \tag{47}$$

$$\hat{\psi}^{2,m}(2^j\omega_x, 2^j\omega_y) = \hat{\varphi}(2^{j-1}\omega_x)\hat{\psi}^m(2^j\omega_y), \tag{48}$$

$$\hat{\varphi}(2^j\omega_x, 2^j\omega_y) = \hat{\varphi}(2^j\omega_x)\hat{\varphi}(2^j\omega_y). \tag{49}$$

Through this construction of 2-D wavelets, we implemented a 2-D sub-octave wavelet transform using 1-D convolution with FIR filters of a 1-D sub-octave wavelet transform. Figure 12 shows the division of the frequency plane under a 2-level SWT. A 2-D sub-octave wavelet transform can be implemented by 1-D FIR filters along horizontal and vertical directions. In the left diagram of Figure 13, a fourth-order spline smoothing function, its first and second derivative sub-octave wavelets, and the corresponding scaling function are shown. The right diagram of Figure 13 presents four sub-octave wavelets corresponding to the first, second, and third derivatives of the smoothing spline in the left diagram.

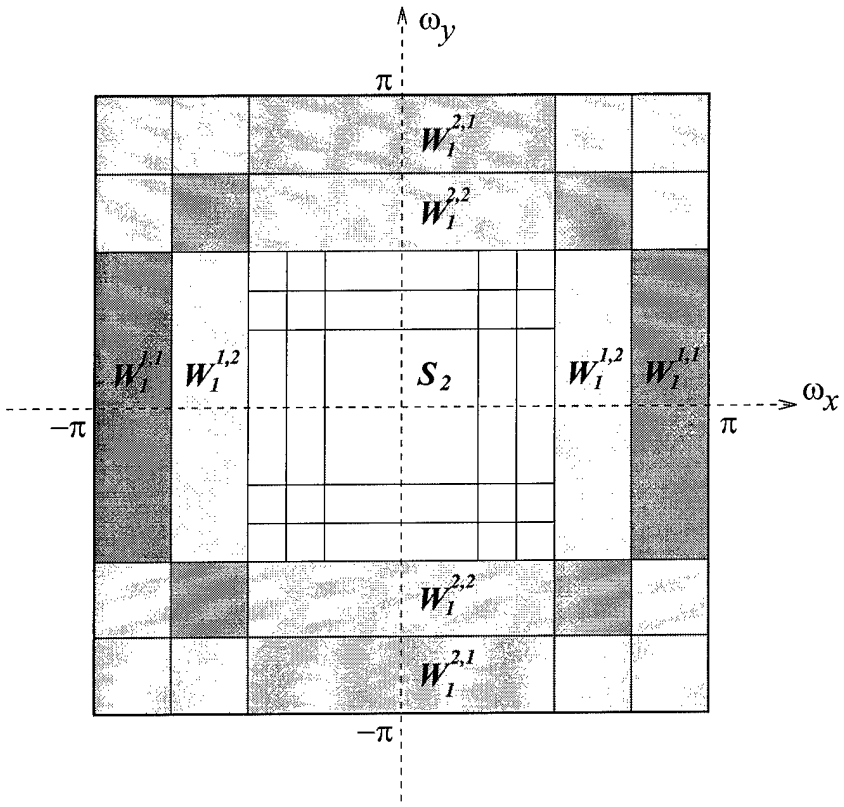

Figure 12: Division of the frequency plane under a 2-D SWT.

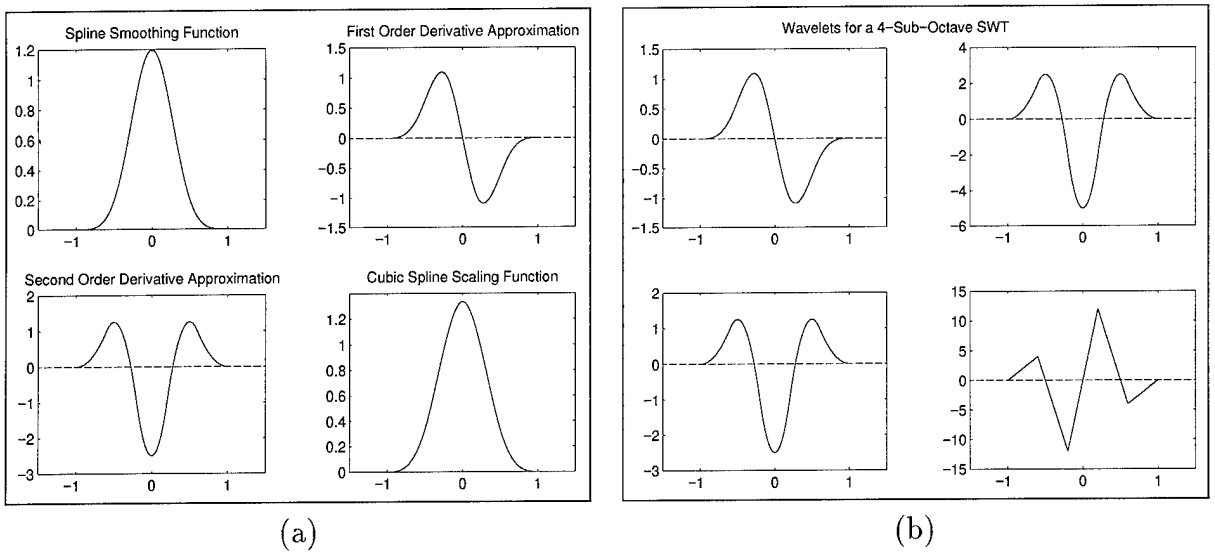

Figure 13: Smoothing, scaling, and wavelet functions for a SWT. (a) Functions for a 2-sub-octave SWT. (b) Wavelet functions for a 4-sub-octave SWT.

A dyadic wavelet transform is a special case of a sub-octave wavelet transform with $M = 1$. As an example, a discrete 2-sub-octave wavelet transform is shown to divide the details of an octave band into the details of 2 sub-octave bands, and one sub-octave can be used for detecting local maxima while the other sub-octave for identifying zero-crossings. Thus, in this sub-octave wavelet representation, we take advantage of local maxima and zero-crossing representations to more accurately characterize local features.

2.3.4 Noise Modeling

Signal and image degradations by noise and artifacts are frequent phenomena of the real world image acquisition. Image degradations have a significant impact on radiologist performance and computer-assisted methods. In addition, noise and artifacts often make feature extraction, analysis, and recognition algorithms unreliable. The denoising and feature enhancement techniques described next improve the reliability of our image processing techniques.

Additive Noise Model

Additive noise can be (in general) represented by the following formula:

$$f(\mathbf{x}) = g(\mathbf{x}) + \eta_a(\mathbf{x}), \tag{50}$$

where $g(\mathbf{x})$ is an unknown function. The function $f(\mathbf{x})$ is a noisy observation of $g(\mathbf{x})$, $\eta_a(\mathbf{x})$ is additive noise, and $\mathbf{x}$ is a vector of spatial locations or temporal samples.

For additive noise, there are existing techniques based on mean squared error or l^1 norm optimization to remove noise, such as Donoho's wavelet shrinkage techniques [36, 40, 41], Chen and Donoho's basis pursuit denoising [42], Mallat's local-maxima-based method for removing white noise [24], and wavelet packet-based denoising [43].

By incorporating a denoising mechanism into our feature enhancement process, we may enhance contrast without amplifying noise. Subtle features barely seen or invisible in a mammogram, such as microcalcification clusters, spicular lesions, and circular (arterial) calcifications, may be enhanced via our sub-octave wavelet transform. Since we treat noise and features independently, we were able to obtain superior results compared to existing algorithms designed for enhancement alone.

2.3.5 Wavelet Shrinkage and Feature Emphasis

In this section, a denoising and contrast enhancement scheme based on wavelet shrinkage and feature emphasis is presented. In this investigation, we studied hard thresholding and Donoho's soft thresholding wavelet shrinkage [40] for noise reduction. The advantage of

soft thresholding is that it can achieve smoothness while hard thresholding better preserves features. In our unified approach for accomplishing denoising and feature enhancement, we took advantage of both thresholding methods. Donoho's soft thresholding method [40] was developed for an orthonormal wavelet transform [31] primarily with Daubechies's Symmlet 8 basis wavelet and his denoising results showed some undesired side-effects, from pseudo-Gibbs phenomenon [37]. By using a SWT and basis wavelets without any oscillations, our method was relatively free from side-effects after denoising. Experiments show that a SWT with a first order derivative of a smoothing function as its basis wavelet separated feature VE and noise VE coefficients. In this algorithm, we adopt regularized soft thresholding wavelet shrinkage to remove noise VE within the finer levels of scale. We then apply to wavelet coefficients a non-linear gain with hard thresholding for preserving features while removing small noise perturbations within the middle levels of space-frequency.

Wavelet Shrinkage By Soft Thresholding

Soft thresholding [40] operation can be represented as

$$u(\mathbf{x}) = \mathcal{T}_S(v(\mathbf{x}), t) = \text{sign}(v(\mathbf{x}))\,(|v(\mathbf{x})| - t)_+, \tag{51}$$

where threshold t is proportional to the noise level and $\mathbf{x} \in D$, the domain of $v(\mathbf{x})$, and $u(\mathbf{x})$ is the result of soft thresholding and has the same sign as $v(\mathbf{x})$ if non-zero. The expression $(|v(\mathbf{x})| - t)_+$ is defined as

$$(|v(\mathbf{x})| - t)_+ = \begin{cases} |v(\mathbf{x})| - t & \text{if } |v(\mathbf{x})| > t, \\ 0 & \text{otherwise.} \end{cases}$$

SWT coefficients can be processed for noise reduction by

$$W_{2^j}^{i,m,*} f(\mathbf{x}) = \mathcal{T}_S(W_{2^j}^{i,m} f(\mathbf{x}), t_{2^j}^{i,m}), \tag{52}$$

where $i = 1, 2$ (omitted for 1-D signals), $j = 1, ..., k$, $k \leq J$, $m = 1, ..., M$, and $t_{2^j}^{i,m}$ is a noise and scale-related threshold. $W_{2^j}^{i,m,*} f(\mathbf{x})$ is a modified coefficient. We recall that Donoho's soft thresholding method used a single global threshold. However, the noise coefficients under a SWT have average decay through fine-to-coarse scales, we regulated soft-thresholding wavelet shrinkage by applying coefficient-dependent thresholds decreasing across scales.

Wavelet Shrinkage By Hard-Thresholding

A hard thresholding operation can be expressed as

$$u(\mathbf{x}) = \mathcal{T}_H(v(\mathbf{x}), t) = v(\mathbf{x})(|v(\mathbf{x})| \geq t), \tag{53}$$

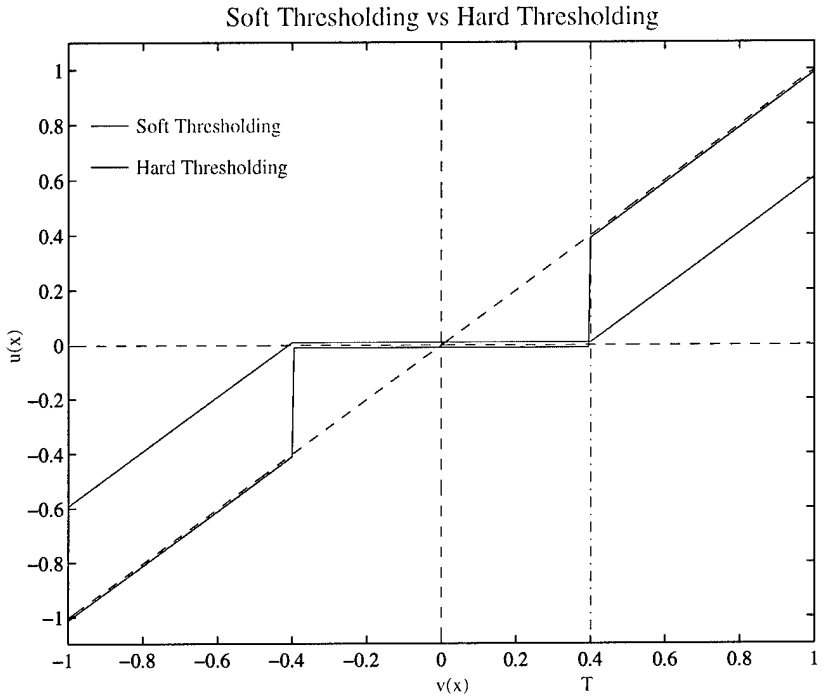

Figure 14: Various thresholding methods.

where t is a threshold value, $\mathbf{x} \in D$, the domain of $v(\mathbf{x})$, and $u(\mathbf{x})$ is the result of hard thresholding and has the same sign as $v(\mathbf{x})$ if non-zero. The meaning of $(|v(\mathbf{x})| \geq t)$ is defined by the expression

$$(|v(\mathbf{x})| \geq t) = \begin{cases} 1 & \text{if } |v(\mathbf{x})| \geq t, \\ 0 & \text{otherwise.} \end{cases}$$

Sub-octave wavelet coefficients were modified by hard-thresholding for noise reduction by

$$W_{2^j}^{i,m,*} f(\mathbf{x}) = \mathcal{T}_H(W_{2^j}^{i,m} f(\mathbf{x}), t_{2^j}^{i,m}), \tag{54}$$

where $i = 1, 2$ (omitted for 1-D signals), $j = 1, ..., k$, and $k \leq J$, $m = 1, ..., M$, and $t_{2^j}^{i,m}$ is (in general) a threshold related to noise and scale. $W_{2^j}^{i,m,*} f(\mathbf{x})$ is a processed coefficient. Figure 14 shows a functional diagram of normalized soft and hard thresholding.

Feature Emphasis By Generalized Adaptive Gain

Recently, several wavelet-based enhancement techniques have been developed [44, 45, 46, 9]. Adaptive gain non-linear processing [46, 10] has been successfully used to enhance features in digital mammograms. The adaptive gain non-linear processing is further generalized in this study to incorporate hard thresholding in order to avoid amplifying noise and actually remove small noise perturbations. The generalized adaptive

gain (GAG) non-linear operator is defined as

$$E_{GAG}(v) = \begin{cases} 0 & \text{if } |v| < T_1, \\ \text{sign}(v)\, T_2 + \bar{a}\,(\text{sigm}(c(u-b)) - \text{sigm}(-c(u+b))) & \text{if } T_2 \le |v| \le T_3, \\ v & \text{otherwise,} \end{cases} \tag{55}$$

where $v \in [-1,\ 1]$, $\bar{a} = a(T_3 - T_2)$, $u = \text{sign}(v)(|v| - T_2)/(T_3 - T_2)$, $b \in (0,\ 1)$, $0 \le T_1 \le T_2 < T_3 \le 1$, c is a gain factor, and a can be computed as

$$a = \frac{1}{\text{sigm}(c(1-b)) - \text{sigm}(-c(1+b))}, \tag{56}$$

$$\text{sigm}(v) = \frac{1}{1+e^{-v}}. \tag{57}$$

T_1, T_2, and T_3 are selected parameters. When $T_1 = T_2 = 0$ and $T_3 = 1$, The expression is equivalent to the adaptive gain non-linear function in [46, 10]. The interval $[T_2,\ T_3]$ serves as a sliding window for feature selectivity. It can be adjusted to emphasize local regions within a specific range of variation. Thus, by selecting gain values and local windows, we can achieve focused enhancement effects. Through this non-linear operator, SWT coefficients can be modified for feature enhancement by

$$W_{2^j}^{i,m,*} f(x,y) = M_{2^j}^{i,m} * E_{GAG}\left(\frac{W_{2^j}^{i,m} f(x,y)}{M_{2^j}^{i,m}}\right), \tag{58}$$

$$M_{2^j}^{i,m} = \max_{x,y}(|W_{2^j}^{i,m} f(x,y)|), \tag{59}$$

where $i = 1, 2$, $1 \le m \le M$, and $1 \le j \le J$. $W_{2^j}^{i,m,*} f(x,y)$ is a processed coefficient. Figure 15 shows a functional diagram of the generalized adaptive gain operator.

2.3.6 Experimental Results

First we present experimental results based on a 1-D sub-octave wavelet transform. This is used to show the denoising capability of our method with features restored and enhanced compared with other well known denoising methods. Experimental results of our SWT-based denoising with features restored are shown in Figure 16. In the fourth plot of Figures 16(a)-(d), the denoised results are overlaid with their corresponding originals. After comparing with Coifman's and Donoho's methods, we can see that the results of our SWT-based method are visually superior and relatively free from side-effects [37]. In the next experiment, we show the incapability of a DWT for characterizing band-limited high frequency features. Figures 17(a)-(b) show the original and noisy "Doppler" signals with their corresponding 5-level DWT and a coarse scale approximation. The finest scale band-limited features (see the second plot in Figure 17(a)) are weak and obscured when

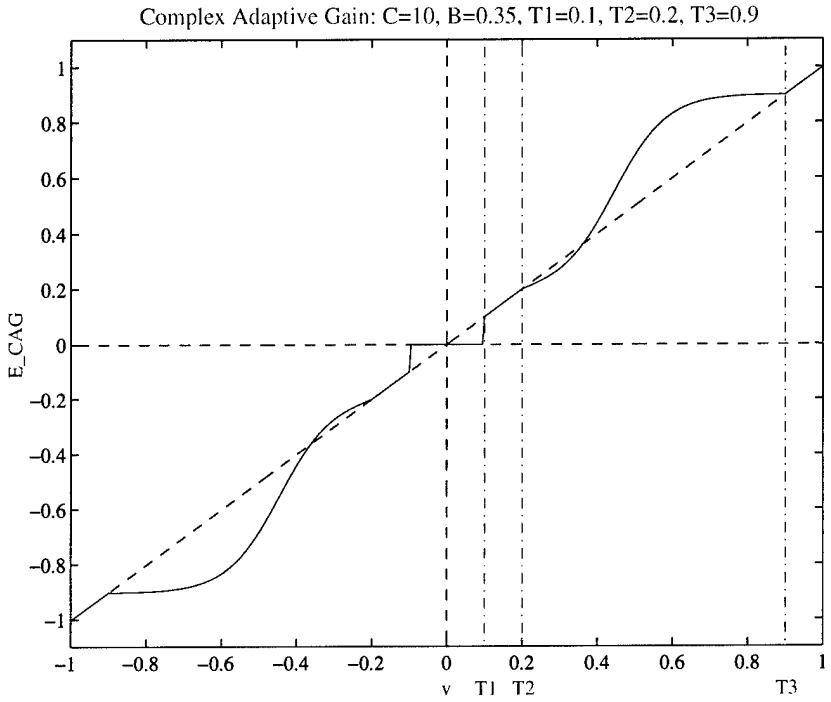

Figure 15: An example of the generalized adaptive gain function.

noise is present (see the second plot in Figure 17(b)). These high frequency band-limited features are lost in a soft thresholding denoising method, which is shown in Figure 18(b). Figures 17(c)-(f) show a 2-sub-octave wavelet transform of the original and noisy "Doppler" signals. Figures 17(c) and 17(e) show first sub-octave coefficients while Figures 17(d) and 17(f) display second sub-octave coefficients. Figure 18 shows denoised and enhanced results of noisy "Doppler" under a DWT and a SWT. The loss of high frequency band-limited features and other factors, make the result from the DWT-based method less attractive than our SWT-based method.

The experimental results of enhancement with noise suppression of mammographic images via a 2-D sub-octave wavelet transform are also presented. This part of our experiment demonstrates the potential of this enhancement method without amplifying noise, such as background noise in [46]. Figure 19(a) shows a dense mammographic image. Enhancement by traditional histogram equalization is presented in Figure 19(b). Figure 19(c) shows the result of SWT-based enhancement with noise suppression. The histogram equalization method makes all features in the slightly dark areas obscured. The mass in the middle right area of the image is enhanced and becomes visible in both methods. As shown in Figure 19(c), enhancement under a SWT makes barely seen tissue structures visible. Additional enhancement results are shown in Figure 20. Figure 20 (b) is the result presented in last year's report and is included for comparison. Thus, the result obtained

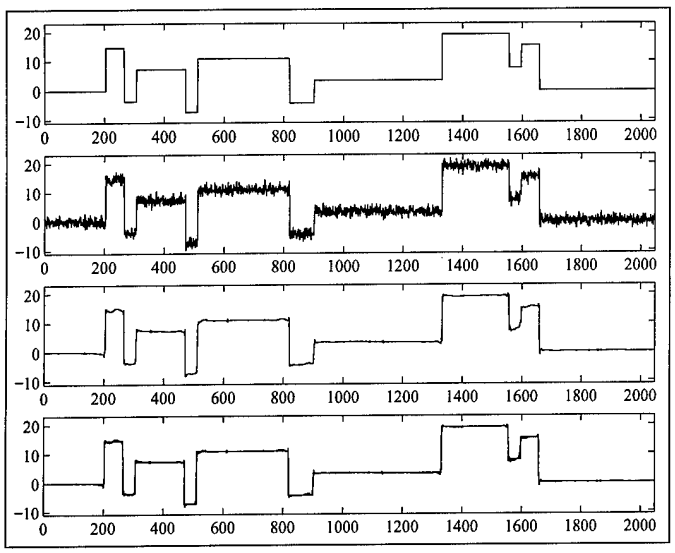

(a) "Blocks"

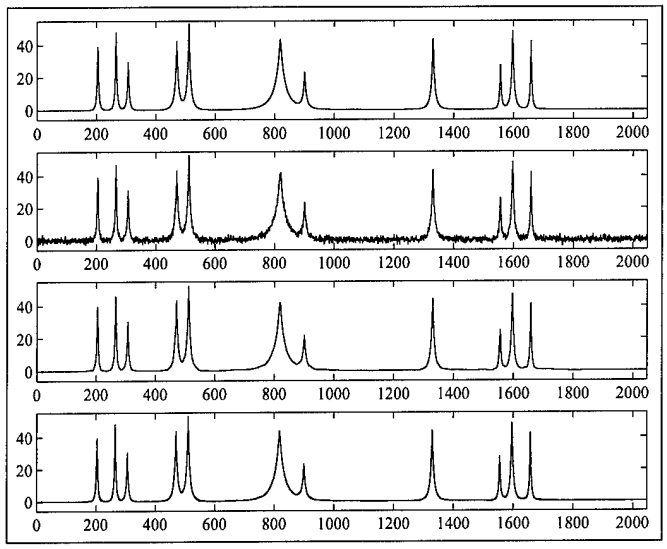

(b) "Bumps"

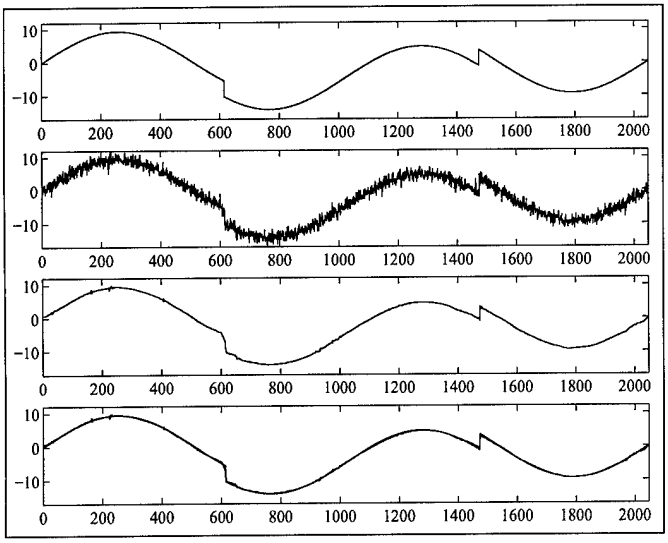

(c) "HeaviSine"

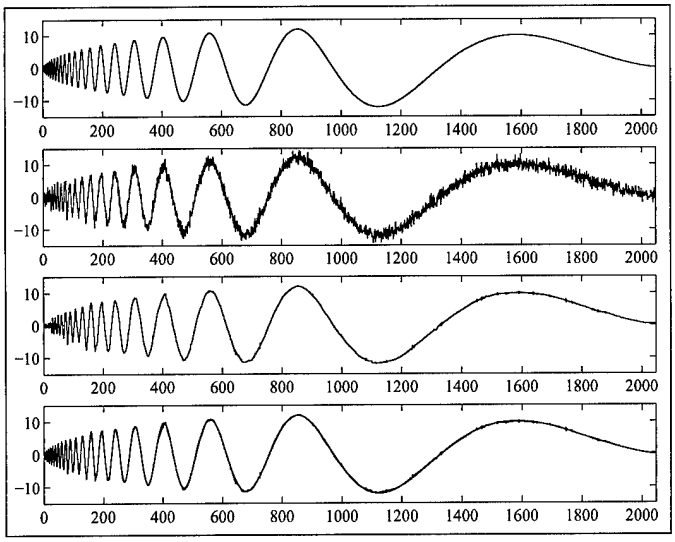

(d) "Doppler"

Figure 16: Denoised and restored features from the SWT-based algorithm from top to bottom: original signal; noisy signal; denoised signal; overlay of original and denoised signal.

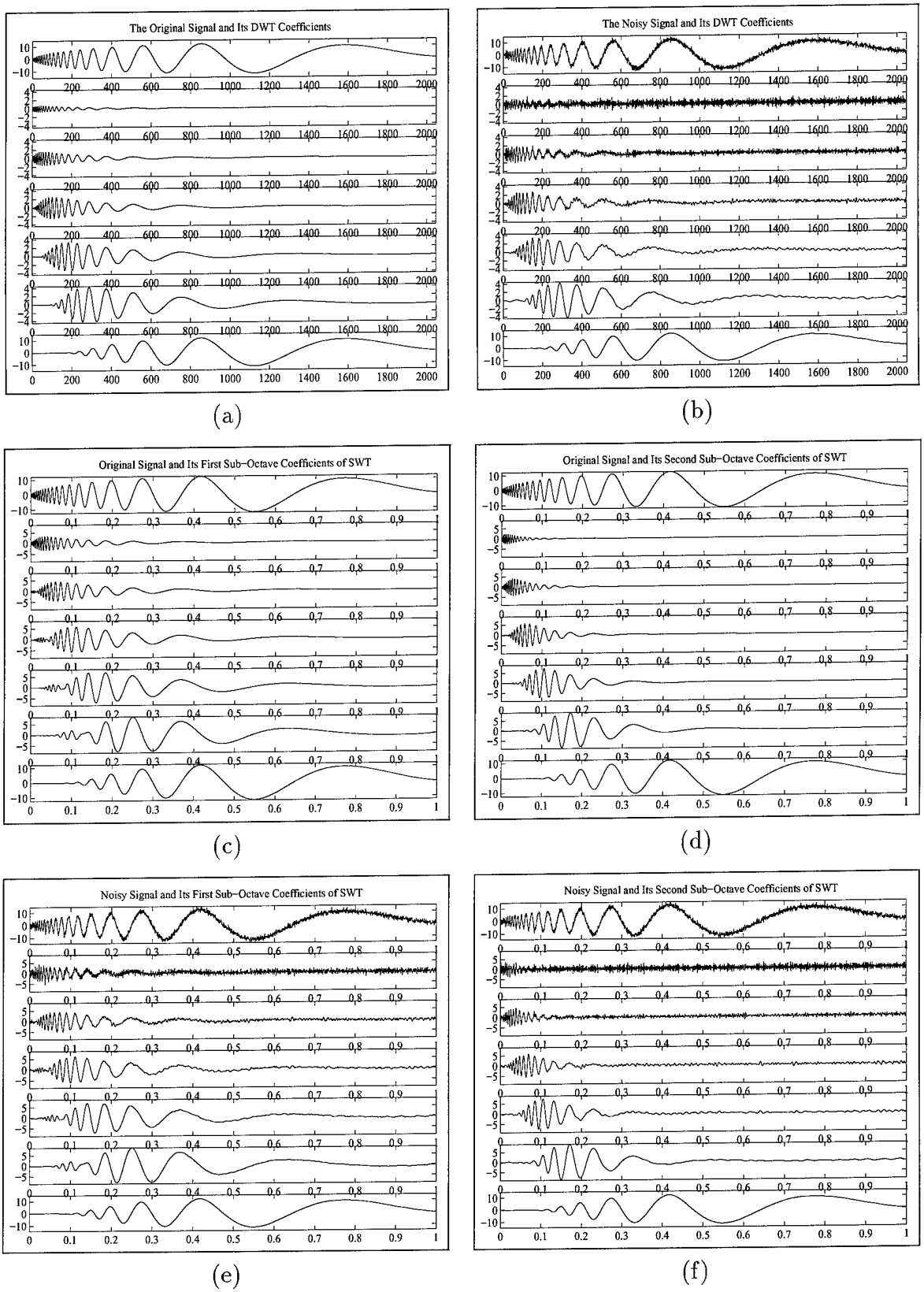

Figure 17: Limitation of a DWT for characterizing band-limited high frequency features.

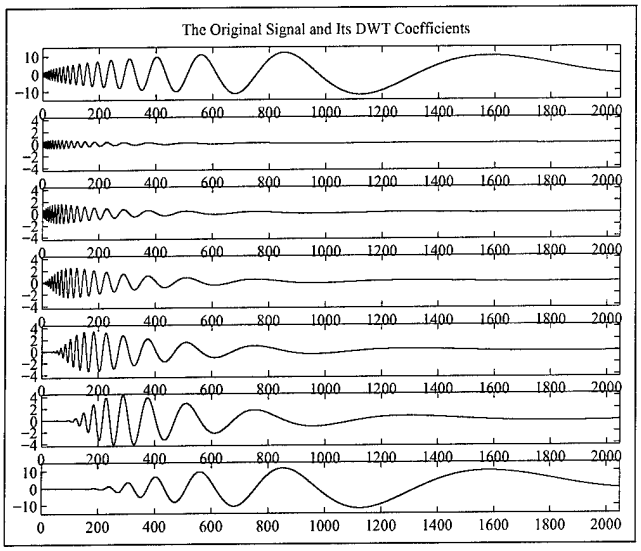

(a)

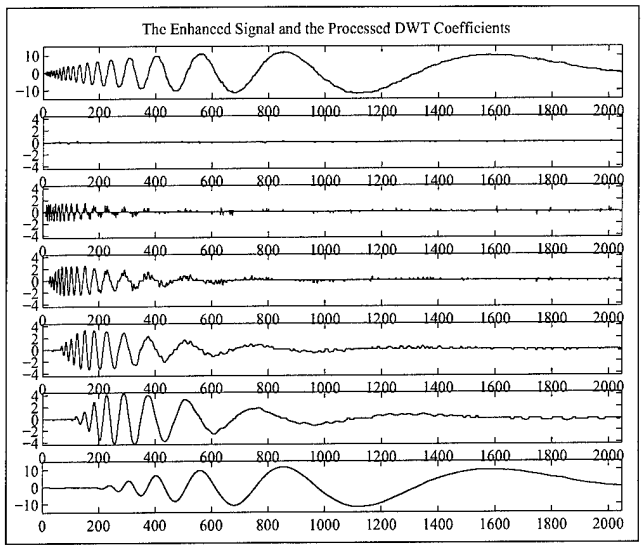

(b)

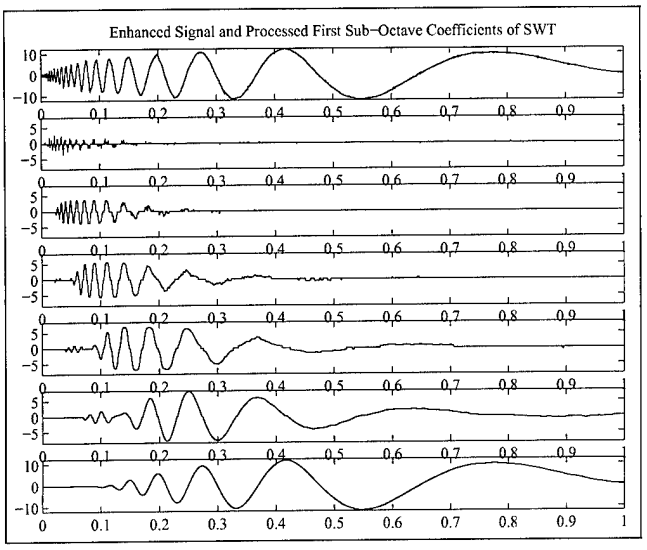

(c)

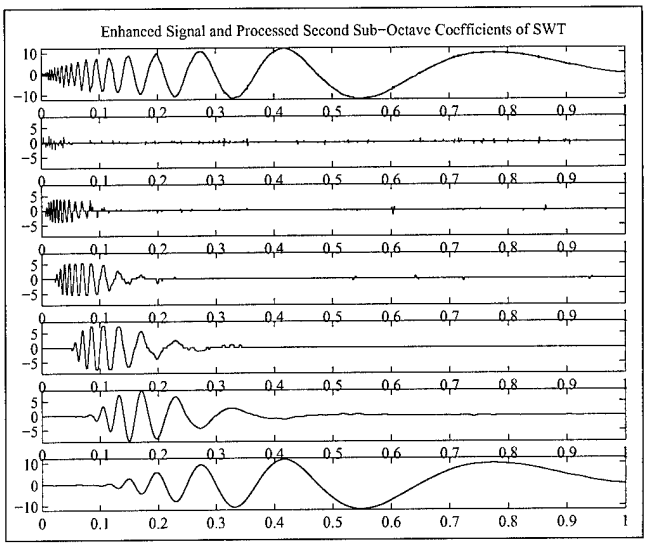

(d)

Figure 18: Denoised and enhanced results of noisy "Doppler" signal under a DWT and a SWT analysis.

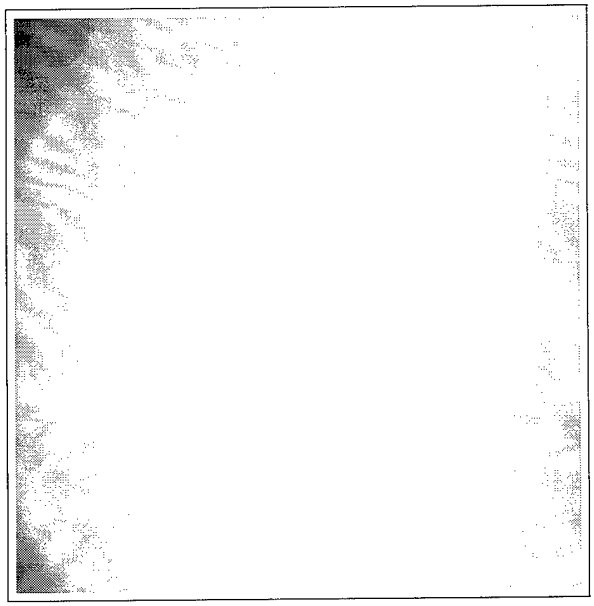

(a)

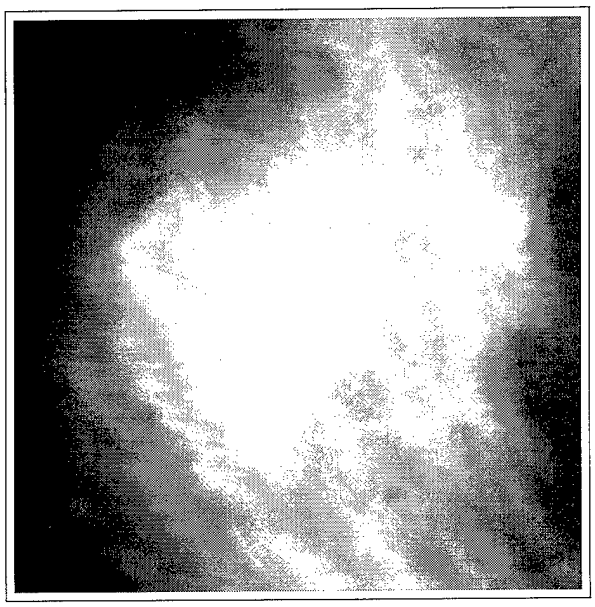

(b)

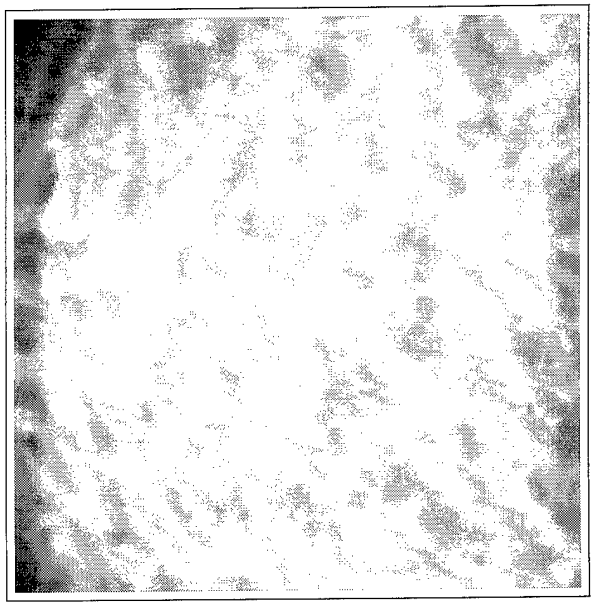

(c)

Figure 19: (a) A dense mammogram. (b) Enhancement by traditional histogram equalization. (c) SWT-based enhancement with noise suppression.

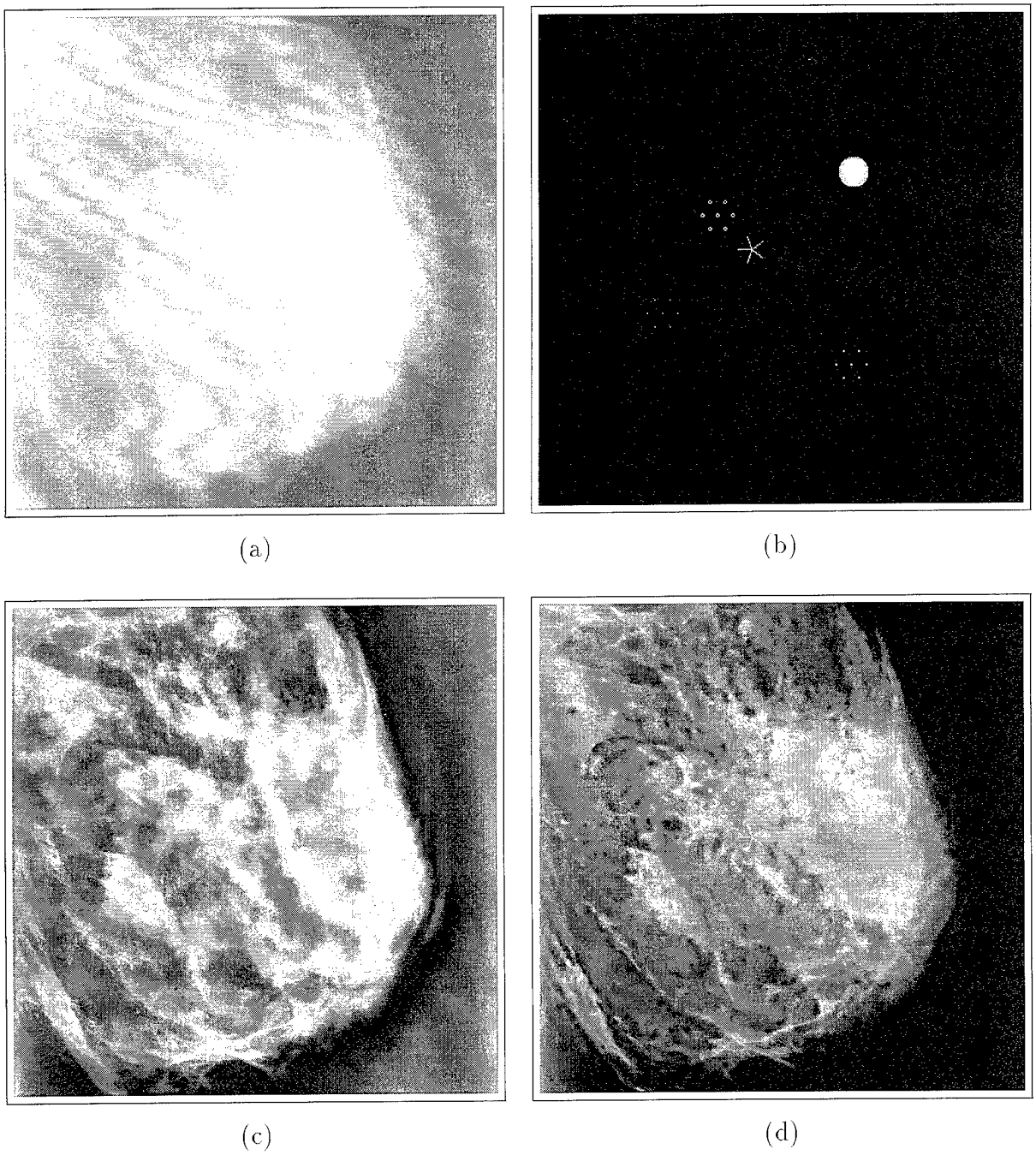

Figure 20: (a) Mammogram M56 with blended phantom features. (b) Phantom image. (c) Nonlinear enhancement with adaptive wavelet shrinkage denoising ($G_m = 20$, $N = 5$, $t = 0.1$). (d) SWT-based enhancement with noise suppression.

via the SWT-based method is superior to that of traditional DWT methods of analysis.

2.3.7 Summary

We have shown the limitation of traditional DWT for characterizing band-limited features, such as subtle features in mammographic images. To more reliably isolate noise and identify features through scale space, we formulated and developed sub-octave wavelet transforms. If the number of sub-octave bands in each octave is a power of 2, it is shown that the sub-octave wavelet transform of a function can be implemented by a single pair of analysis and synthesis wavelets. FIR filters for a class of wavelets designed for a DWT can be used to implement sub-octave wavelet analysis. A wavelet shrinkage scheme for noise suppression was presented and generalized adaptive gain processing was developed to enhance features without amplifying noise.

Our future efforts will include developing feature clustering techniques and statistical analysis for efficiently removing noise and enhancing features. A more dedicated feature cluster-based technique for denoising and feature enhancement is under development. We will also explore iterative methods for identifying coherent structures from an image via sub-octave wavelet analysis.

2.4 Denoising Using Complex Daubechies Wavelets

2.4.1 Introduction

The purpose of denoising is to restore an image that differs as little as possible from its original. Thus, we want to preserve the features of an image while removing noise.

Here, we find important features existing at one scale that propagate to the next larger scale. Wavelet transforms can be used to locate the singularities of an image because of their localization characteristics. By taking advantage of these properties, we can trace the evolution of features across distinct scales by their wavelet coefficients. In this investigation we present a new approach for denoising using complex Daubechies wavelets. By virtue of linear phase and dual representations of scaling functions, noise can be removed and features preserved. Preliminary simulation results are shown.

2.4.2 Symmetric Daubechies Wavelets

A family of compactly supported orthonormal wavelet bases were first constructed by Daubechies [31], using multiresolution analysis. In oder to construct a compactly supported wavelet ψ, the analysis starts from a scaling function ϕ with compact support. A multiresolution analysis of $L^2(\mathrm{R})$ is a sequence of closed subspaces V_j of $L^2(\mathrm{R})$, $j \in \mathrm{Z}$,

satisfying

$$\cdots \subset V_2 \subset V_1 \subset V_0 \subset V_{-1} \subset V_{-2} \subset \cdots$$

Since the scaling function $\phi \in V_0 \subset V_{-1}$, a sequence of coefficients $h_n \in l^2(\mathrm{Z})$ exists such that the scaling function satisfies

$$\phi(x) = \sqrt{2} \sum_n h_n \phi(2x - n). \tag{60}$$

The associated wavelet ψ can be generated through ϕ

$$\psi(x) = \sqrt{2} \sum_n g_n \phi(2x - n), \tag{61}$$

where

$$g_n = (-1)^n h^*_{1-n} \tag{62}$$

with h^* denoting complex conjugate of h.

From multiresolution analysis, $f(x)$ can be expressed as

$$f(x) = \sum_n s_k^{j_0} \phi_{j_0,n}(x) + \sum_{j=J}^{j_0} \sum_n w_n^j \psi_{j,n}(x), \tag{63}$$

where j_0 is the coarsest level scale and J is the finest level scale. The coefficients s_n^j and w_n^j are obtained by computing the inner products

$$s_n^j =< f, \phi_{j,k} >, \qquad w_n^j =< f, \psi_{j,k} > . \tag{64}$$

Using a fast wavelet transform (FWT) algorithm, we can compute these coefficients by recursively convolving with filters h_n^* and g_n^*, respectively, and downsampling.

$$s_n^j = \sqrt{2} \sum_k h^*_{k-2n} s_k^{j-1}, \qquad w_n^j = \sqrt{2} \sum_k g^*_{k-2n} s_k^{j-1}, \tag{65}$$

where s_n^0 is the original signal. The original signal $f(x)$ can be reconstructed, in a similar way, via the inverse FWT.

$$s_n^{j-1} = \sqrt{2} \sum_k h_{n-2k} s_k^j + \sqrt{2} \sum_k g_{n-2k} w_k^j. \tag{66}$$

The block diagrams of FWT and inverse FWT algorithms are shown in Figure 21. Multiresolution analysis leads naturally to a hierarchical and fast scheme for the computation of the wavelet coefficients. In electrical engineering terms, (65) and (66) are the analysis and synthesis stages of a subband filtering scheme with perfect reconstruction. Filters h_n and g_n are quadrature mirror filters (QMF).

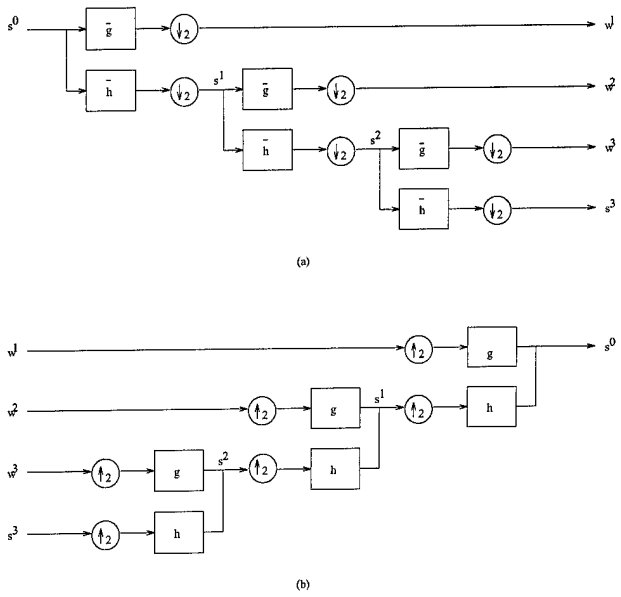

Figure 21: Block diagram of fast wavelet transform: (a) decomposition; (b) reconstruction.

A linear phase property can be achieved with symmetric filters. There have been two distinct methods developed to generate complex Daubechies wavelets. Lawton [47] derived a complex valued linear phase FIR conjugate quadrature filters (CQF) from a class of real valued FIR CQF's by replacing certain filter zeros by their reciprocal conjugates. Lina *et al.* [48] used two parameterizations to compute complex solutions for Daubechies wavelets. Let the Z-transform of h_n be

$$H(z) = \sum_n h_n z^n, \qquad \text{with } H(1) = 1. \tag{67}$$

Symmetric Daubechies wavelets have the following advantages:

1. Compactness: The scaling function has support inside interval $[-J, J+1]$, where J is the order of the underlying analysis.

2. Orthogonality: The orthogonality of $\phi_{m,n}$ implies

$$|H(z)|^2 + |H(-z)|^2 = 1.$$

3. Regularity: The derived wavelets will optimize the regularity of a given compact support

$$H'(-1) = H''(-1) = \cdots = H^{(J)}(-1) = 0.$$

4. Symmetry: The filter h_n must satisfy $h_n = h_{1-n}$, i.e.,

$$H(z) = zH(z^{-1}).$$

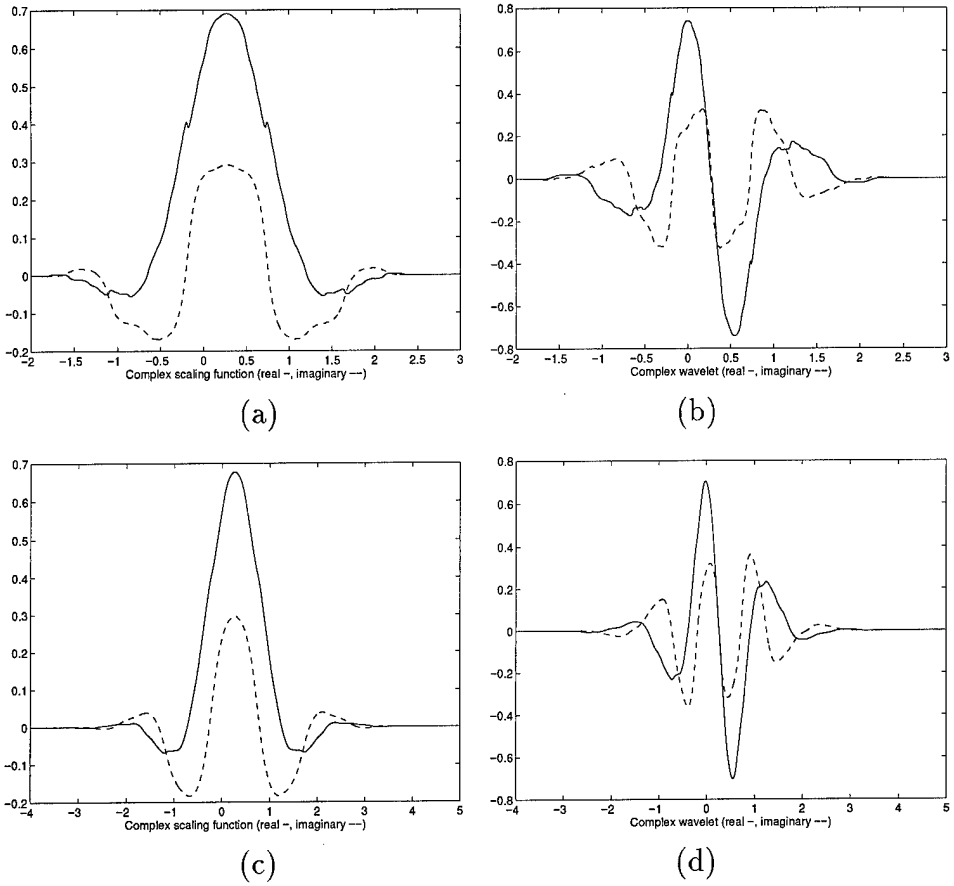

Figure 22: Scaling functions and wavelets: (a),(b) J=2; (c),(d) J=4.

The standard Daubechies wavelets have the first three properties, while the parameterized solutions of symmetric Daubechies wavelets can be obtained from properties 2, 3, and 4. Figure 22 shows complex scaling functions and wavelets, derived by Lina *et al.* [49, 48], for $J = 2$ and 4, where $(2J + 2)$ is the tap number for the complex filters. Note that the scaling function and wavelet for $J = 4$ are smoother than those for $J = 2$. The real part and the imaginary part of the scaling function are close to first derivative and second derivative of a Gaussian function, respectively.

2.4.3 Methodology

Previous Techniques

There have been many noise reduction methods discussed in the literature. The simplest noise reduction technique is an equally weighted averaging over a neighborhood (mean filtering). Averaging produces an effect similar to lowpass filtering. However, reducing the effects of random noise results in blurring. The method of median filtering is similar to mean filtering in that it uses the local median instead of a local mean, and exhibits better performance for edge-preservation and noise reduction (for speckle noise).

More recently, denoising based on wavelet transforms have been proposed. Mallat *et al.* [24, 13] used the local maxima of the wavelet transform modulus to analyze image singularities. The algorithm computed Lipschitz exponents from the evolution across scales of the wavelet transform modulus maxima, removed all maxima whose amplitude increased on average when the scale decreased, or which did not propagate to larger scales. A "denoised" signal was then reconstructed with an alternative projection algorithm. Mallat *et al.* [24, 13] conjectured that a signal can be perfectly reconstructed from the locations and values of the modulus maxima of the wavelet transform at different scales. This conjecture has been disproved by Meyer [50] although the reconstruction gives a good approximation in many cases.

Donoho and Johnstone [40, 36] proposed a three-step method for recovery of a noisy signal. Their method is based on a nonlinear shrinkage of wavelet coefficients. In contrast to the hard thresholding of wavelet coefficients, their soft-thresholding approach provides a smoother means for removing noise.

Mallat and Zhang [51] introduced a matching pursuit algorithm that decomposed a signal into a linear expansion of waveforms that belonged to a redundant dictionary of functions. With a dictionary of Gabor functions, a matching pursuit defines an adaptive time-frequency transform. A coherent structure is chosen by testing the amplitude ratio of successively extracted amplitudes with thresholded noise components. The denoised signal can then be reconstructed from coherent components. There is a trade-off between

computation time and precision. If we use too many bases in a dictionary, the algorithm will take a long time to converge; if a small set of bases is used, the matching may not be good enough.

Two variations of matching pursuit algorithm have been proposed. Both of them express a signal as a superposition of a collection of libraries of waveforms. The first one was an adapted waveform transform by Coifman and Wickerhauser [52]. They used wavelets, wavelet packets, and windowed trigonometric waveforms as the libraries of waveforms because these bases could be implemented with fast algorithms, and thus could achieve high-speed interactive performance. They found the best basis in each library by minimizing a cost function. A signal can then be divided into two parts – coherent components and incoherent components – via a threshold. The incoherent component is then considered a new signal and decomposed again. This process is performed iteratively until it reaches a fixed number of decompositions or no coherent components are obtained. The denoised signal is obtained by superimposing the coherent components together. Because the bases are orthogonal, this method may not obtain sparse representations if a signal is composed of several non-orthogonal components.

In another method, basis pursuit was presented by Chen and Donoho [42]. They used a richer libraries of waveforms as basis, including wavelets, steerable wavelets, Gabor dictionaries, multiscale Gabor dictionaries, wavelet packets, cosine packets, and chirplets. They choose the basis whose coefficients have a minimum l^1 norm. The solution can be obtained by solving an equivalent linear program. In order to deal with a noisy signal, they proposed an approximate decomposition, as mentioned previously, by solving a quadratic program. Noise in both variations is assumed to be white Gaussian.

Freeman and Adelson [53] proposed the concept of steerable filters and applied it to several problems. With a set of "basis filters", one can adaptively steer a filter along any orientation. Hilbert transform pairs were constructed to find a local "oriented energy" measure. Noise was then reduced by performing a soft threshold function [54] on a pyramid of multiscale coefficients.

It is well known that linear phase filters are important in image coding [55]. There exists no real orthogonal compactly supported wavelet bases in which a scaling function ϕ has linear phase, except for the Haar basis [31, 39]. Complex Daubechies wavelets were first developed by Lawton [47] and Lina and Marrand [49, 48] to achieve the linear phase property. Lina *et al.* proposed a sharping algorithm for image enhancement based on complex Daubechies wavelets analysis.

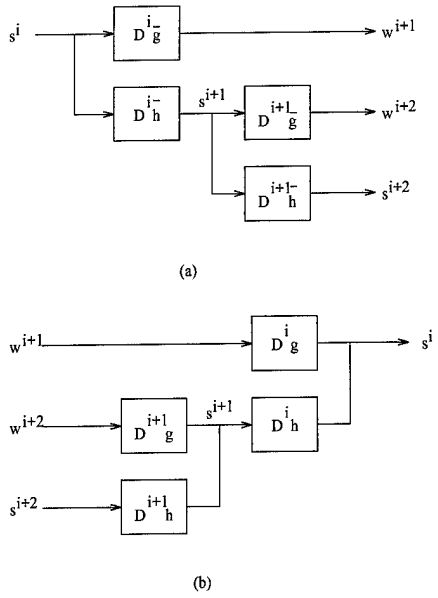

Figure 23: Block diagram of "*algorithme à trous*": (a) decomposition; (b) reconstruction.

Complex Daubechies Wavelets Approaches

In order to obtain linear phase, we can relax the orthogonality requirement and use biorthogonal bases, or give up compactly supported bases to get infinite impulse response (IIR) filters. Also, we may choose to drop the real valued filter requirement and obtain complex valued linear phase FIR filters. We found that complex Daubechies wavelets have some interesting properties which may be useful for the analysis of mammographic features, such as dual representation – local extrema and zero-crossings. We have used these characteristics in our denoising algorithm.

As we mentioned previously, for compactly supported orthonormal wavelet bases, we may decompose and reconstruct an image via a fast wavelet transform algorithm [56]. However, this transform is not shift-invariant, which is a problem in mammographic analysis. In order to accomplish shift-invariance, we needed to find an equivalent structure without downsampling. We used the structure shown in Figure 23 to implement the transformation. Compared to Figure 21, every filter f and downsampling (upsampling) operation is replaced by a new filter $D^i f$. $D^i f$ is obtained by inserting $2^i - 1$ zeros between every pair of the coefficients of f. That is,

$$[D^i f]_n = \begin{cases} f_{\frac{n}{2^i}} & \text{if} \quad n = 2^i m, \\ 0 & \text{otherwise,} \end{cases}$$

where m and n are lengths of the original filter and filters at i-th level, respectively. This approach is called "*algorithme à trous*" (algorithm with holes) [27, 57]. The decomposition and reconstruction equations at level i are as follows.

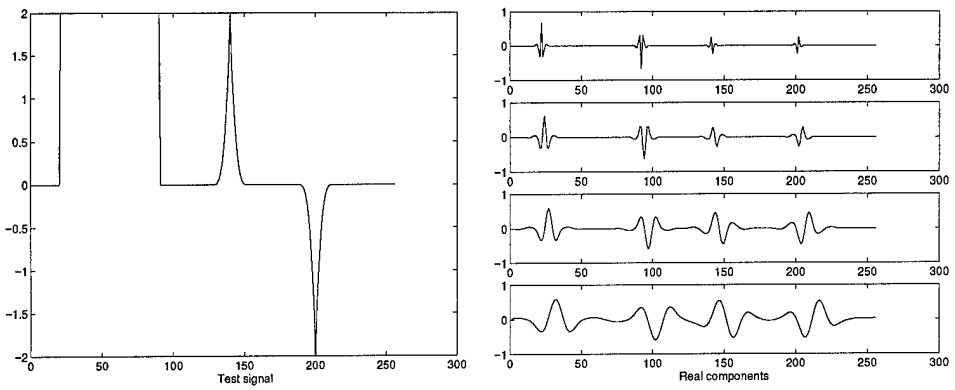

(a) (b)

Figure 24: (a) Test signal. (b) Four levels of waveform basis.

Decomposition:

$$s^{i+1} = (D^i h^*) * s^i. \tag{68}$$

$$w^{i+1} = (D^i g^*) * s^i. \tag{69}$$

Reconstruction:

$$s^i = (D^i h) * s^{i+1} + (D^i g) * w^{i+1}, \tag{70}$$

where "$*$" indicates discrete convolution.

One-dimensional case

Edges are important for detecting mammographic features. In this study, we considered two kinds of features: steps (including low to high and high to low) and pulses, which are shown in Figure 24(a). Real components of four levels of wavelets coefficients were also shown in Figure 24(b). Basically, each level had two types of waveforms. (Actually, there are four kinds of waveforms. Two waveforms form a pair and each pair is opposite of each other.) The waveforms among distinct levels have similar shapes, except for dilations. We saved the waveforms in the fourth level and normalized them as a basis. Since these waveforms are symmetric or antisymmetric, we only needed to save half of the samples.

We can decompose a signal into several levels of wavelet coefficients using complex Daubechies wavelets. The filter coefficients that we used are shown in Table 2.4.3 for $J = 6$. Because the filters are complex, the coefficients in each level contain two parts: real and imaginary components. According to our experiments, four levels of wavelet coefficients were enough for analysis. If we decomposed further, some of the features were smoothed and disappeared.

We started the analysis from the third level. Real components were considered first. The coefficients were thresholded and local extrema were identified. The features of a

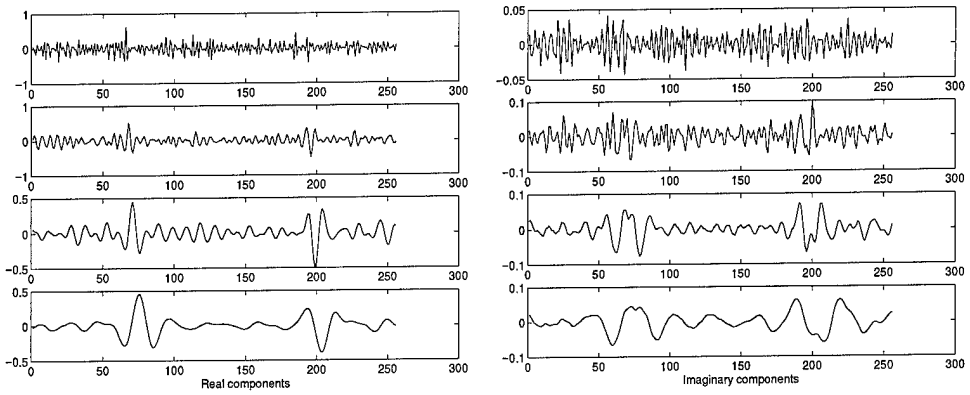

(a) (b)

Figure 25: Four levels of wavelet coefficients for a noisy input sample: (a) real components; (b) imaginary components.

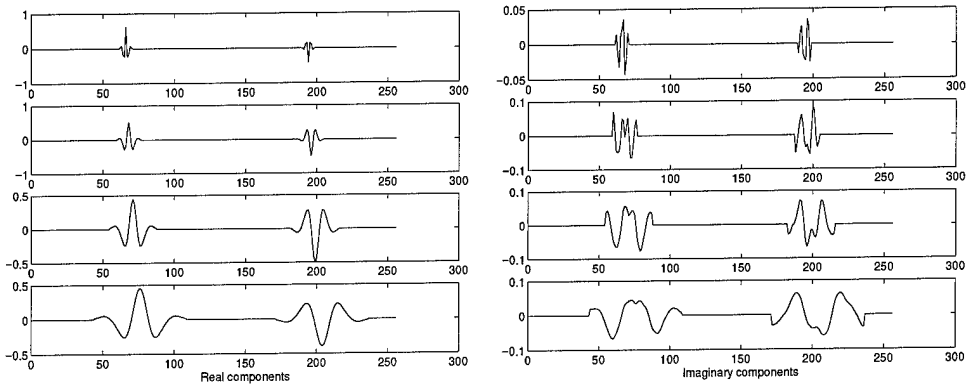

(a) (b)

Figure 26: Four levels of denoised wavelet coefficients: (a) real components; (b) imaginary components.

signal should propagate across scales. Extrema in the third level were compared with those in the fourth level. We kept the extrema that also appeared at the fourth level. Extrema that did not show up at the fourth level were considered as false peaks and removed.

Because the lengths of the basis were long, four simple 3-tap masks, {-1.0, 3.0, -1.0}, {-0.1, 2.5, -2.5}, {1.0, -3.0, 1.0}, and {0.1, -2.5, 2.5}, were used to classify the waveforms. These four masks are the simplified forms of the basis shown in Figure 24(b) and were used to identify the waveform type. At the third level, we simply aligned the center of the mask with the extrema and the other two of the masks with the eighth neighbors of the extreme. These were then multiplied and summed. The mask which had a maximum value was used to decide the waveform type of a feature.

Since we classified the waveform type, we traced backwards to the first two levels and find the positions of extrema. A feature will propagate across different scales with the same

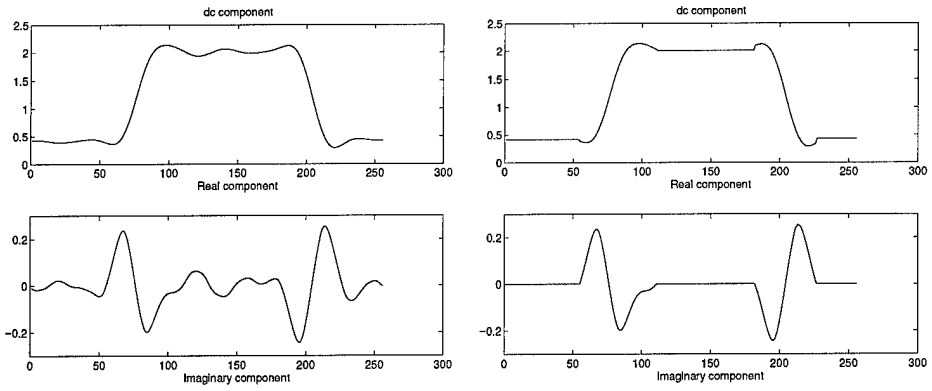

(a) (b)

Figure 27: (a) Noisy dc components. (b) Denoised dc components.

waveform type. We kept the best match at the first two levels. Then we replaced real wavelet coefficients in four levels with corresponding idealized waveform basis proportional to the magnitudes of the extrema. Because the basis were fitted for the fourth level, we downsample by two to obtain the basis for the other levels. Imaginary components of the corresponding periods were preserved. The reasons are as follows: the energy in the imaginary part of the coefficients is significantly smaller than that in the real part, and coefficients of a noisy signal are similar to those without noise. Four levels of wavelet coefficients for noisy input are shown in Figure 25, and the denoised versions are shown in Figure 26.

Next, we focus on the DC component. This component is obtained from passing an input through several lowpass filters, and is very smooth. We already know that the real part and imaginary part of a scaling function is close to the first derivative and the second derivative of Gaussian, respectively. We first locate regions within imaginary components that are less than some threshold and oscillate near zero. We set these regions to zero and replace each corresponding region of real components with its average value. Figure 27 shows a sample noisy dc component and denoised version. Finally, we reconstructed the original signal with the modified coefficients.

The algorithm is summarized as follows:

1. Using a frame representation, we decompose a signal into several levels of complex wavelet coefficients.

2. Starting from the third level, we identify the local maxima for real wavelet coefficients that are greater than some threshold.

3. Selected coefficients are compared with the fourth level to remove unwanted maxima

and classify each waveform type.

4. Trace backward to the first two levels to find the positions of maxima.

5. Replace real wavelet coefficients with corresponding idealized waveform basis and preserve imaginary components.

6. Locate regions within the imaginary component of DC channel that are less than some threshold and oscillate near zero.

7. The real part of each corresponding region is replaced with its average value.

8. Reconstruct original signal using modified coefficients.

Two-dimensional case

The two-dimensional case is easily extended from the one-dimensional case by tensor product construction. In order to reduce computational cost, we used a method proposed by Mallat *et al.* [13] to find features along the x-axis and y-axis, respectively. Let the scaling function $\phi(x)$ be expressed by

$$\hat{\phi}(\omega) = e^{-is\omega} \prod_{p=1}^{+\infty} H(2^{-p}\omega), \tag{71}$$

where $H(\omega)$ is the Fourier transform of a lowpass filter $h(n)$ and s is the sampling shift. This implies that

$$\hat{\phi}(2\omega) = e^{-is\omega} H(\omega)\hat{\phi}(\omega). \tag{72}$$

A wavelet $\psi(x)$ whose Fourier transform $\hat{\psi}(\omega)$ can be defined in the same way:

$$\hat{\psi}(2\omega) = e^{-is\omega} G(\omega)\hat{\phi}(\omega), \tag{73}$$

where $G(\omega)$ is the Fourier transform of a highpass filter $g(n)$. The two wavelets $\psi^1(x, y)$ and $\psi^2(x, y)$ are separable, and are defined as

$$\psi^1(x, y) = 2\psi(x)\phi(2y), \tag{74}$$

$$\psi^2(x, y) = 2\phi(2x)\phi(y). \tag{75}$$

The Fourier transform of these two wavelets are then given by

$$\hat{\psi}^1(2\omega_x, 2\omega_y) = e^{-is\omega_x} G(\omega_x)\hat{\phi}(\omega_x)\hat{\phi}(\omega_y), \tag{76}$$

$$\hat{\psi}^2(2\omega_x, 2\omega_y) = e^{-is\omega_y} \hat{\phi}(\omega_x)G(\omega_y)\hat{\phi}(\omega_y). \tag{77}$$

The two-dimensional wavelet transform of $f(x,y)$ can be expressed as the set of functions

$$Wf = (W^1_{2^j} f(x,y), W^2_{2^j} f(x,y)), \tag{78}$$

where $j \in \mathrm{Z}$. We now find two reconstructing functions $\chi^1(x,y)$ and $\chi^2(x,y)$ such that $f(x,y)$ can be reconstructed from its wavelet transform

$$f(x,y) = \sum_{j=-\infty}^{+\infty} (W^1_{2^j} f * \chi^1_{2^j}(x,y) + W^2_{2^j} f * \chi^2_{2^j}(x,y)). \tag{79}$$

In order to obtain perfect reconstruction, the Fourier transforms of $\chi^1(x,y)$ and $\chi^2(x,y)$ must satisfy

$$\sum_{j=-\infty}^{+\infty} (\hat{\psi}^1(2^j\omega_x, 2^j\omega_y)\hat{\chi^1}(2^j\omega_x, 2^j\omega_y) + \hat{\psi}^2(2^j\omega_x, 2^j\omega_y)\hat{\chi^2}(2^j\omega_x, 2^j\omega_y)) = 1. \tag{80}$$

Let $\hat{\chi^1}(\omega_x, \omega_y)$ and $\hat{\chi^2}(\omega_x, \omega_y)$ be defined such that

$$\hat{\chi^1}(2\omega_x, 2\omega_y) = e^{is\omega_x} K(\omega_x) L(\omega_y) \hat{\phi}(\omega_x)\hat{\phi}(\omega_y) \tag{81}$$

$$\hat{\chi^2}(2\omega_x, 2\omega_y) = e^{is\omega_y} K(\omega_y) L(\omega_x) \hat{\phi}(\omega_x)\hat{\phi}(\omega_y), \tag{82}$$

where $K(\omega)$ and $L(\omega)$ are 2π periodic functions and they have to satisfy

$$G(\omega)K(\omega) + |H(\omega)|^2 = 1, \tag{83}$$

$$L(\omega) = \frac{1 + |H(\omega)|^2}{2}. \tag{84}$$

In our algorithm, $f(n)$ and $g(n)$ are lowpass and highpass filters, respectively. We choose $k(n)$ equals to $g^*(n)$ to meet the first criterion. Next we need to generate a filter $l(n)$ which will satisfy the second criterion. In Mallat's original derivation, he developed his algorithm based on a continuous wavelet transform. We approximate his derivation with a discrete formulation.

The support of the lowpass filter (used for decomposition) was 14 taps. In order to increase the resolution in the frequency domain, we needed to interpolate between the original samples. This was done by padding zeros in filter $f(n)$, and then computing its Fourier transform. Because this filter was not symmetric with respect to the origin, we compensated with a $\frac{1}{2}$ sample phase shift. The final filters used in the study are shown in Table 2.4.3.

2.4.4 Experimental Results

To date, our algorithm has been tested on several examples. Figures 28(a) and 28(b) show an original signal and noisy signal, respectively. The SNR is 17.6 dB. The denoised signal

	h(n)		g(n)		k(n)	
n	Real	Imaginary	Real	Imaginary	Real	Imaginary
-6	-0.003384	-0.001523	0.003384	-0.001523	-0.003384	-0.001523
-5	-0.000295	0.000655	-0.000295	-0.000655	0.000295	-0.000655
-4	0.022730	0.019115	-0.022730	0.019115	0.022730	0.019115
-3	-0.009154	0.024154	-0.009154	-0.024154	0.009154	-0.024154
-2	-0.084726	-0.019306	0.084726	-0.019306	-0.084726	-0.019306
-1	0.094778	-0.035922	0.094778	0.035922	-0.094778	0.035922
0	0.480049	0.012827	-0.480049	0.012827	0.480049	0.012827
1	0.480049	0.012827	0.480049	-0.012827	-0.480049	-0.012827
2	0.094778	-0.035922	-0.094778	-0.035922	0.094778	-0.035922
3	-0.084726	-0.019306	-0.084726	0.019306	0.084726	0.019306
4	-0.009154	0.024154	0.009154	0.024154	-0.009154	0.024154
5	0.022730	0.019115	0.022730	-0.019115	-0.022730	-0.019115
6	-0.000295	0.000655	0.000295	0.000655	-0.000295	0.000655
7	-0.003384	-0.001523	-0.003384	0.001523	0.003384	0.001523

	l(n)	
n	Real	Imaginary
0	0.744441	-0.009214
1	0.152932	0.010146
2	0.003917	0.025936
3	-0.038336	0.001404
4	-0.002509	-0.022426
5	0.013544	-0.014009
6	0.002328	0.001338
7	-0.003416	0.002981
8	-0.001008	-0.000301
9	0.000320	-0.000616
10	0.000049	0.000059
11	-0.000048	0.000099
12	0.000002	0.000002
13	0.000005	-0.000005

$l(-n) = l(n)$, $n = 1, \cdots, 13$.

Table 4: **Coefficients of h(n), g(n), k(n), and l(n).**

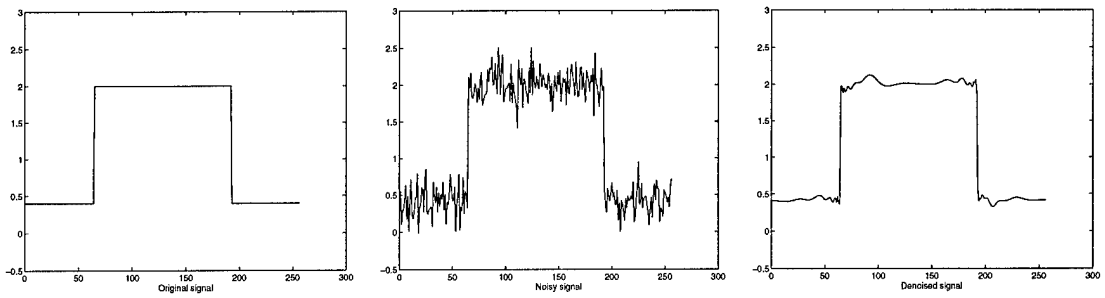

(a) (b) (c)

Figure 28: Square waveforms: (a) original signal; (b) noisy signal; (c) denoised signal.

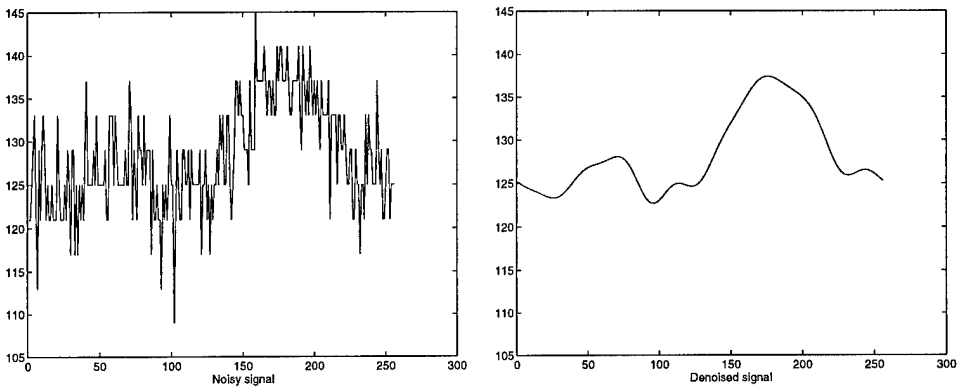

(a) (b)

Figure 29: (a) Noisy signal. (b) Denoised signal.

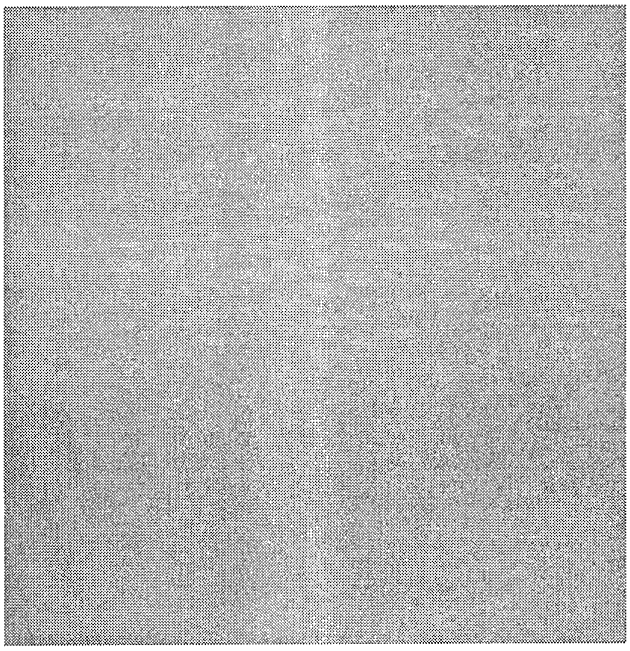

(a)

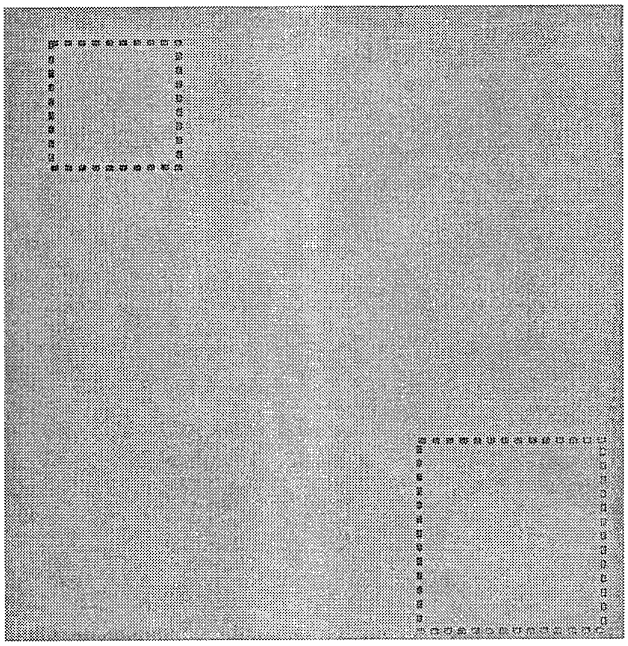

(b)

Figure 30: (a) Original RMI phantom image of mammographic mass. (b) Denoised image.

is shown in Figure 29(c). The new SNR is 30.8 dB. Figures 29(a) and 29(b) show an arbitrary cross section of the RMI phantom image containing a mass. We successfully preserved the mass while reducing noise. A two-dimensional example is shown in Figure 30(a) which shows the original phantom image. It is difficult to see the mass in this image. However, after denoising, we clearly see two masses on the upper left and lower right corners of the image as shown in Figure 30(b).

2.4.5 Summary

Linear phase filters are very important for mammographic image processing. Such filters enable control over phase shifts during processing. By virtue of symmetry (antisymmetry), complex Daubechies wavelets were designed to serve this advantage in analysis.

In this study, we proposed a denoising algorithm based on complex Daubechies wavelets. This algorithm aimed at removing noise while preserving features. We designed an easy method to classify waveform types and replaced the wavelet coefficients of features with "ideal" waveform basis. The dc components were also modified using the unique properties of complex Daubechies wavelets. Our approach differs from previous methods including Mallat's [24, 13] which used local extrema and reconstructed a denoised signal via alternative convex projection iteratively. Despite high redundancy of frame representation, our algorithm was implemented efficiently.

2.5 Segmentation of Masses Using a Continuous Scale Representation

2.5.1 Introduction

In this chapter of the report, we describe a wavelet transform where a continuous scale analysis is carried out through discretization and adaptively finds the scale at which a signal (mass) is best represented.

Edges are an important feature for analyzing the properties of images. Psychophysical experiments suggest that the human visual cortex functions as a population of feature detectors tuned to edges and bars of various widths and orientations [58]. It has also been shown that visual information is processed in parallel by a number of spatial-frequency-tuned channels [59].

Based on such physiological findings, Marr [60] developed an edge detection scheme based on multiscale analysis using a Laplacian of Gaussian filter. Shortly afterward, Witkin [61] decomposed a signal into a tree representation in terms of extrema of the signal or its derivatives. This representation was obtained by scale-space filtering and it is

complete under certain assumptions.

In our study, we have focused on multiscale wavelet analysis. The wavelet kernel is predominantly localized in a certain region of the space-frequency plane. What distinguishes a wavelet transform from a short-time Fourier transform is that a wavelet may have a larger spatial window for low frequency analysis and a smaller spatial window for high frequency analysis. This property enables us to zoom in on sharp variations and design multiscale image processing algorithms tuned for digital mammography. Mallat first developed a recursive algorithm to decompose an image into dyadic scales and reconstruct an original image from its scale space representations [56]. He argued that when using a Gaussian as a smoothing function, detecting the zero-crossings of a wavelet transform is equivalent to a Marr-Hildreth edge detector [60].

A dyadic wavelet analysis provides a complete non-redundant representation [56]. However, here we suggest that for the analysis of digital mammograms, it is desirable to carry out analysis across arbitrary scales, especially, when a certain mammographic feature lies between two dyadic scales. Unser and Aldroubi recently proposed a way to calculate an arbitrary integer scale wavelet transform using B-splines to approximate a wavelet [62]. In this report, we derive a scheme to calculate the wavelet transform of a discrete signal at an arbitrary scale.

Although wavelet transforms have proven to be a powerful tool for the enhancement of digital mammography [9], little is known about choosing the optimal set of parameters for a specific algorithm [63]. For enhancement of digital mammography, one must choose a scale, threshold value, and gain factor in order to target a specific feature [64]. To optimize a wavelet algorithm, one has to systematically investigate the effect of the level, gain, and threshold [64]. In addition, a distinct set of optimal parameters may be necessary for each digital radiograph.

Many image processing and computer vision algorithms are surprisingly fragile when it comes to choosing various parameters and thresholds. There have been no good solutions to setting the proper value of the scale parameter in regularization networks. Local adaptation is needed in these networks to make them less brittle. Using an assumption of zero-mean, additive Gaussian noise, it can be shown that the scale parameter for edge detection problems should be set to be proportional to the variance of the additive noise [65]. However, these assumptions are too restrictive for most purposes, including digital mammography. More promising methods from Bayesian analysis are under investigation for setting the scale and other parameters by standard regularization-based methods [66, 67].

The Laplacian filter is a popular edge detector in image processing. However, knowledge of the image feature size is necessary when choosing the proper scale for feature

detection. In addition, traditional edge detectors require a smoothing prefilter and choosing the proper amount of smoothing may be difficult. Compared to our previous work, traditional image enhancement algorithms may strengthen features within certain spatial scales but choosing an optimal spatial scale is not obvious.

It is common to make some assumptions about feature characteristics. For example, we can assume that microcalcifications in mammograms occur within finer scales since these features are characterized by small, high-contrast spots. Unfortunately, it is more difficult to make such general assumptions for masses in mammograms since masses may assume distinct shapes and sizes, e.g., spiculated, round, or irregular shapes. Thus, it is necessary to find a way to identify an "optimal" scale for representation of masses. Once detected, their regions can be marked and provide an area of local support for multiscale feature enhancement, including reinforcement of the "halo" effect, to assist in the visibility of masses.

In this chapter, we describe a method to segment a mass from its background using a continuous multiscale analysis. First, a suspicious region is identified, which may or may not contain a lesion. Next, the region is used as a matched filter to select a wavelet basis. A soft threshold is then applied. If the selected region contains a feature, the mammographic feature is segmented from its background for further processing.

2.5.2 Traditional Wavelet Analysis

A wavelet transform is a linear operator that projects a signal onto a set of basis functions (wavelets). Each wavelet is a dilated and translated version of a mother wavelet. A mother wavelet is a function $\psi(t) \in L^2(\boldsymbol{R})$ such that

$$\int_{-\infty}^{\infty} \psi(t)dt = 0.$$

The dilation of $\psi(t)$ by a factor a can be described by

$$\psi_a(t) = \frac{1}{a}\psi\left(\frac{t}{a}\right).$$

The convolution operator is defined by

$$f * g(t) = \int_{-\infty}^{\infty} f(u)g(t-u)du.$$

The wavelet transform of a function $f(t)$ at scale a and position b is defined as

$$W_a f(b) = f * \psi_a(t) \mid_{t=b}.$$

The continuous wavelet transform satisfies energy conservation and $f(t)$ can be perfectly reconstructed from its wavelet transform coefficients [68]. Both scale a and position b may

vary continuously over the set of real numbers. At a fine scale a_0, the support of the basis $\psi_{a_0}(t)$ is small and wavelet coefficients $W_{a_0}f(b)$ are sensitive to detail. For a larger scale a_1, the support of $\psi_{a_1}(t)$ has greater extent and wavelet coefficients $W_{a_1}f(b)$ are more sensitive to slow changing information (or larger objects).

For a particular class of wavelets, the scale parameter can be sampled on a dyadic grid without losing the mathematical completeness property of the transform. A dyadic wavelet transform of a continuous function $f(t)$ at scale 2^k and at position b is defined as [13]:

$$W_{2^k}f(b) = f * \psi_{2^k}(t)\,|_{\,t=b}. \tag{85}$$

A function $f(t)$ can then be reconstructed from its transform coefficients alone by:

$$f(t) = \sum_{k=-\infty}^{\infty} W_{2^k}f * \chi_{2^k}(t) = \sum_{k=-\infty}^{\infty} f * \psi_{2^k} * \chi_{2^k}(t) \tag{86}$$

where wavelets $\psi(t)$ and $\chi(t)$ satisfy the condition

$$\sum_{k=-\infty}^{\infty} \Psi(2^k\omega)\mathcal{X}(2^k\omega) = 1, \tag{87}$$

and $\Psi(\omega)$ and $\mathcal{X}(\omega)$ are the Fourier transforms of $\psi(t)$ and $\chi(t)$, respectively.

The dyadic wavelet transform filters used in this report were designed analytically as follows.

Similar to [13], we define a smoothing function $\Phi(\omega)$ such that [25]

$$\Phi(\omega) = \prod_{p=1}^{+\infty} H(2^{-p}\omega). \tag{88}$$

Since $\prod_{p=1}^{+\infty}\cos(2^{-p}\omega) = \frac{\sin(\omega)}{\omega}$, we let [10, 25]

$$\Phi(\omega) = \prod_{p=1}^{+\infty}\cos^2\left(2^{-p}\frac{\omega}{2}\right) = \left(\frac{\sin(\frac{\omega}{2})}{\frac{\omega}{2}}\right)^2 \qquad \text{and} \tag{89}$$

$$H(\omega) = \cos^2\left(\frac{\omega}{2}\right). \tag{90}$$

Choosing $G(\omega) = (4i\sin(\frac{\omega}{2}))^2 = -16\sin^2(\frac{\omega}{2})$, the wavelet $\Psi(\omega)$ can be defined simply as [25]

$$\Psi(\omega) = G\left(\frac{\omega}{2}\right)\Phi\left(\frac{\omega}{2}\right) = (i\omega)^2\left(\frac{\sin(\frac{\omega}{4})}{\frac{\omega}{4}}\right)^4. \tag{91}$$

Filter $K(\omega)$ is then defined by

$$K(\omega) = \frac{1-|H(\omega)|^2}{G(\omega)} = -\frac{1}{16}\left(1+\cos^2(\frac{\omega}{2})\right). \tag{92}$$

Finally, the reconstructing wavelet $\chi(t)$ can be formulated as

$$\mathcal{X}(\omega) = K\left(\frac{\omega}{2}\right)\Phi\left(\frac{\omega}{2}\right). \tag{93}$$

We note that since $\Theta(\omega) = (\frac{sin(\frac{\omega}{4})}{\frac{\omega}{4}})^4$ is a cubic spline whose integral is equal to 1, $\psi(t)$ is a second order derivative of a cubic spline smoothing function. For more detailed treatment of this class of wavelets please refer to Section 2.2 of this report.

2.5.3 An Arbitrary Scale Algorithm for the Discrete Case

A variation of Mallat's algorithm for discrete dyadic analysis is presented next. Mallat's algorithm can analyze a discrete signal $x[n]$, of finite energy [13]. In his algorithm, the scaling function $\Phi(\omega)$ must satisfy the constraint

$$\forall\omega \in R, \quad 0 < C_1 \leq \sum_{n=-\infty}^{+\infty} |\Phi(\omega + 2n\pi)|^2 \leq C_2 \qquad \text{where } C_1 \text{ and } C_2 \text{ are constants.} \tag{94}$$

Marr [60] claimed also that there exists some function $f(t) \in L^2(\boldsymbol{R})$ (not unique) such that [13]

$$\forall n \in Z, \quad S_1 f(n) = \int_{-\infty}^{\infty} f(t)\phi(t-n)dt = x[n]. \tag{95}$$

At each scale 2^j, we may decompose $S^d_{2^j} f[k]$ into $S^d_{2^{j+1}} f[k] = b_{j,k}$ and $W^d_{2^{j+1}} f[k] = c_{j,k}$ [13]. The decomposition algorithm is:

$j = 0$

while $(j < J)$

$$W^d_{2^{j+1}} f = S^d_{2^j} f * G_j$$
$$S^d_{2^{j+1}} f = S^d_{2^j} f * H_j$$
$$j = j + 1$$

end of while,

where $H_p(\omega) = H(2^p\omega)$ and $G_p(\omega) = G(2^p\omega)$. The reconstruction algorithm is:

$j = J$

while $(j > 0)$

$$S^d_{2^{j-1}} f = W^d_{2^j} f * K_{j-1} + S^d_{2^j} f * H_{j-1}$$
$$j = j - 1$$

end of while,

where $K_p(\omega) = K(2^p\omega)$.

In frequency domain, this can be formulated as:

$$\widehat{S}_1^d f = F(\omega)\Phi(\omega) \tag{96}$$

$$\widehat{W}_{2^{j+1}}^d f = \widehat{S}_{2^j}^d f \; G(2^j\omega) \tag{97}$$

$$\begin{aligned}
\widehat{S}_{2^{j+1}}^d f &= \widehat{S}_{2^j}^d f \; H(2^j\omega) \\
&= \widehat{S}_{2^{j-1}}^d f \; H(2^{j-1}\omega)H(2^j\omega) \\
&= F(\omega)\Phi(\omega)\prod_{i=0}^{j} H(2^j\omega) \\
&= F(\omega)\Phi(2\omega)\prod_{i=1}^{j} H(2^j\omega) \\
&= F(\omega)\Phi(2^{j+1}\omega)
\end{aligned} \tag{98}$$

$$\begin{aligned}
\widehat{W}_{2^{j+1}}^d f &= F(\omega)\Phi(2^j\omega)G(2^j\omega) \\
&= F(\omega)\Psi(2^{j+1}\omega) \\
&= \widehat{S}_1^d f \; \frac{\Psi(2^{j+1}\omega)}{\Phi(\omega)}
\end{aligned} \tag{99}$$

Therefore, the wavelet transform of a discrete signal $x[n]$ is,

$$FFT\{DWT\{x[n], 2^j, k\}\} = \widehat{W}_{2^{j+1}}^d f = X(\omega)\; O(2^j\omega), \tag{100}$$

where the frequency response of the analysis filter $O(\omega)$ is

$$O(2^j\omega) = \frac{\Psi(2^{j+1}\;\omega)}{\Phi(\omega)}. \tag{101}$$

Notice that in the algorithm above, filters at scale 2^J are obtained by putting $2^{J-1} - 1$ zeros between consecutive coefficients of filters at level 1. However, this introduces undesirable high frequency components into the analysis filter $O(\omega)$ as shown in Figure 31(a). Thus, a modification was introduced as shown in Figure 31(b). By including an ideal lowpass filter with cutoff frequency $\pi/2^{J-1}$, a mathematically perfect reconstruction is sacrified to obtain superior frequency performance as shown in Figure 31(c). We can show that perfect reconstruction is almost achievable with respect to contrast resolution currently provided by digital mammography. When using the wavelet defined previously, the corresponding analysis filter for our algorithm becomes

$$\Psi_m(2^{j+1}\;\omega) = \begin{cases} \Psi(2^{j+1}\;\omega) & \text{when } |\omega + 2k\pi| \leq 2^{1-j}\pi \\ 0 & \text{when } |\omega + 2k\pi| > 2^{1-j}\pi. \end{cases} \tag{102}$$

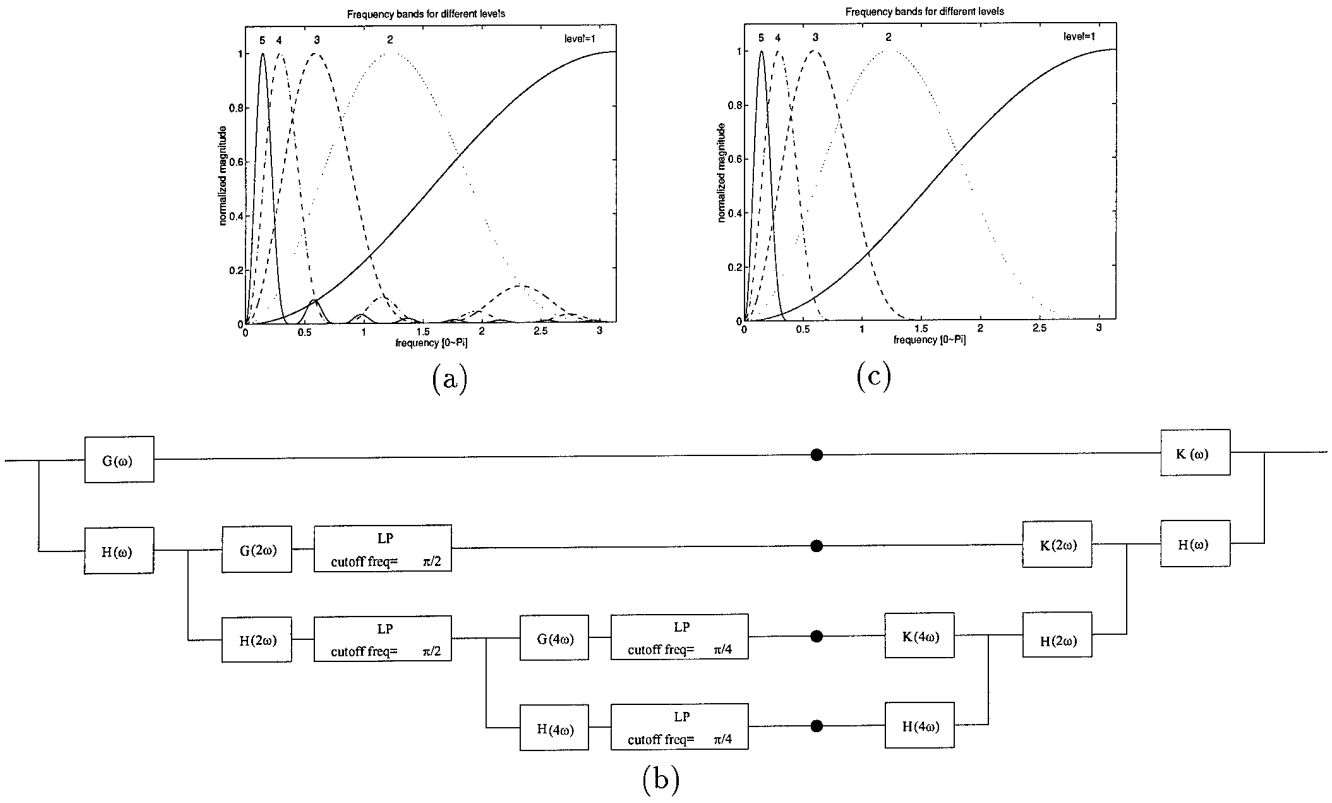

Figure 31: (a) The frequency bands for standard analysis. (b) Block diagram of our modified algorithm (3 levels shown). (c) The frequency response for the subbands of our algorithm.

If $\psi(t)$ satisfies the admissibility condition, $\Psi(\omega) = 0$ when $\omega = 0$. Thus $\Psi_m(\omega) = 0$ when $\omega = 0$. And so we can define

$$O(2^j\omega) = \frac{\Psi_m(2^{j+1}\ \omega)}{\Phi(\omega)}. \tag{103}$$

This analysis filter and its frequency response are comparable to our original analysis filters as shown in Figure 32. Our filter appears more smooth, which is desirable for image

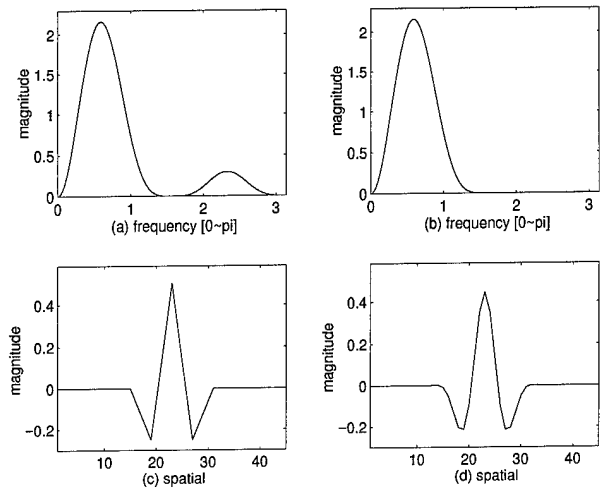

Figure 32: (a) Standard analysis filter's frequency response at level 3. (b) Our analysis filter's frequency response at level 3. (c) Second derivative wavelet at level 3. (d) Our new wavelet at level 3.

analysis. In addition, the ripples caused by the ideal low pass filter are very subtle. Our new algorithm also enables us to zoom in-between octave levels and trace a particular feature in a mammogram. Let us now define

$$\Psi_m(2a\omega) = \begin{cases} \Psi(2a\omega) & \text{when } |\omega + 2k\pi| \leq 2\pi/a, \\ 0 & \text{when } |\omega + 2k\pi| > 2\pi/a, \end{cases} \tag{104}$$

and

$$D(a\omega) = \frac{\Psi_m(2a\omega)}{\Phi(\omega)}, \tag{105}$$

where $a \geq 2$ or $a = 1$, when $a = 2^j$, $D(a\omega) = O(2^j\omega)$ as shown in Figure 33.

2.5.4 Locating the Best Scale

In the previous section we showed how wavelet coefficients can be calculated at an arbitrary scale. We next discuss a method for determining an appropriate scale based on local feature sizes within an image. Using the image as a matched filter, finite number of scales are searched to find the wavelet coefficients that most resemble the features of interest.

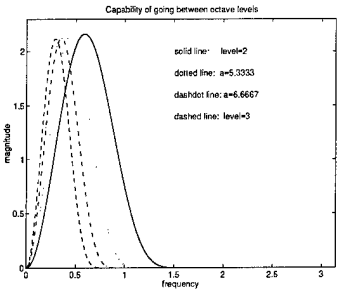

Figure 33: Capability to zoom in between 2 levels.

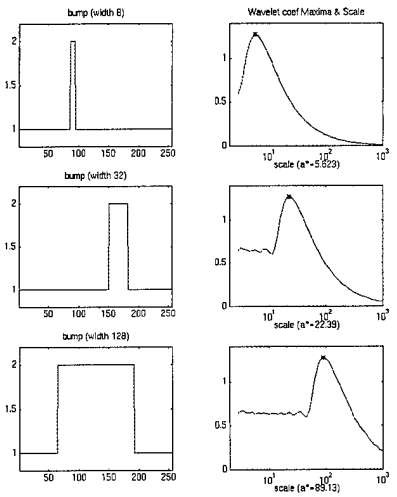

(a)

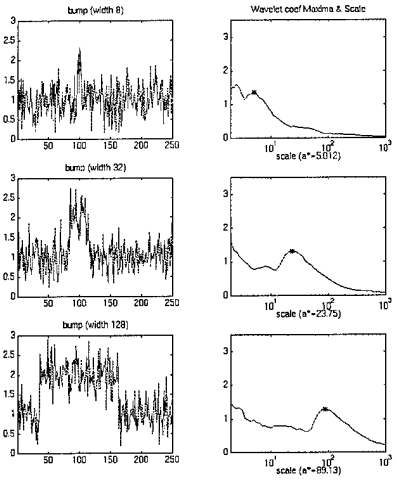

(b)

Figure 34: (a) The best scale to detect a bump in a simulated mass profile. (b) The best scale to detect a bump in a noisy image profile.

This method is demostrated in Figure 34. The left-hand side of Figure 34(a) shows three scales of an image profile, containing bumps of distinct width. We calculated the wavelet transform for each image. At each scale, the maximum of wavelet coefficients across the shifting parameter was found. The relation between scale and the wavelet maximum is shown on the right-hand side of Figure 34(a). Note that there is exactly one scale a^* corresponding to the maximum of wavelet coefficients across both shifting and scale parameters. The value a^* is clearly a function of the size of the feature within the cropped region.

Figure 34(b) shows an image profile corrupted with random noise. Our method is still able to identify candidates for the best scale in the presence of severe noise.

2.5.5 Application of the Segmentation Algorithm

X-ray images of an RMI model 156 phantom (Radiation Measurements Inc., Middleton, WI) were investigated. The RMI phantom contains five masses and six fibrils which mimic two objects of interest in mammography. The radiographic image quality of this phantom, as well as the total number of objects which are deemed to be visible, form a key component of the mammography accreditation program administered by the American College of Radiology (ACR). The RMI phantom is designed so that at least one object in each category is not visible and one object is at the borderline of the visibility threshold [69].

An X-ray image of the RMI phantom is ideal for studying image segmentation since it has well defined features of clinical interest which are present both above and below the threshold for visibility. Figure 35(a) shows a schematic representation of the insert in the RMI. For imaging purposes, this insert is placed in block of acrylic designed to simulate an average compressed breast. Figure 35(b) shows an example of the corresponding radiographic image obtained with a conventional mammography unit as used for ACR accreditation.

We suggest that traditional multiscale analysis carried out at dyadic scales is flawed in the sense of best representation and sensitivity. To demonstrate graphically the flaw of processing at dyadic scales alone we present the following seqence of images, obtained by processing a digital radiograph of the RMI phantom (shown in Figure 35) containing three masses (small, medium, and large). Figure 36(a) shows regions obtained by the zero-crossings of wavelet coefficients extracted from the dyadic scale five. Note that the bounded regions corresponding to the large and medium masses are quite deformed and there are many small "false positives" detected at this level of analysis. However, at the next dyadic scale (level six) shown in Figure 36(b), the boundaries of the small and large

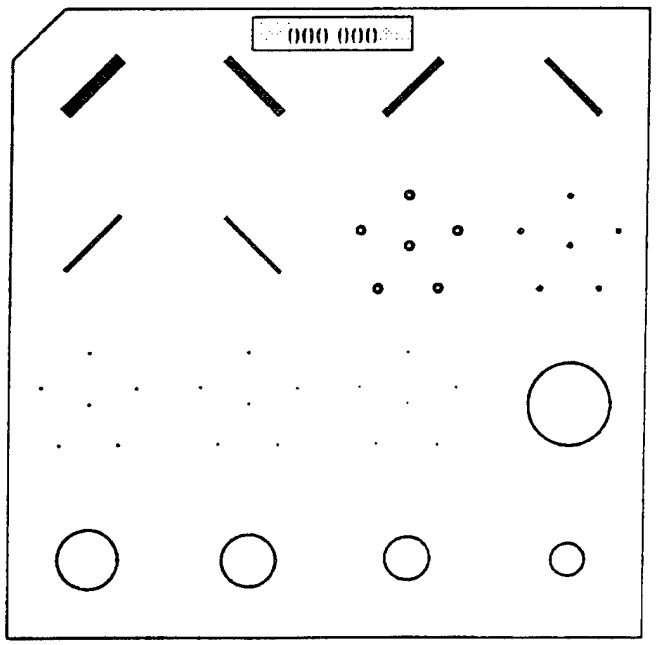

(a)

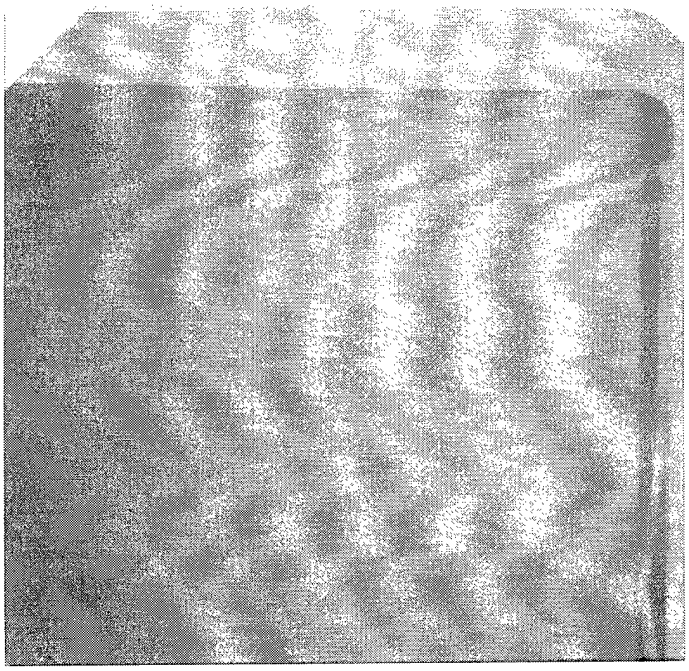

(b)

Figure 35: RMI phantom: (a) internal schematic; (b) digital radiograph.

Visibility on x-ray image	Feature	
	Mass thickness/ diameter	Fibril (nylon fiber diameter)
Easy (E)	750 μm / 6 mm	750 μm
Borderline (B)	500 μm / 5 mm	540 μm
Invisible (I)	250 μm / 3 mm	400 μm

Table 5: Characteristics of masses and fibrils investigated.

masses are merged with an adjacent L-shaped border detected within the phantom.

Thus, a better representation may live (exist) in between the two dyadic scales, level five (which proved to be too fine an analysis) and six (too coarse an analysis). Indeed, this is exactly what we find. Figure 37(a) shows the regions corresponding to zero-crossings extracted at a scale inbetween levels five and six. Note the shape of each of the three masses are distinct and well defined. Figure 37(b), shows the three masses detected by applying simple geometric constraints to each labelled segmented region within the "best" level of analysis. The one false positive present is most likely due to the lack of sophisitication of our present (simple) algorithm.

Figure 35(a) shows that the phantom also contains objects which simulate microcalcifications, however this study focused on fibrils and masses. Table 5 summarizes the key parameters of the masses and fibrils that were investigated. Identification of each object is by category of fibril (F) or mass (M) and by its visibility of easy (E), borderline (B), or invisible (I).

Radiographic images of the RMI phantom were obtained using a Digital Spot Mammography (DSM) system attached to a Lorad Breast Biopsy System (Lorad Corporation, Danbury, CT). The detector area was 50 mm by 50 mm which is smaller than the RMI phantom size shown in Figure 35. As a result, only 20 % was able to be captured in any single digital image. The DSM image matrix size used in this study was 512 by 512 so that the nominal pixel size was 100 μm. Separate images were obtained of mass and fibril regions of the phantom. For the mass region, technique factors of 22 kVp and 16 mAs were used, whereas for the fibril region, 22 kVp and 80 mAs were used. Additional images were also acquired at 32 kVp and 200 mAs, where the increased radiation reduced the noise and permitted the B/I masses and fibrils to become visible. By this process, the locations of the invisible and borderline masses in test images (standard radiation dose) were established with a high level of accuracy.

The acquired image data set was transferred to a SUN workstation (Mountain View, Ca.) for subsequent analysis and display. A 256 by 256 pixel region of interest incorporating the E and B masses was extracted for subsequent processing whereas for the invisible mass, a cropped region of 183 by 183 was used. For the fibrils, the selected region

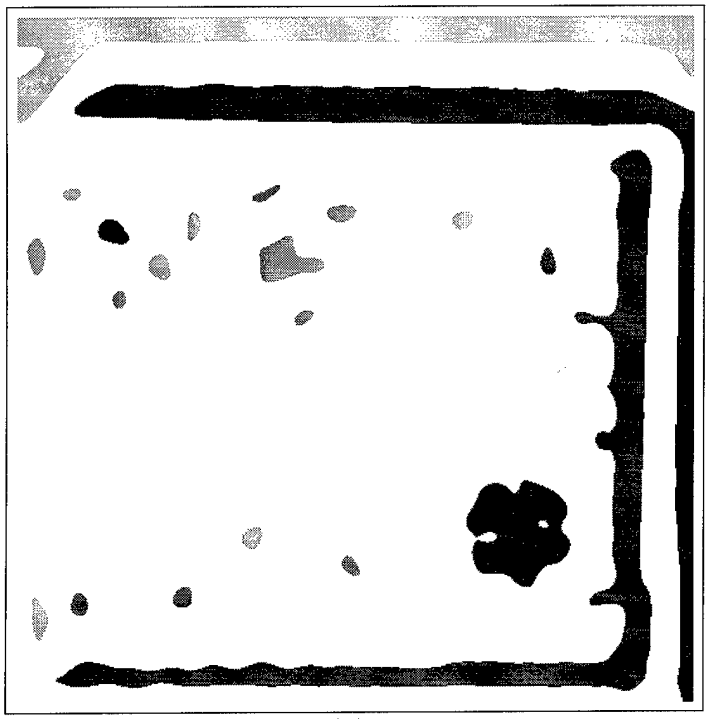

(a)

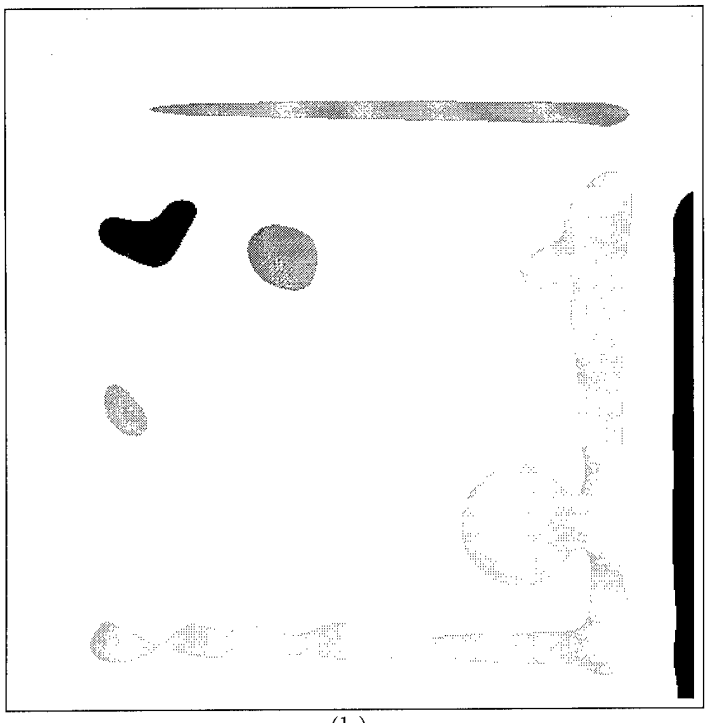

(b)

Figure 36: (a) Blobs detected from dyadic wavelet coefficients at level 5, (b) Blobs detected from dyadic wavelet coefficients at level 6.

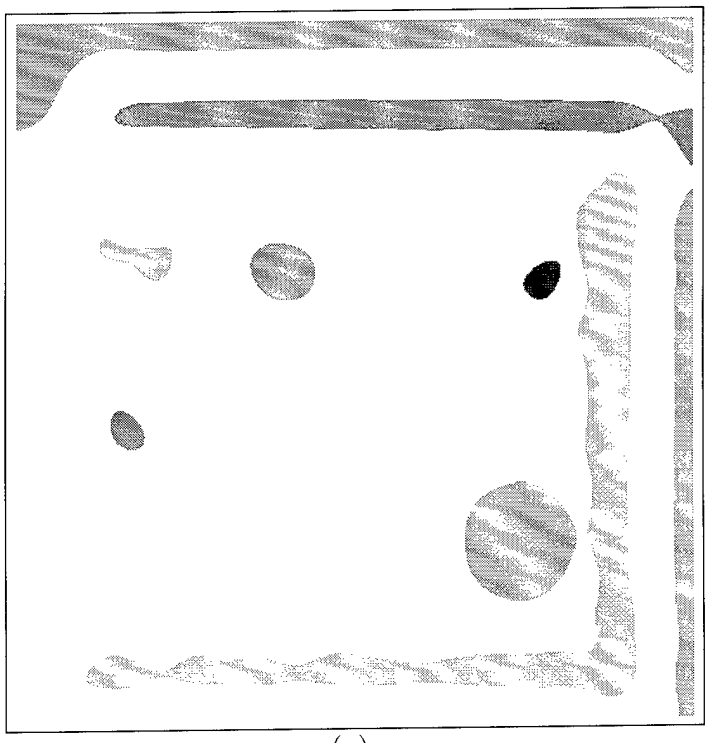

(a)

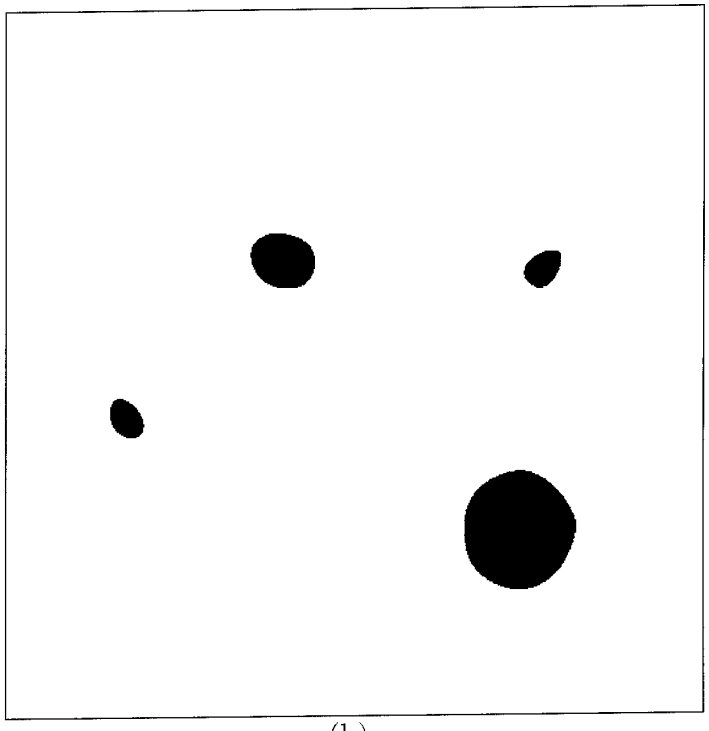

(b)

Figure 37: (a) Suspicious regions detected for wavelet coefficients at scale 28.5. (b) Suspicious region identified as possible masses providing local support for enhancement of wavelet coefficients.

was 128 by 128 pixels. The choice of these regions was determined by the need to eliminate all extraneous objects for this part of the image processing exercise. For comparison purposes, a uniform background of 200 by 200 pixels containing no objects was also investigated, and categorized as none (N) below.

Segmentation - Mass

Figure 38 shows representative images of the cropped regions corresponding to three masses (E, B and I) as well as a background region with no objects (N). These images were generated using 22 kVp and 16 mAs. Also shown are the same four images after histogram equalization and unsharp masking enhancement. As expected, the processed images in Figure 35 shows negligible improvement in overall mass visibility using either of these two common image enhancement techniques.

Figure 39 shows the segmentation results obtained for an easily visible mass, M-E. A profile through the center of M-E is depicted in Figure 39(a), and the corresponding profile of the wavelet coefficients is shown in Figure 40(b). It is the interscale value, $a = 48$, which best defines the wavelet coefficient profile and therefore best segments the mass (see Figure 39(d)).

Figure 41 shows the segmentation results obtained for a mass with borderline visibility, $M - B$. A profile through the center of $M - B$ is depicted in Figure 42(a), and the corresponding profile of the wavelet coefficient is shown in Figure 42(b). Note that the interscale value $a = 28$ best defines the wavelet coefficient profile and therefore best segments the mass (see Figure 41(e)). The segmentation algorithm clearly defined this mass.

Figure 43 shows the segmentation results obtain for the invisible mass, $M - I$. A profile through the center of $M - I$ is depicted in Figure 44(a), and the corresponding profile of the wavelet coefficients is shown in Figure 44(b). Here the interscale value $a = 28$ again best defines the wavelet coefficient profile and therefore best segments the mass (see Figure 43(e)). It is clear that the segmentation algorithm developed in this work was capable of finding the mass which is normally invisible on standard radiographs of this phantom.

Figure 45 shows the results obtained when processing the background region with no object in the field of view.

Segmentation - Fibrils

Figure 47 shows representative images of the cropped regions corresponding to three fibrils (E, B, and I). As in the case of masses, these images were generated using 34 kVp (22 is preferred) and 56 mAs (16 mAs is preferred). Also shown are these same images

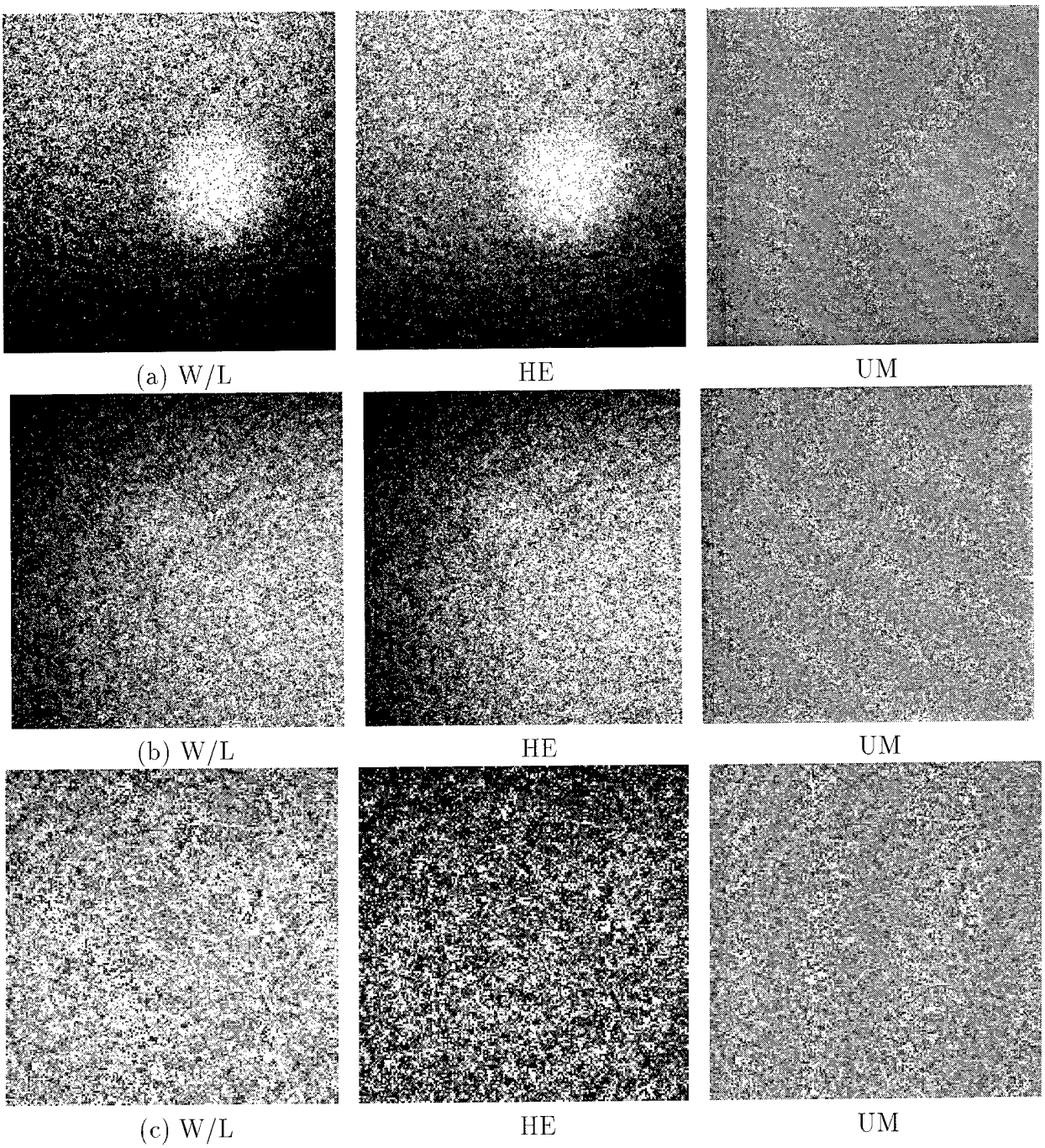

Figure 38: Different processing methods, window and leveling (W/L), histogram equalization (HE), unsharp masking (UM). (a) The easy case, (b) The borderline case, (c) The invisible case.

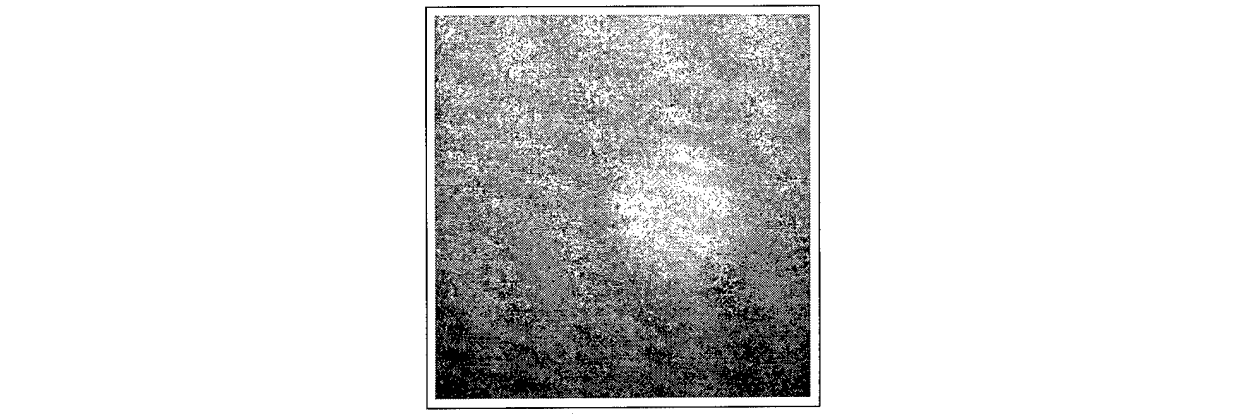

(a) original

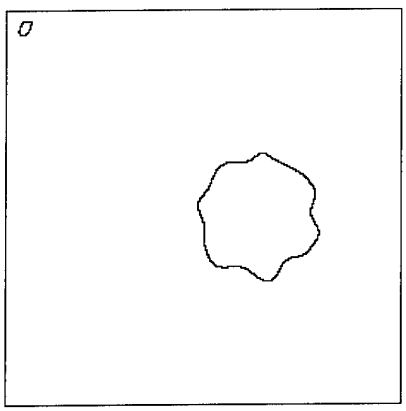

(b) L=5 (a=16)

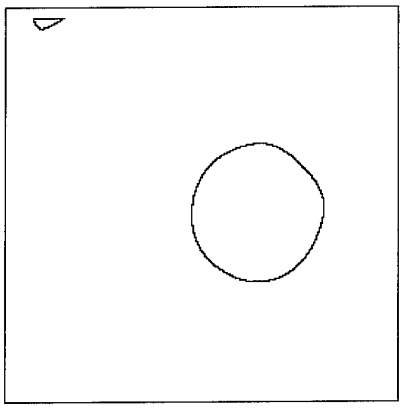

(c) L=6 (a=32)

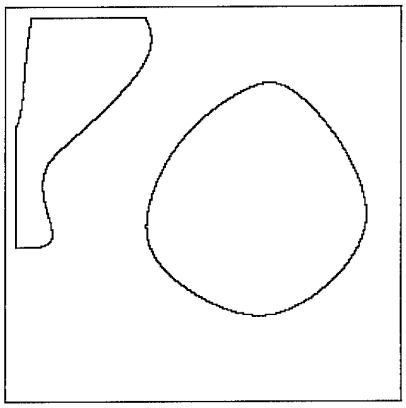

(d) L=7 (a=64)

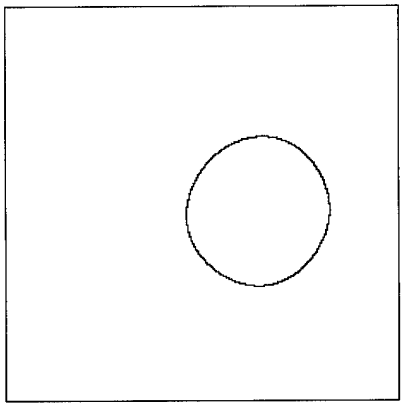

(e) a=48

Figure 39: Mass (large) and its edges: (a) original image; (b)–(d) dyadic scales; (e) edges at best scale.

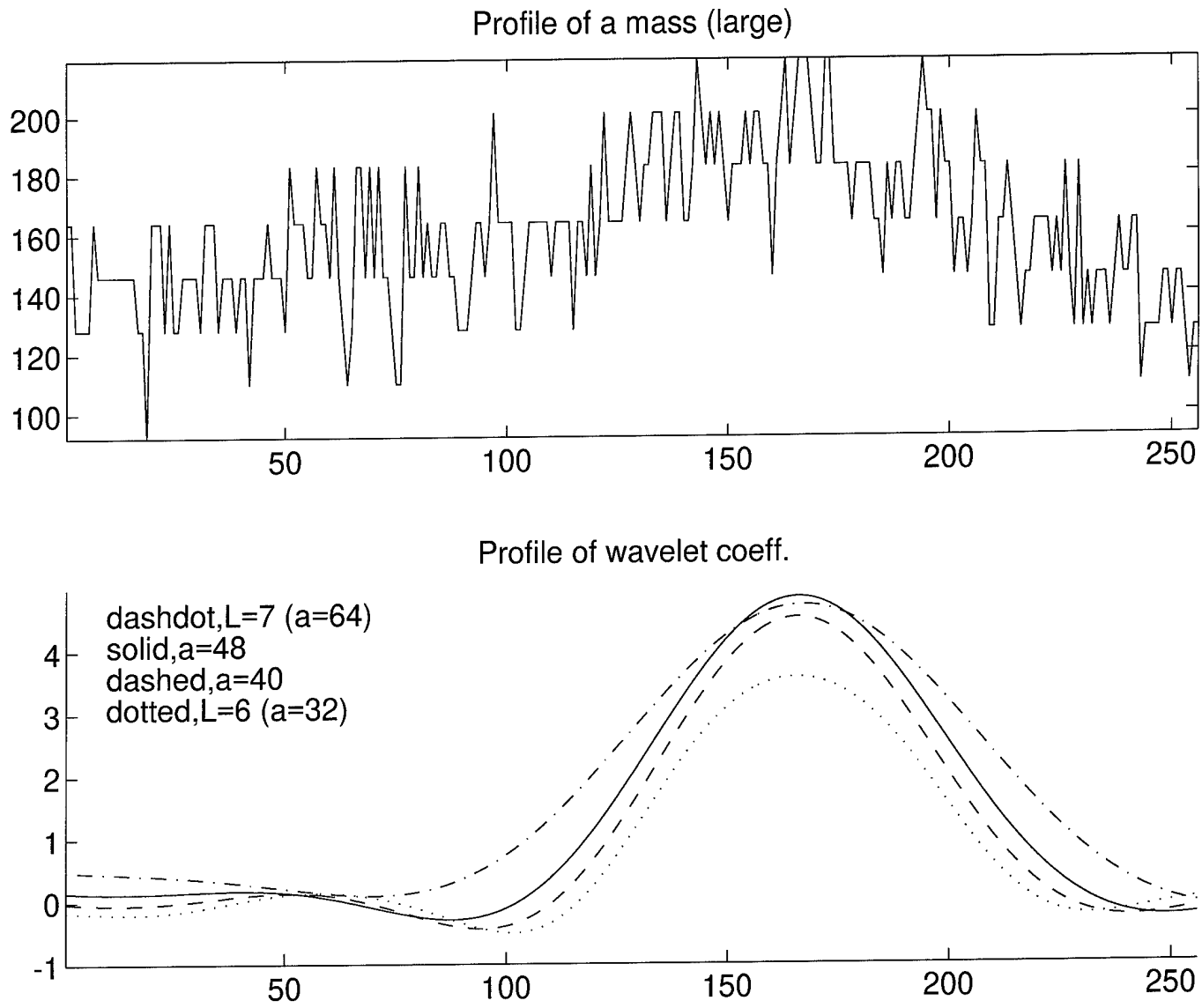

Figure 40: Profiles of the large mass and its wavelet coefficients.

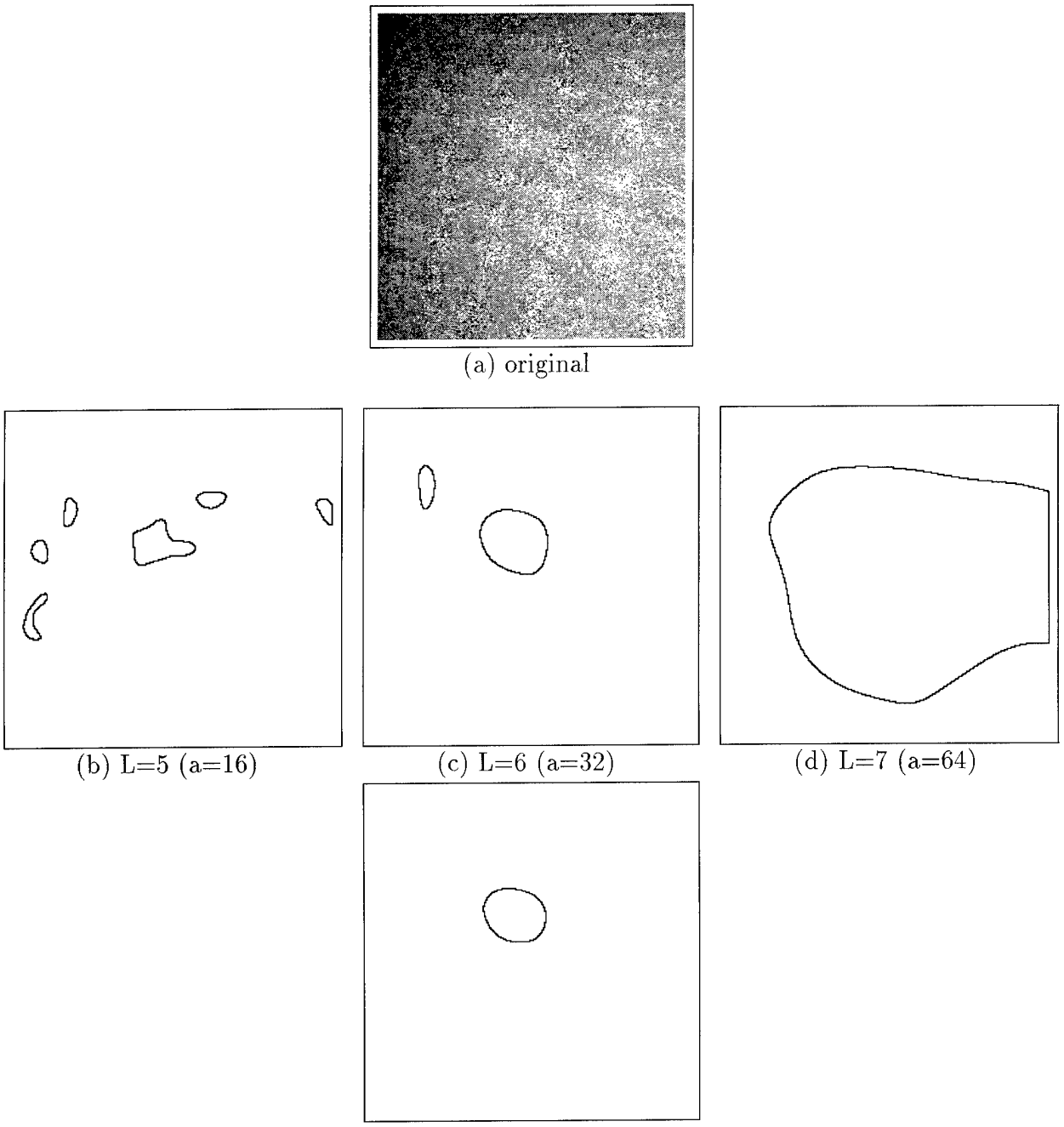

(a) original

(b) L=5 (a=16)

(c) L=6 (a=32)

(d) L=7 (a=64)

(e) a=28

Figure 41: Mass (medium) and its edges: (a) original image; (b)–(d) dyadic scales; (e) edges at best scale.

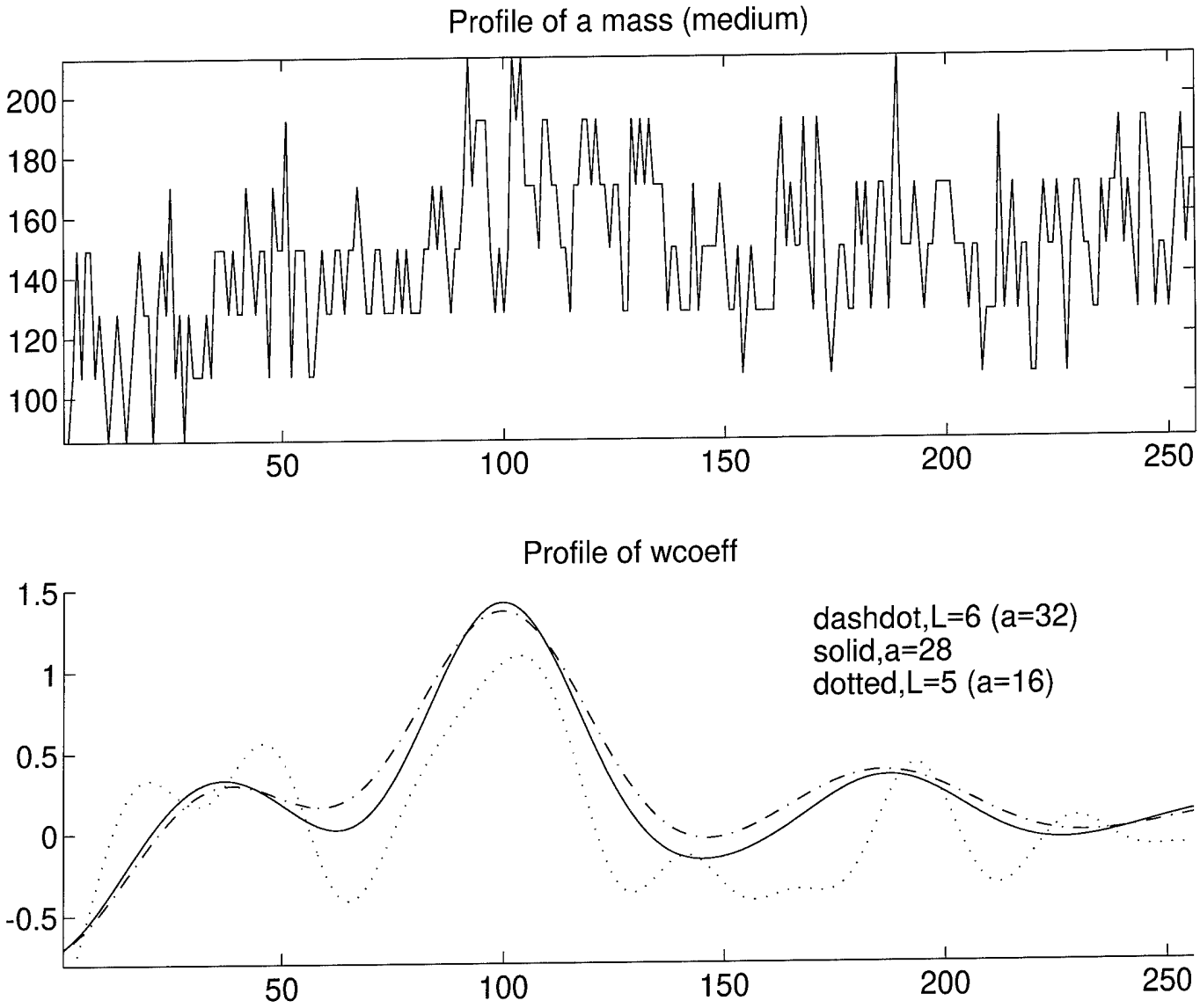

Figure 42: Profiles of the medium mass and its wavelet coefficients.

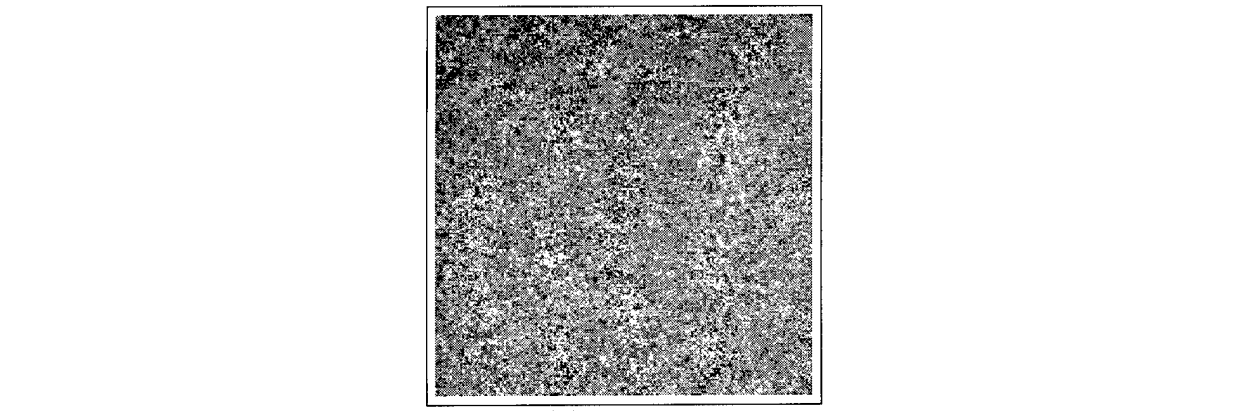

(a) original

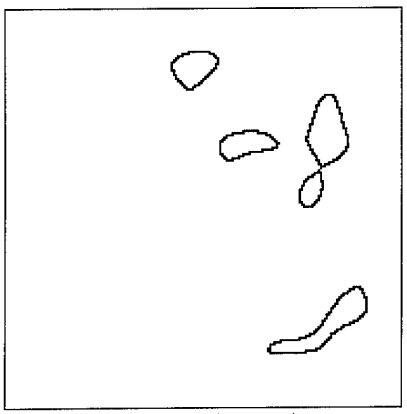

(b) L=5 (a=16)

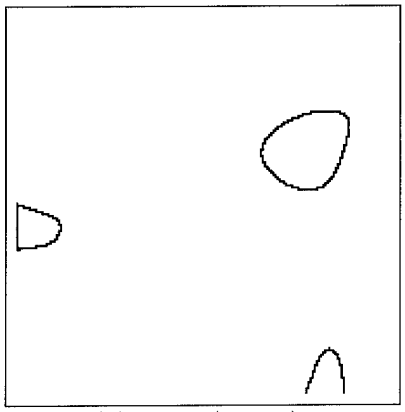

(c) L=6 (a=32)

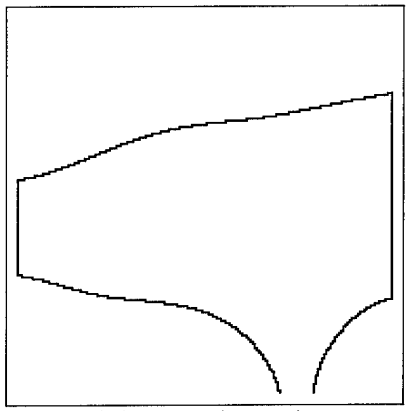

(d) L=7 (a=64)

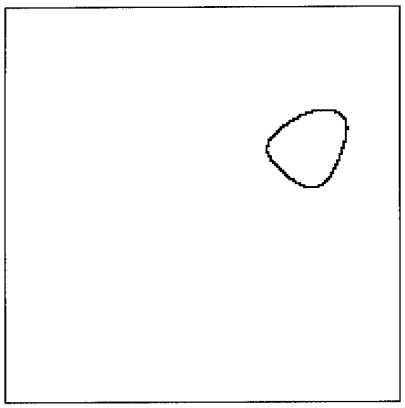

(e) a=28

Figure 43: Mass (small) and its edges: (a) original image; (b)–(d) dyadic scales; (e) edges at best scale.

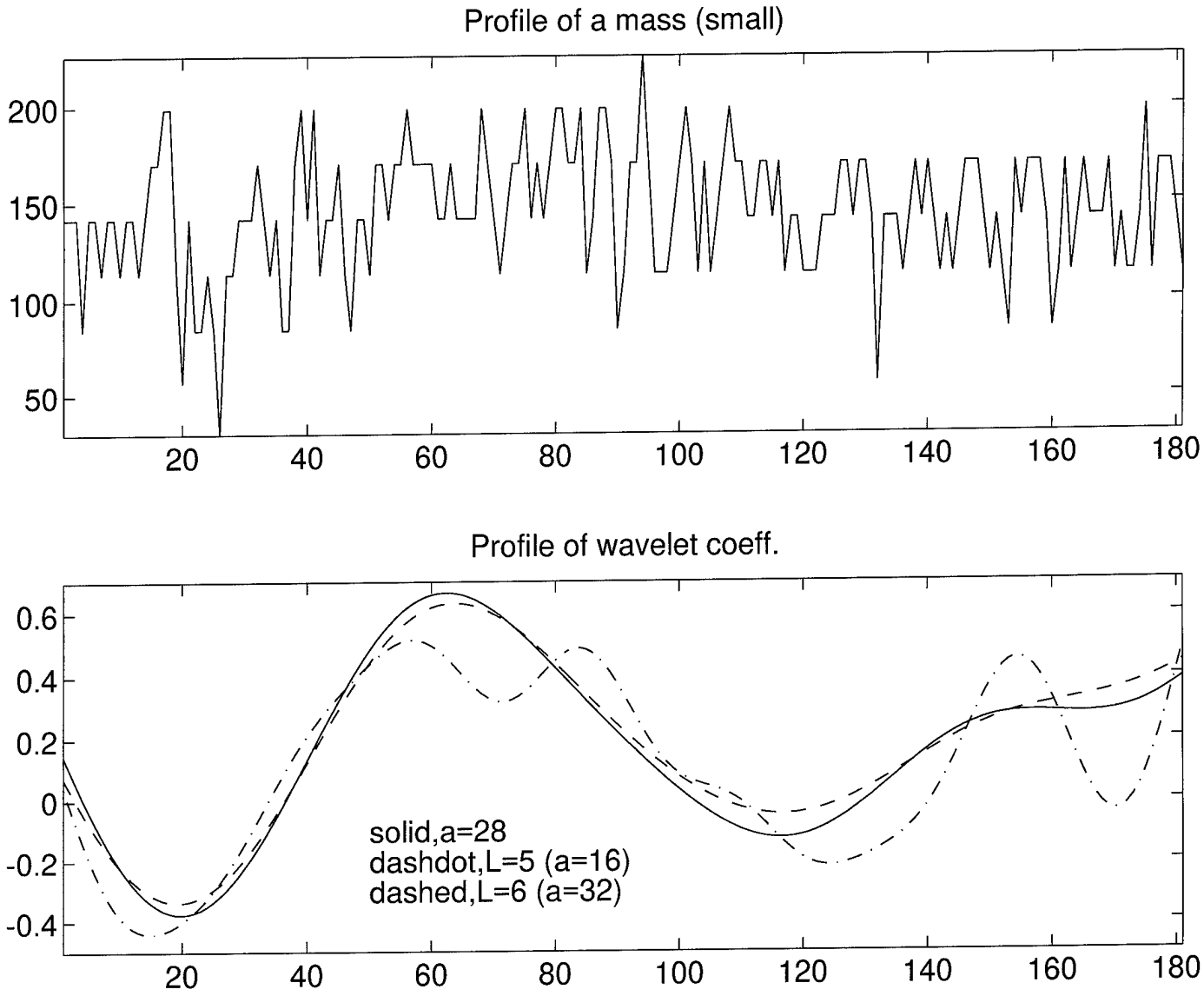

Figure 44: Profiles of the small mass and its wavelet coefficients.

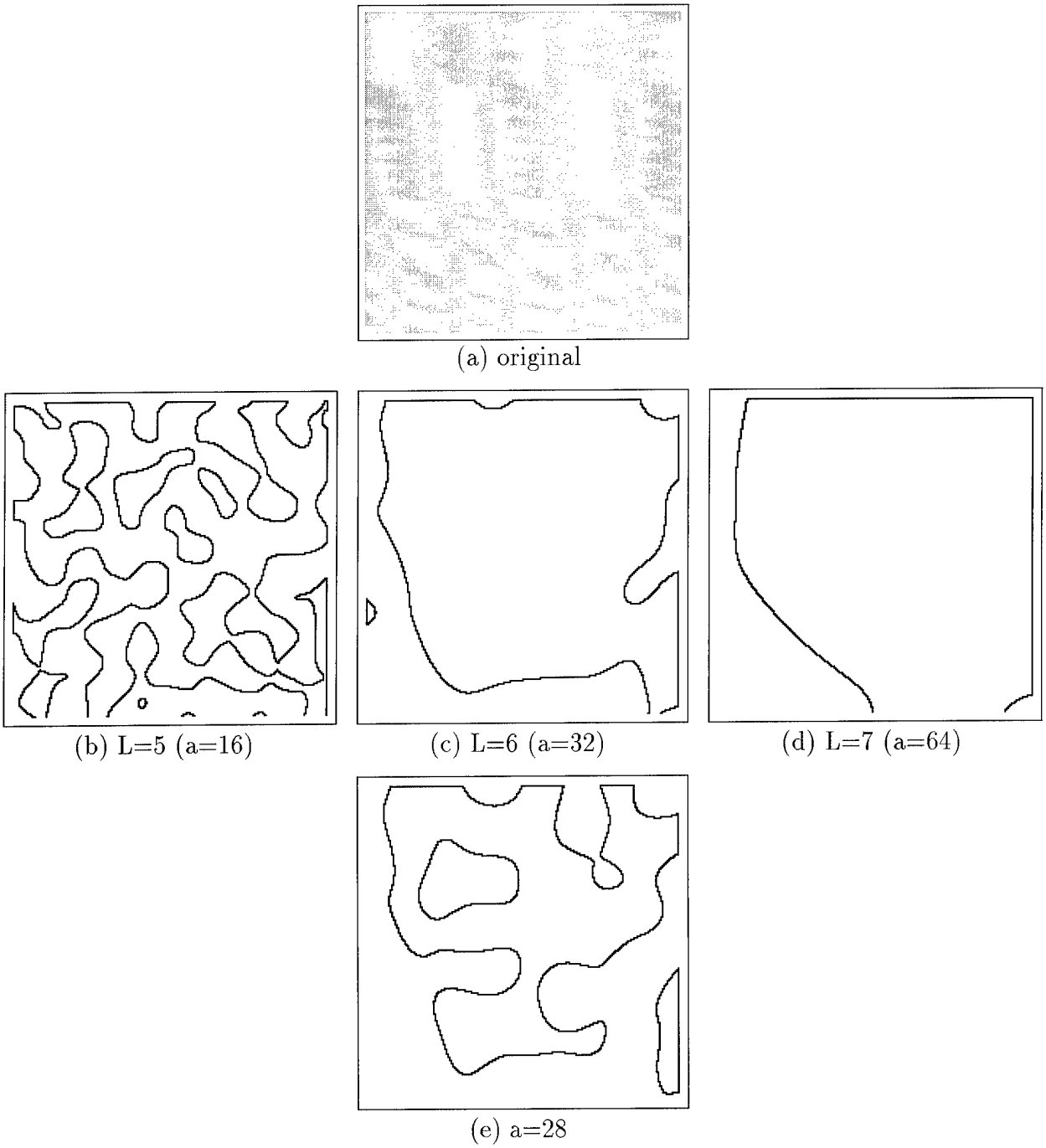

(a) original

(b) L=5 (a=16)

(c) L=6 (a=32)

(d) L=7 (a=64)

(e) a=28

Figure 45: Randomly chosen region and its edges: (a) original image; (b)–(d) dyadic scales; (e) edges detected at best scale.

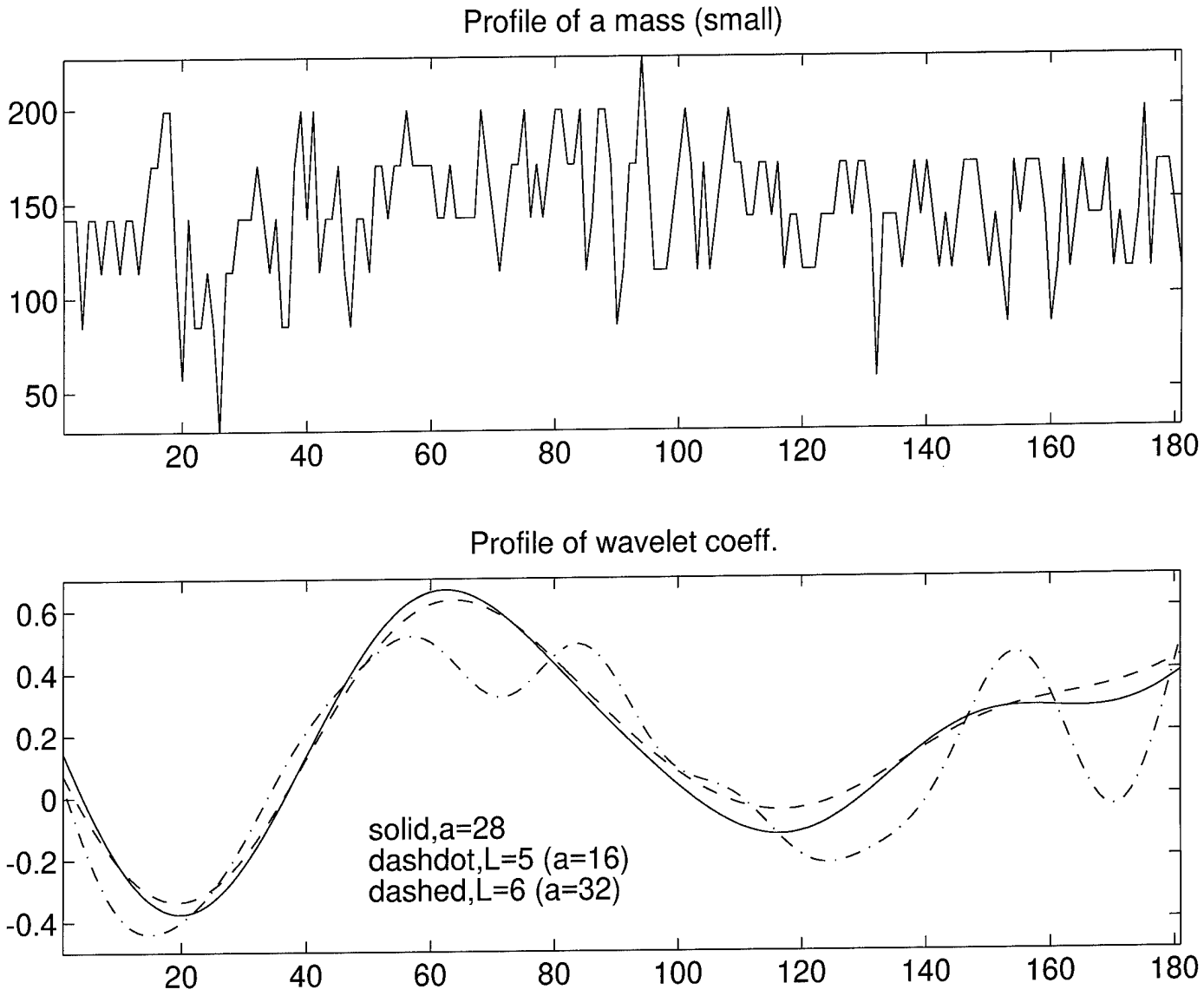

Figure 46: Profiles of the small mass and its wavelet coefficients.

using histogram equalization as well as an unsharp masking enhancement. The processed images in Figure 47 show that little improvement in overall fibril visibility is achieved using either of these three standard image enhancement techniques.

Figure 48 shows the segmentation results obtained for an easily visible fibril, F-E. A profile through the center of F-E is depicted in Figure 49(a), and the corresponding profile of wavelet coefficients is shown in Figure 49(b). It is the interscale value $a = 7.5$ which best defines the wavelet coefficient profile and therefore best segments the shape of the fibril (see Figure 48(a)).

Figure 50 shows the segmentation results obtained for fibril with borderline visibility, F-B. A profile through the center of F-B is depicted in Figure 51(a), and the corresponding profile of the wavelet coefficients is shown in Figure 51(b). The interscale value $a = 10$ best defined the wavelet coefficient profile and therefore best captured the fibril (see Figure 50(e)). The segmentation algorithm clearly defined this fibril.

Figure 52 shows the segmentation results obtained for a fibril that is invisible, F-I. A profile through the center of F-I is depicted in Figure 53(a), and the corresponding profile of the wavelet coefficients is shown in Figure 53(b). It is an interscale value which best defines the wavelet coefficient profile and therefore best captures the fibril (see Figure 52(a)). The segmentation algorithm clearly defined this subtle fibril.

2.5.6 Summary

We have shown that regions corresponding to masses can be identified reliably through frame representations of a continuous multiscale analysis. We showed that subtle features characteristic of mammographic findings required a finer parameterization of scale space than provided by traditional methods of wavelet analysis.

Basis functions for carrying out continuous multiscale analysis were designed to be symmetric and have zero-phase providing closed contours (via zero-crossings) of emergent features within each level of scale.

Spatial locality was preserved via a frame representation enabling segmentation of masses and adaptive contrast enhancement. We suggest that masses located in dense and somewhat dense mammograms can be reliably characterized and identified by applying geometric constraints (size and shape) to the set of segmented regions.

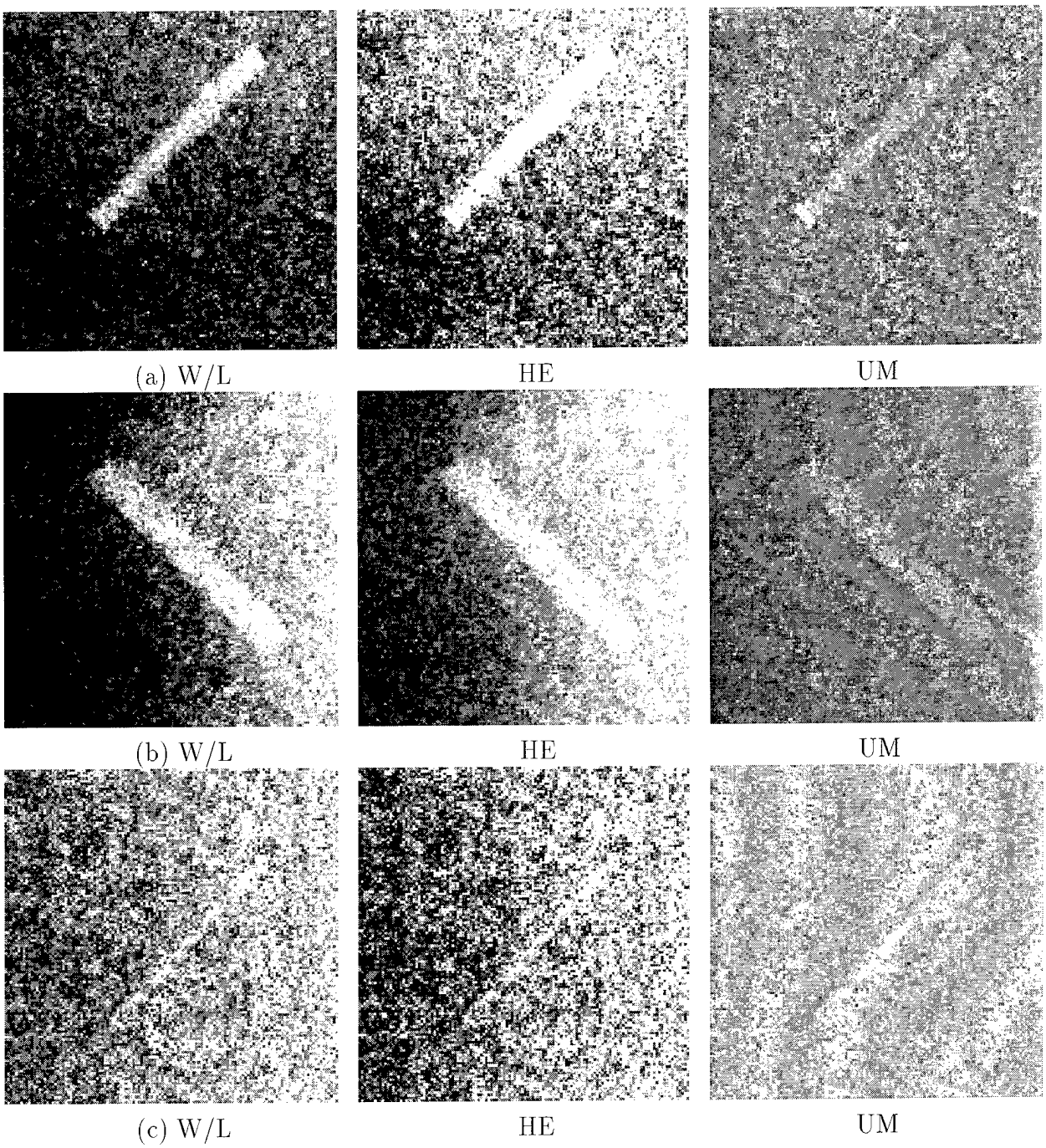

Figure 47: Different processing methods, window and leveling (W/L), Histogram equalization (HE), unsharp masking (UM). (a) The easy case, (b) The borderline case, (c) The invisible case.

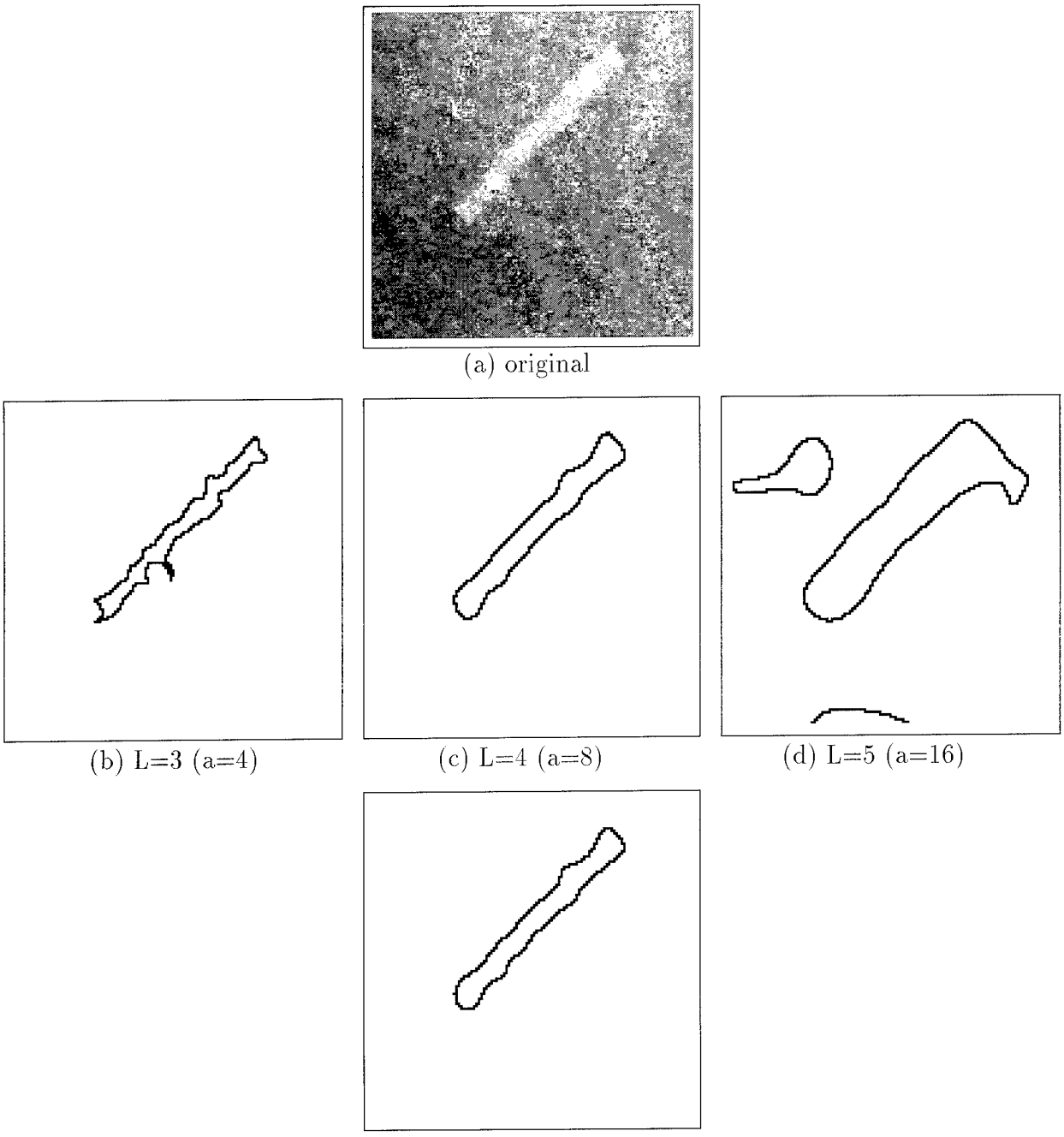

(a) original

(b) L=3 (a=4)

(c) L=4 (a=8)

(d) L=5 (a=16)

(e) a=7.5

Figure 48: Fibril (E-easy) and its edges: (a) original image; (b)–(d) dyadic scales; (e) edges at best scale.

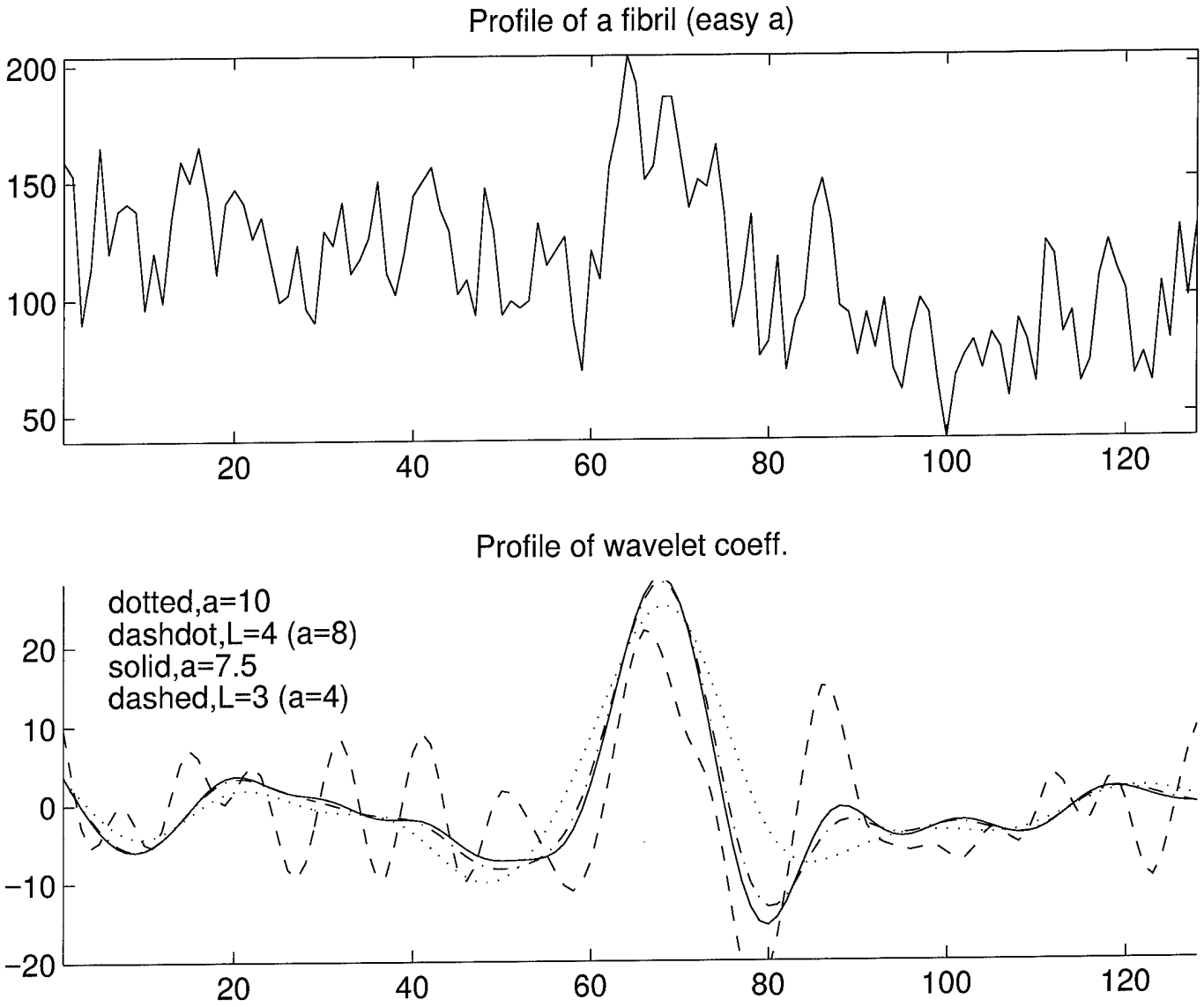

Figure 49: Profiles of the fibril and its wavelet coefficients.

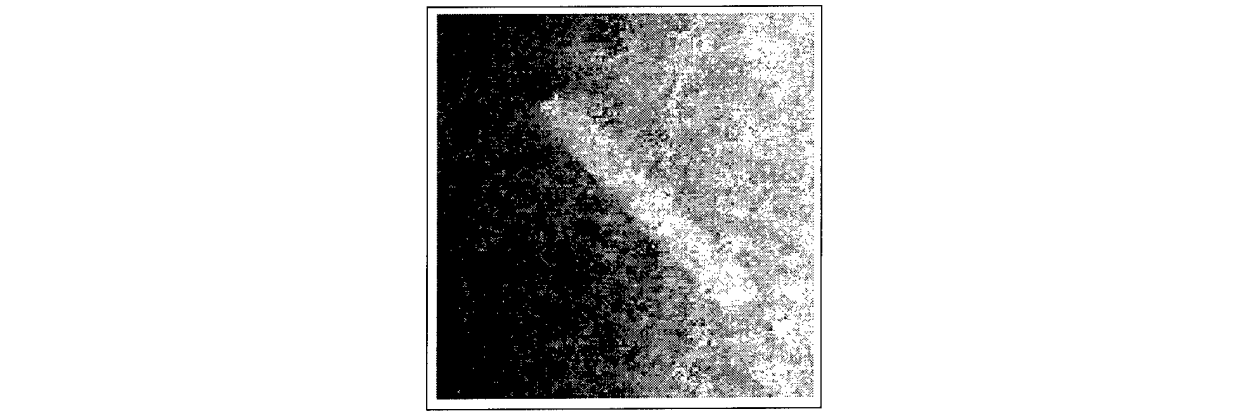

(a) original

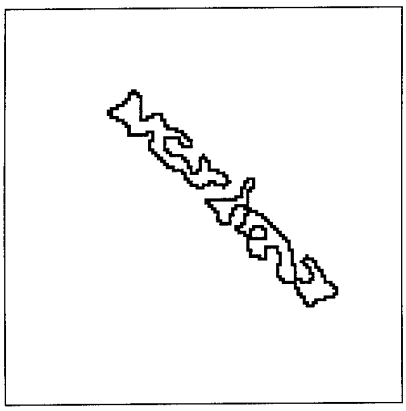

(b) L=3 (a=4)

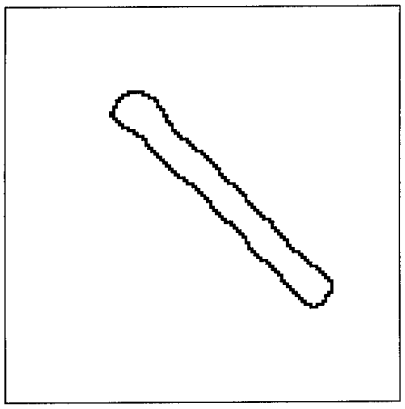

(c) L=4 (a=8)

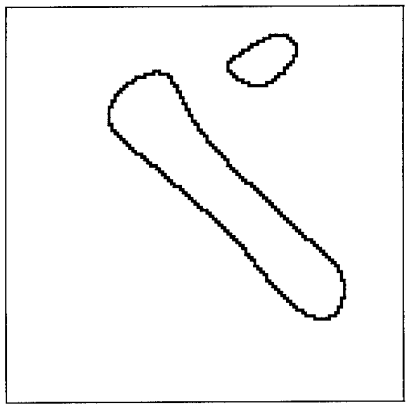

(d) L=5 (a=16)

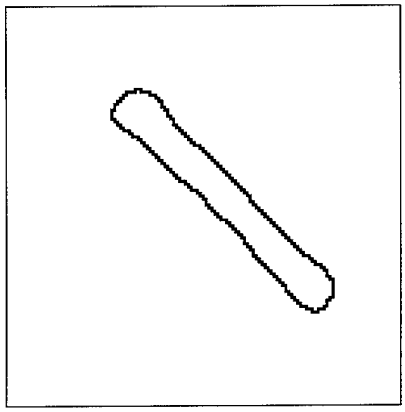

(e) a=10

Figure 50: Fibril (B-borderline) and its edges: (a) original image; (b)–(d) dyadic scales; (e) edges at best scale.

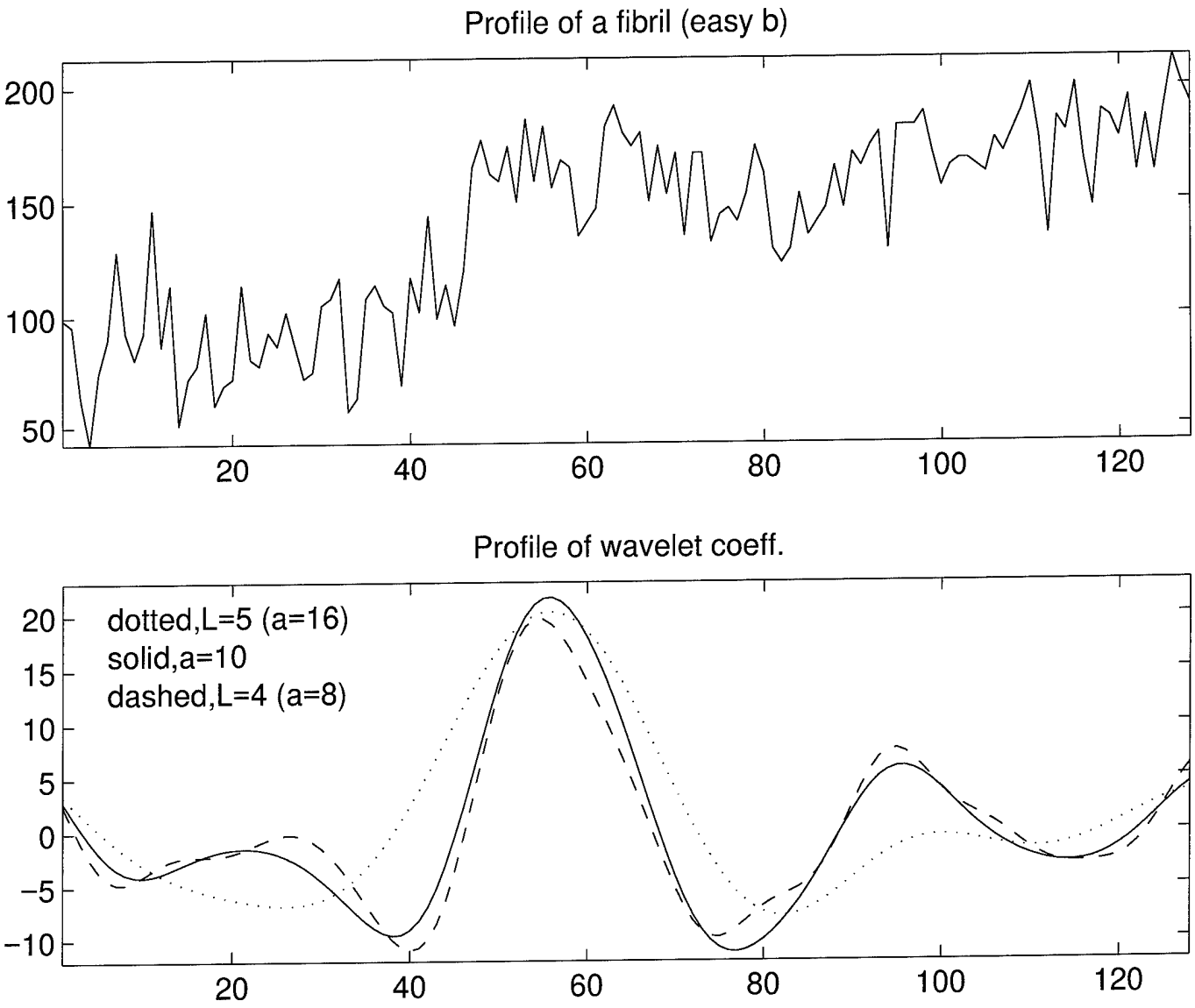

Figure 51: Profiles of the fibril and its wavelet coefficients.

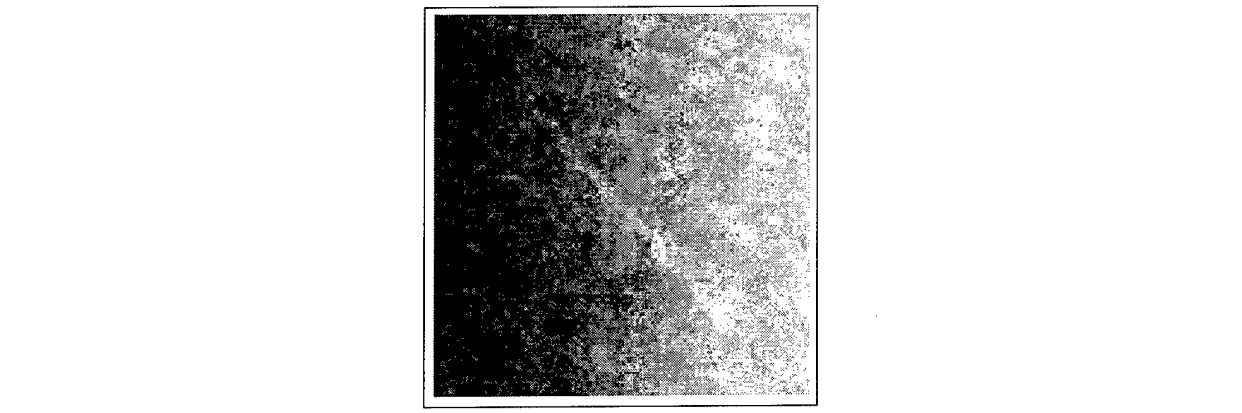

(a) original

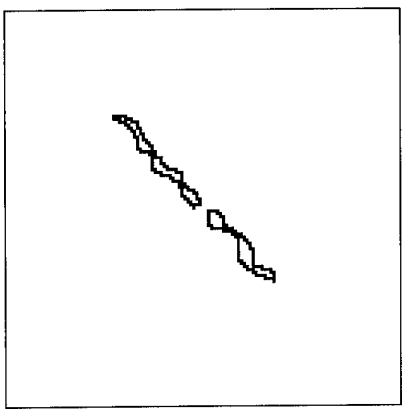

(b) L=3 (a=4)

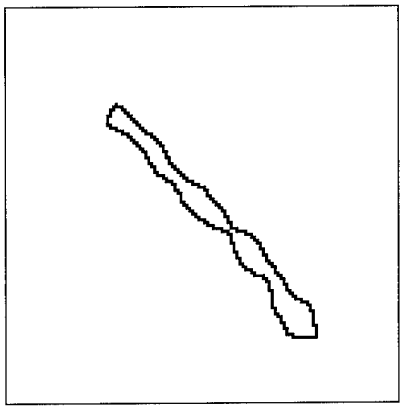

(c) L=4 (a=8)

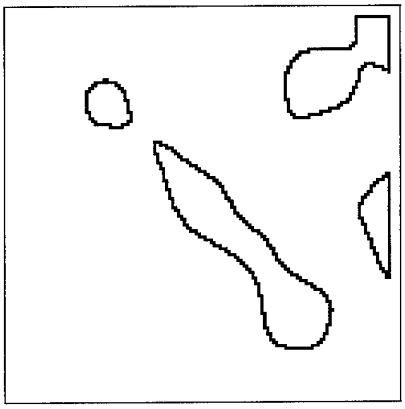

(d) L=5 (a=16)

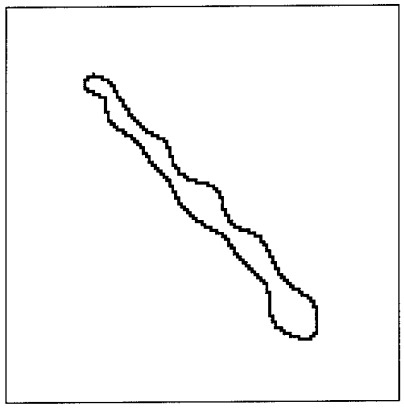

(e) a=10

Figure 52: Fibril (I-invisible) and its edges: (a) original image; (b)–(d) dyadic scales; (e) edges at best scale.

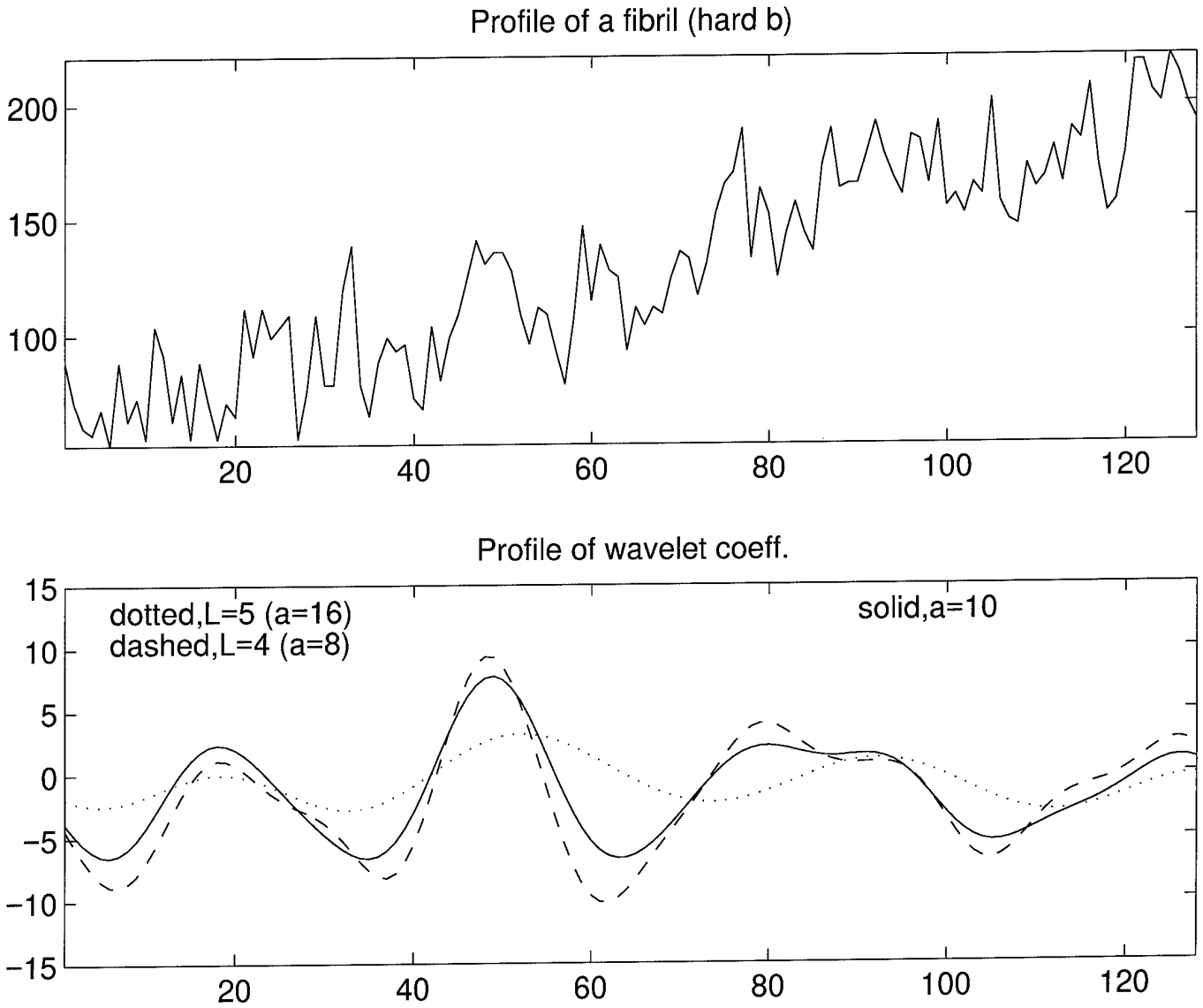

Figure 53: Profiles of the fibril and its wavelet coefficients.

2.6 Enhancement of Computer Simulated Masses for Mammography Using Wavelet Analysis

2.6.1 Introduction

In this section we report results on the application of enhancement by hard thresholding. We present:

- mathematical details of modeling of image formation,
- details of hard thresholding method, and
- methods (mathematical and psychophysical) for evaluation of the enhancement technique.

In section 2.6.3 we present the enhancement evaluation methods. In section 2.6.4 we demonstrate results of our experimentation with the hard thresholding technique and in section 2.6.5 we present conclusions and future directions.

2.6.2 Methodology

Phantoms Simulated by Mathematical Construction

The phantom used in this study was designed to replicate circularly shaped masses in a uniform noisy background.

1. Image: For computational purposes, a 512 by 512 matrix containing a number of simulated masses was used. There were 8 bits per pixel corresponding to 256 grey levels. The phantom was divided into 25 squares (a 5 by 5 grid). The size of each square was 100 by 100 pixels. Thirteen of these squares were chosen randomly to contain a simulated mass while the remaining twelve contained only noise.

2. The masses: Each mass was modelled as a circle with a radius equal to r. The center of the mass coincided with the center of the square. The signal intensity of the mass was computed by:

$$I(x,y) = \alpha\sqrt{(r^2 - x^2 - y^2)} \tag{106}$$

where x and y were the coordinates with respect to a local coordinate system (point of origin for the local coordinate system was the geometrical center of the mass). The parameter α controls the local contrast and r controls the size of the simulated mass (r is the radius of the mass). The background had a grey level of value 128.

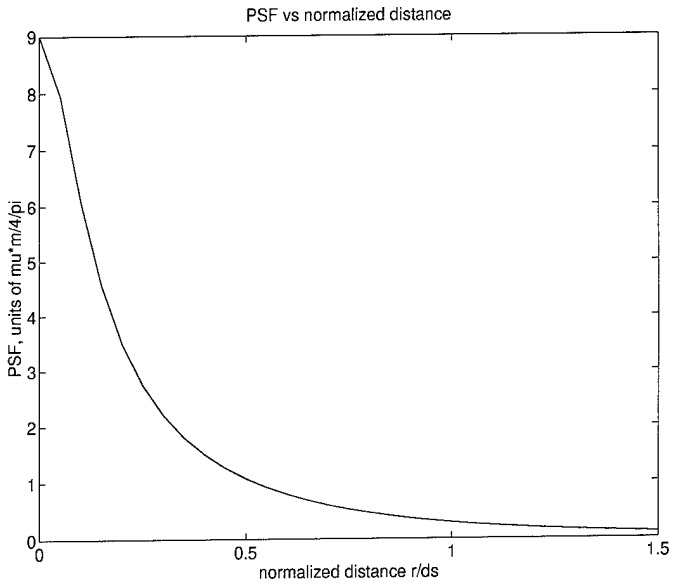

Figure 54: A plot of the Point Spread Function (PSF) as a function of the normalized distance d/r_s.

3. Noise and blurring: In mammography, the dominant source of image noise is quantum mottle and for this simulation, a $10mR$ exposure level at the detector was used with an average photon energy of 20 keV. A 42 μm pixel size was used since this corresponds to a $4k \times 6k$ matrix size for a conventional 25 $cm \times 30$ cm mammogram [70]. As a result the mean number of photons per pixel should be a 1000 which corresponds to a standard deviation in the noise level of 3% [71]). The limiting resolution in screen-film mammography is in the range 15 to 20 line pairs per mm [72]. The computer simulated phantom was convolved with a smoothing function to simulate a reduced modulation transfer function. A screen thickness of 80 μm was assumed and a two dimensional Point Spread Function (PSF) generated using an expression derived by Barrett and Swindell [73]. A plot of the Point Spread Function used in our simulations as a function of the normalized distance r/d_s, is presented in Figure 54.

Figure 55 (a) shows one of twenty-five squares that was cropped from a simulated phantom. The size of the square is 100 by 100 pixels. This square contains, located at its center, a mass of radius of 20 pixels and it is corrupted with zero mean Gaussian noise of standard deviation of 15. Figures 55 (b) and 55 (c) show two phantoms of the same size with only a mass and only noise. Figures 56 (a), 56 (b) and 56 (c) show three profiles chosen from the Figure 55 (a). Finally, Figure 57 shows a typical simulated phantom containing thirteen masses.

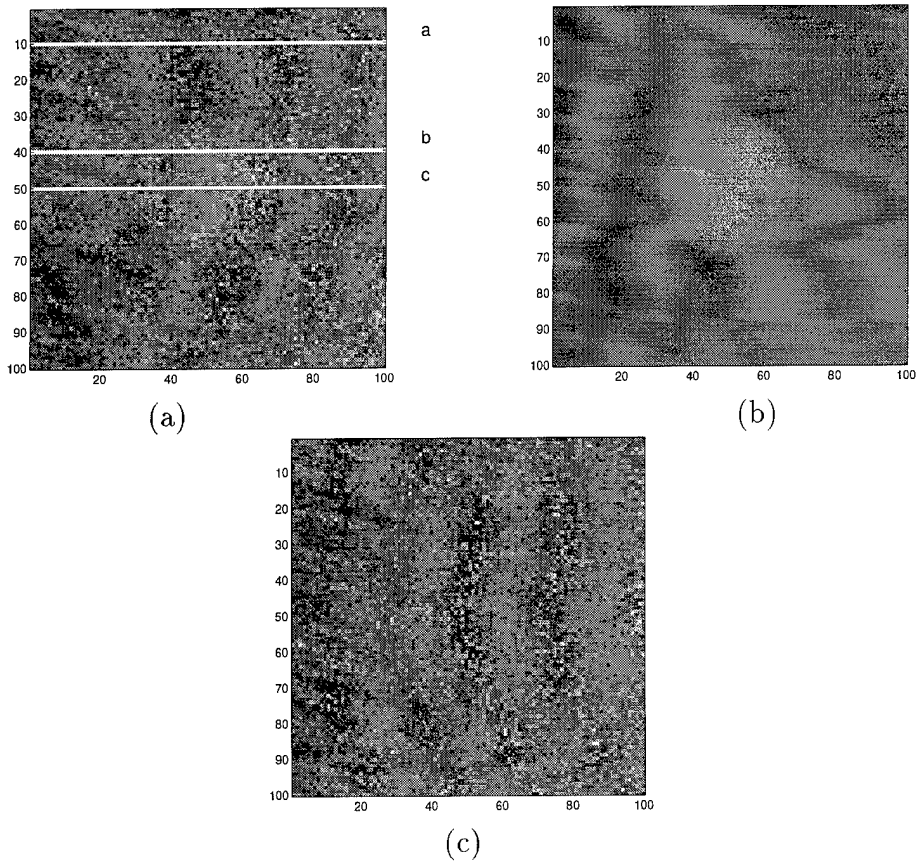

Figure 55: (a) A square containing a mass at its center and corrupted with Gaussian noise; (b) the same square containing only signal; (c) the same square containing only noise.

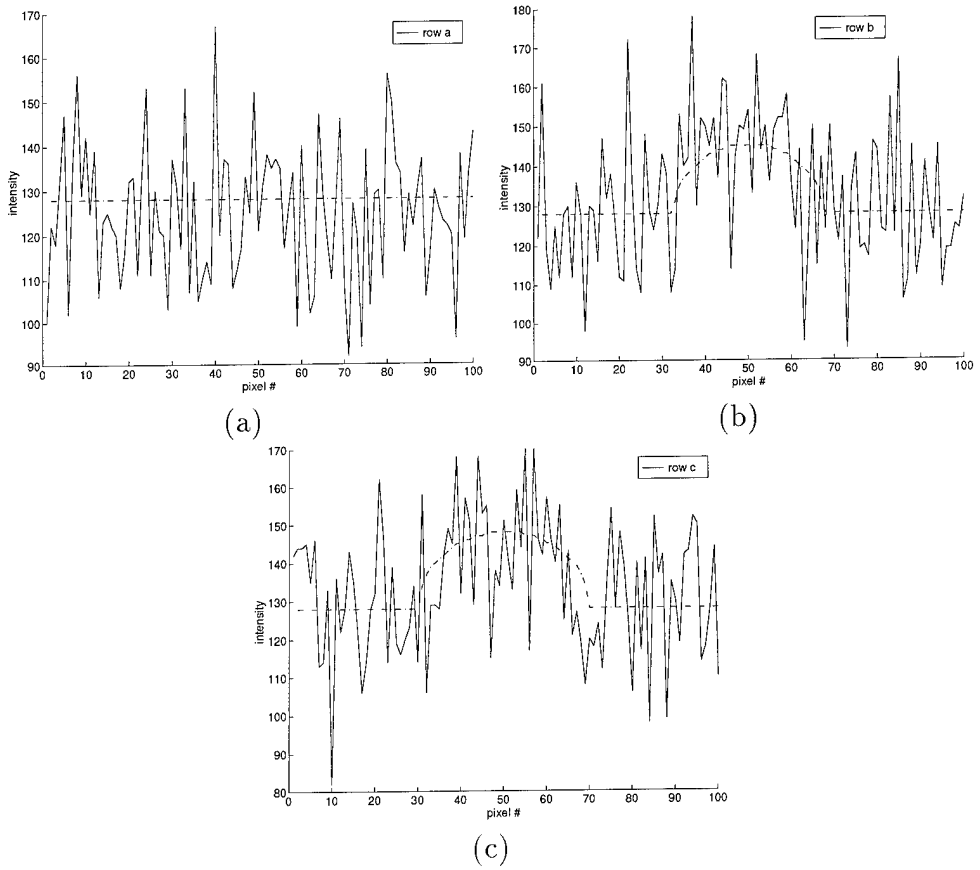

Figure 56: Three profiles of the square shown in Figure 55. For strips indicated as scanlines (a), (b) and (c) respectively.

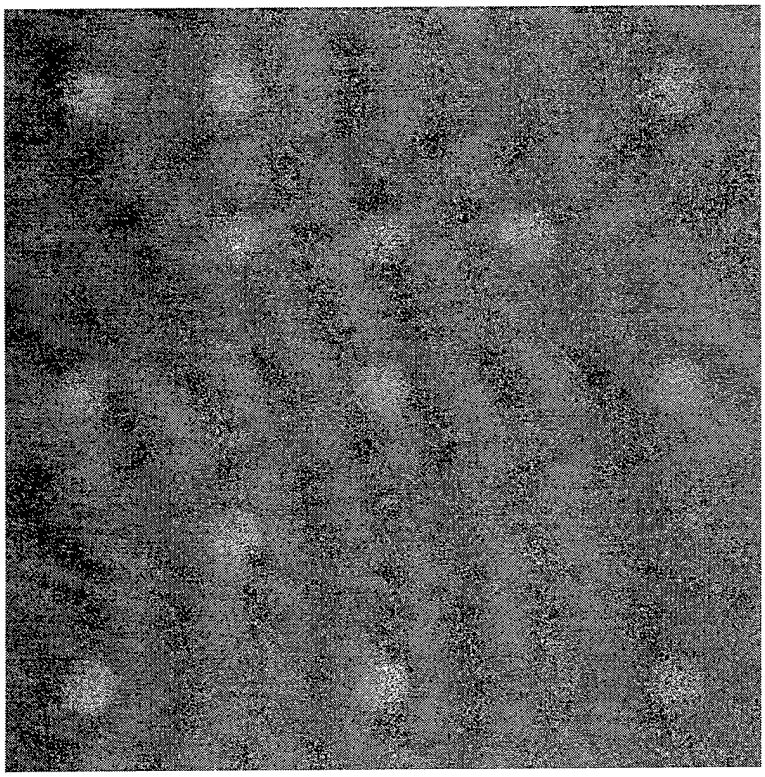

Figure 57: A typical mathematical phantom used in our study. The size of the phantom was 512 by 512 pixels. The phantom contained 13 masses and was corrupted with random Gaussian noise.

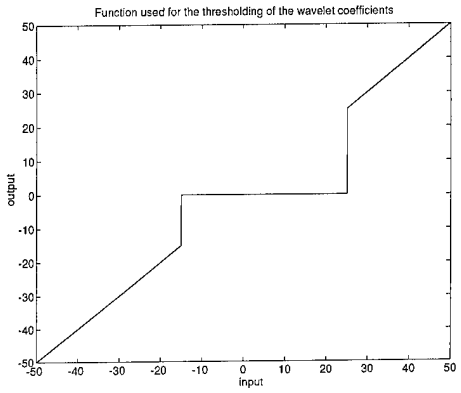

Figure 58: A plot of the piecewise linear function of the wavelet output $f(w)$ as a function of the input w of the wavelet coefficients.

Image Enhancement

Thresholding of the wavelet coefficients for the purpose of denoising is a popular theme in current literature. In this work we investigated the use of hard thresholding for the denoising of the simulated phantoms. In this method for each decomposition level i a threshold value t_i was selected and all the coefficients below that level were set to zero. The rest remained unaltered. Mathematically this can be expressed as follows:

$$y_{l,i} = \begin{cases} 0 & \text{for } t_i^n < w_{l,i} < t_i^p, \\ w_{l,i} & \text{otherwise,} \end{cases} \tag{107}$$

where $w_{l,i}$ is the l–th wavelet coefficient of the i–th level t_i^n and t_i^p are the positive and negative thresholds respectively for decomposition level i. Figure 58 shows schematically the thresholding strategy. The choice of the thresholds t_i^n and t_i^p was based on the percentage of the wavelet coefficients that remain unaltered after the thresholding. In other words if we set the threshold at 20 %, t_i^n and t_i^p were chosen in such a way as to leave 80 % of the negative wavelet coefficients and 80 % percent of the positive wavelet coefficients unaltered. The equality:

$$t_i^p = -t_i^n \tag{108}$$

does not necessarily hold since the histogram of the coefficients for all levels is not symmetric with respect to the $y = 0$ axis. Figures 59(a)–(f) show the histograms of wavelet coefficients of the six decomposition levels for the phantom of Figure 57. The vertical lines denote the thresholds for the percentages 0 %, 10 %, ..., 100 %.

After performing the inverse transform the resulting image was window leveled for better visualization and contrast.

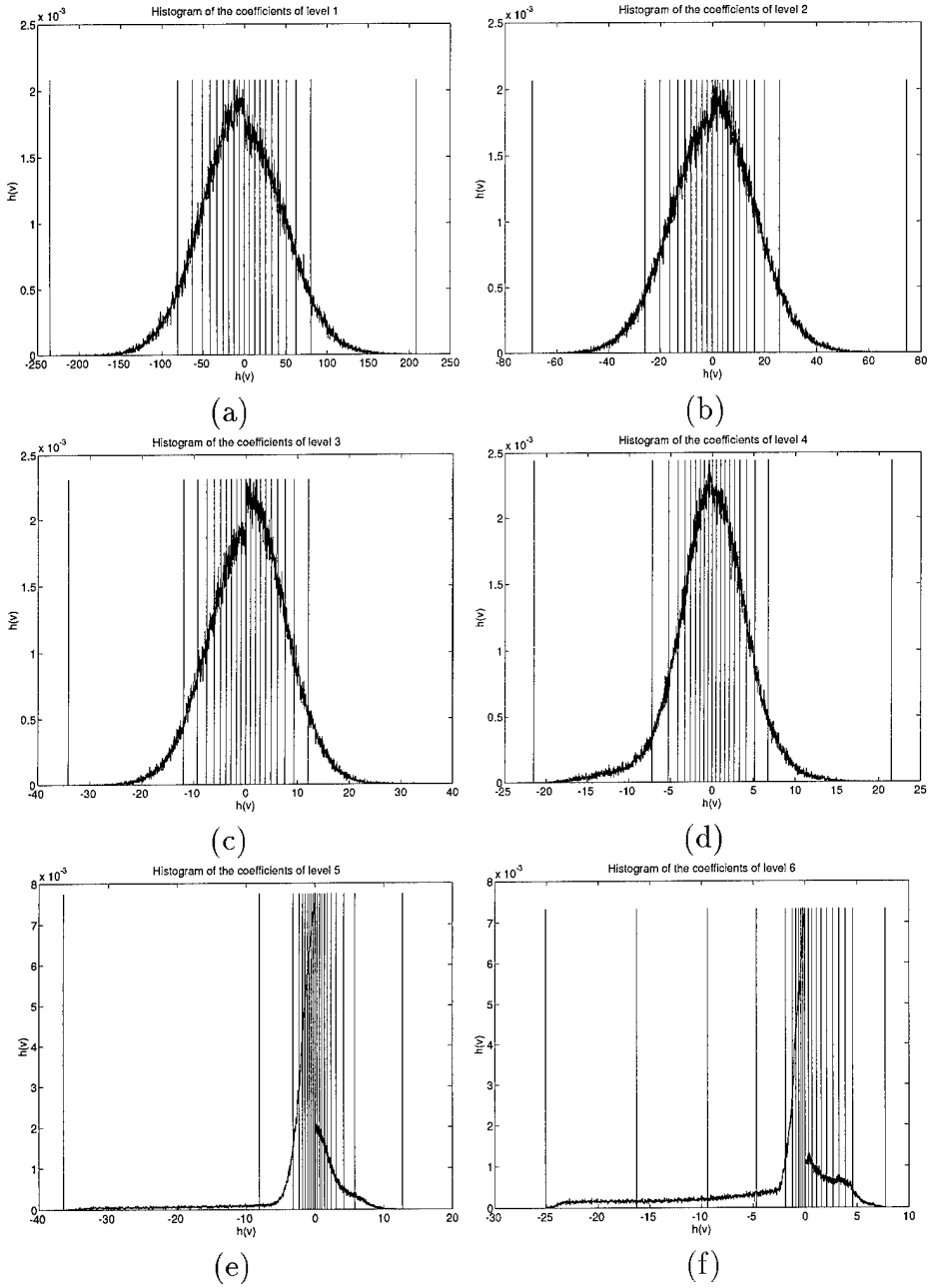

Figure 59: (a)–(f) Histograms of the wavelet coefficients of a phantom. The vertical lines indicate the thresholds from 0 % (thick line) to 100%.

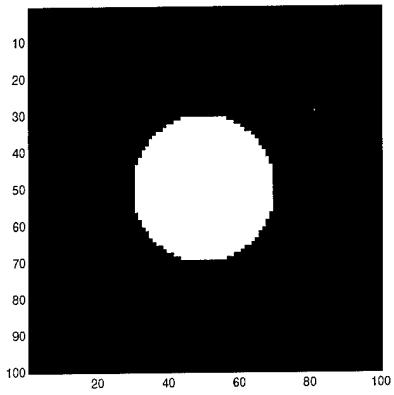

Figure 60: An image I is defined in the rectangular domain D. A mass m is defined in the domain D_m (white region). The area surrounding the domain D_m, $D - D_m$, is used for the calculation of the background B (black region).

2.6.3 Evaluation of Enhancement

In this Section we describe our methodology for quantitative and qualitative evaluation. A discussion of the relation between the Enhancement Factor EF, and the performance of an observer has been presented in a previous publication [63].

Enhancement Factor

The mean signal contrast, C, in each simulated mass was defined as:

$$C = \frac{\int_{D_m} S dA}{\int_{D_m} dA} - \frac{\int_{D-D_m} S dA}{\int_{D-D_m} dA} \tag{109}$$

where S is the original signal and dA is the area differential. D_m is the area where the signal (mass) resides, $D - D_m$ is the area that surrounds the mass and D is the area of the square. For the calculation of C we used the following formula [74]:

$$C = \frac{1}{13} \sum_{j=1}^{13} \left(\frac{S_j}{\pi r^2} - \frac{B_j}{100^2 - \pi r^2} \right) \tag{110}$$

where S_j is the gross count in the j–th square in the area where the signal resided (D_m) and B_j was the gross count in the same square where the S_j was calculated but for the area that surrounds the simulated mass (see Figure 60). Equation 110 is a discretized version of Equation 109. The summation considers the blocks that contain a mass.

An estimation of the noise N, in the image is provided by the following formula:

$$N = \sqrt{\frac{1}{12} \sum_{j=1}^{12} \sigma_j^2} \tag{111}$$

where σ_j is the standard deviation in the square where no signal resides. The summation for that case considers the blocks that contain only noise.

These definitions for contrast and noise were used to obtain the input contrast to noise ratio (CNR_i) and the corresponding value of the output contrast to noise ratio (CNR_o) in the processed image. The resultant enhancement factor, EF, is given by the expression:

$$EF = \frac{CNR_o}{CNR_i} = \frac{(C/N)_o}{(C/N)_i}. \tag{112}$$

Psychophysics Evaluations

The performance of the mass enhancement algorithm was evaluated through psychophysical experiments. The phychophysical technique used for the evaluation of the improvement of the visibility was the two-alternative forced choice (2AFC) measurement. Recent results suggest that the alternative forced choice (AFC) techniques are superior when the experimental conditions can be precisely controled using synthetic computer-generated images or images produced with phantoms and diagnostic equipment [75]. The 2AFC method was adopted, instead of the 4AFC (which according to Burgess [75] is the best choice), because of its simplicity and its reduced computational and storage costs.

In this method a radiologist was given two images of size 128 by 128 pixels. The noise in both images was normal and of the same variance. One of the two images was assigned a mass of known intensity, shape and size. The two images had equal probabilities of being assigned the mass. A reference image, indicating the correct position, shape and strength of the mass in a noiseless background was present to assist the radiologist in his task of locating the mass.

The same process was repeated for both the original and processed images. Eight point *CNR*s were selected and for each point 100 images were reviewed. The radiologist used a mouse to indicate his preference on the right or left image. For each point the proportion of the correct responses, was calculated and plotted as a function of the *CNR*. For the evaluation of the processed image we generated images, one with a mass and noise and the other with only noise. Both images were processed using the threshold algorithm and presented as the two alternatives to the radiologist.

Figure 61 shows the graphical user interface built for the 2AFC experiments. The top row contains the two images (left and right) the radiologist is forced to choose from. In the middle row (on the right side) one can see the reference image containing the noiseless mass (reference image). This image refreshes the radiologist's memory about the shape, size and position of the simulated mass. On the left corner there is the control panel. It

contains the buttons the radiologist has to click on in order to choose the left or the right image, a counter showing the number of the image and a button he/she can use if he/she wants to review a previous image.

2.6.4 Results

Choosing Optimized Thresholds

Our task was to choose the threshold values for each level in such a way that we obtained best possible improvement in visibility. As a measure of improvement we used the EF described earlier. In order to obtain this optimum choice we relied on an empirical study of the variation of the EF with the choice of the threshold value for each level.

In order to reduce the computational complexity we grouped the six decomposition levels into three groups:

Group 1 (high decomposition levels): Levels 1 and 2. This group contained noise and the fine details of the image.

Group 2 (medium decomposition levels): Levels 3 and 4. This group contained a mixture of noise and signal.

Group 3 (low decomposition levels): Levels 5 and 6. This group contained mainly pure signal.

Our study was performed in two stages. First we studied the effects of the threshold levels of each group and then we concentrated on the areas and levels we found most important and performed a more detailed study. In the first part of our study eleven threshold levels were chosen, thresholding at 0 %, 10 %,..., 100 % percent of the coefficients for that level. The EF was plotted as a mesh as a function of the thresholds of two groups. This was performed for all combinations. Results from the first part of our study are presented in Figure 62. These results suggested that only a very small percentage of the wavelet coefficients of the high levels should not be thresholded. Therefore we concentrated in the area of threshold values from 90 % to 100 %. Figure 63 shows the plot of the EF as a function of the threshold values for Groups 1 and 3. It is obvious that even if 1 % of the wavelet coefficients survives the thresholding there is no significant improvement on the EF. We therefore concluded that all the wavelet coefficients of Levels 1 and 2 should be set to zero.

For groups 2 and 3 we pursued into a more detailed study to obtain an estimation of the optimized threshold values. For group 2 we concentrated on the area from 90 % to 100 % and found that an optimum choice depends heavily on the CNR. We therefore opted

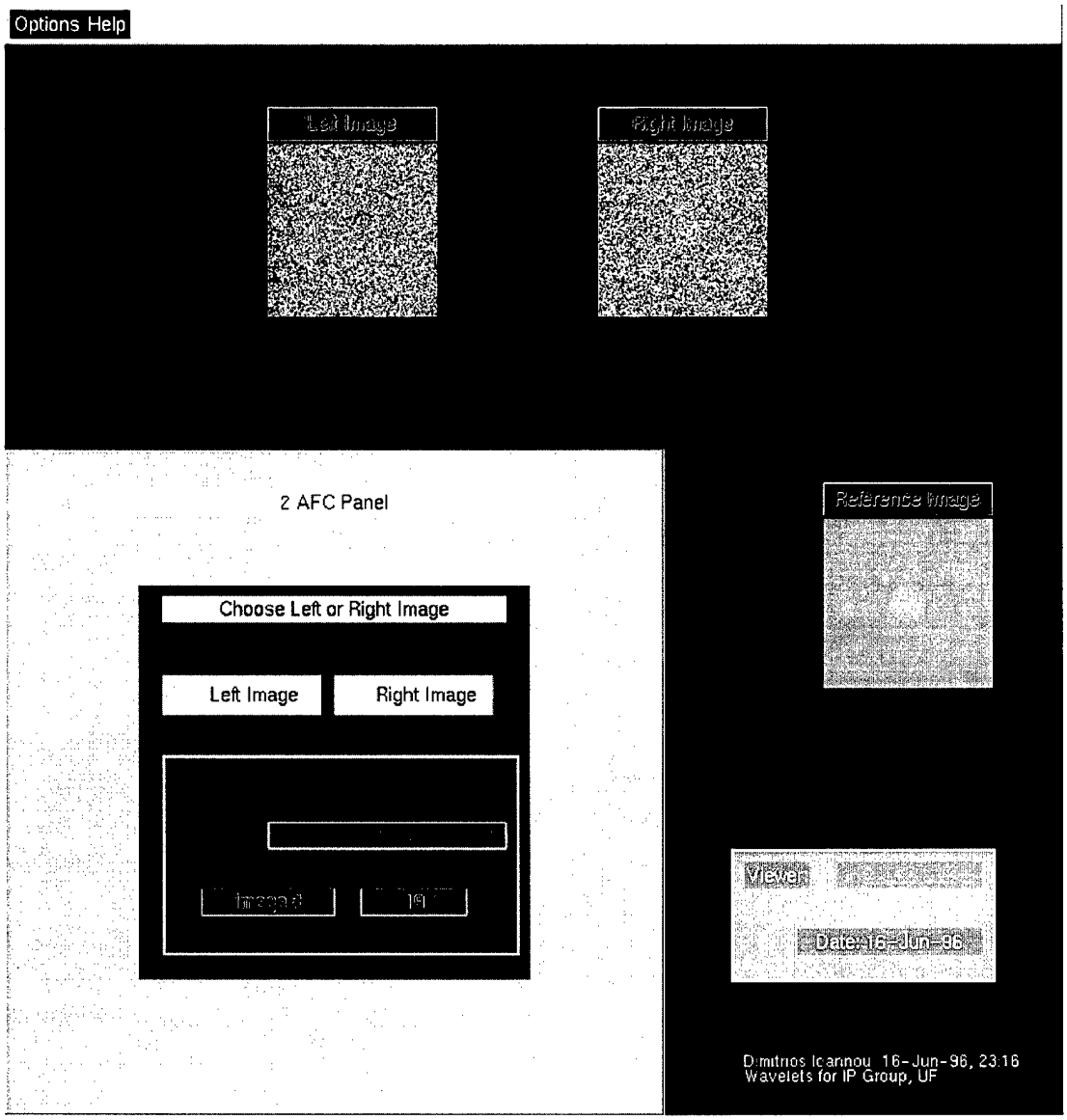

Figure 61: The graphical user interface used during the 2AFC experiments.

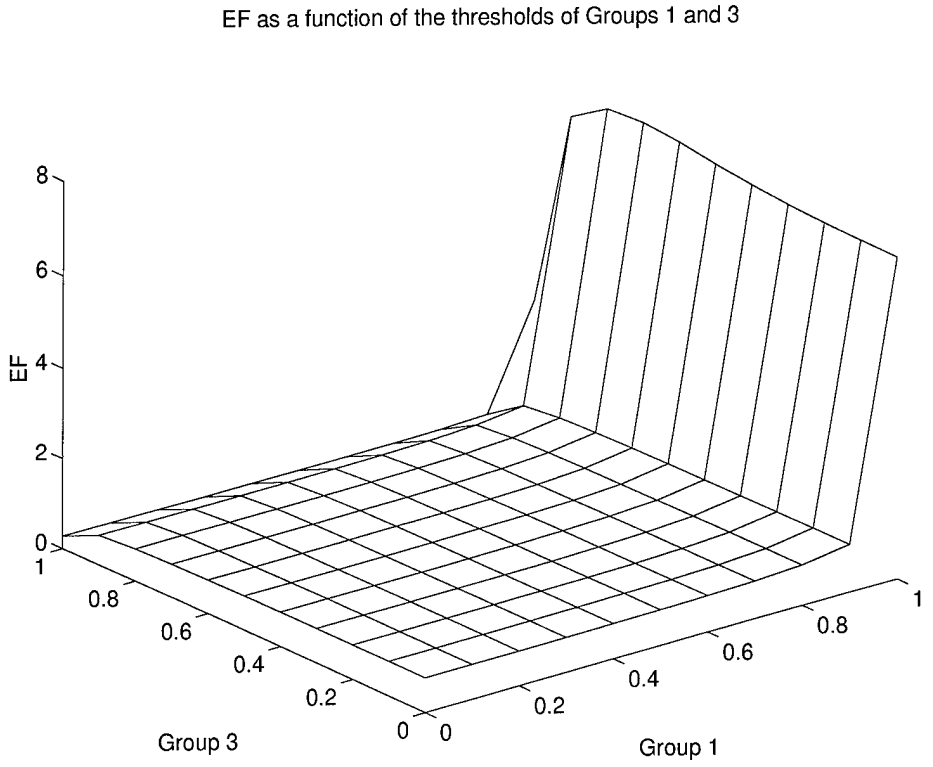

Figure 62: Plot of the *EF* as a function of the thresholds for Groups 1 and 3. The *EF* value increases dramaticaly for a threshold equal to 100 % for the levels of Group 1.

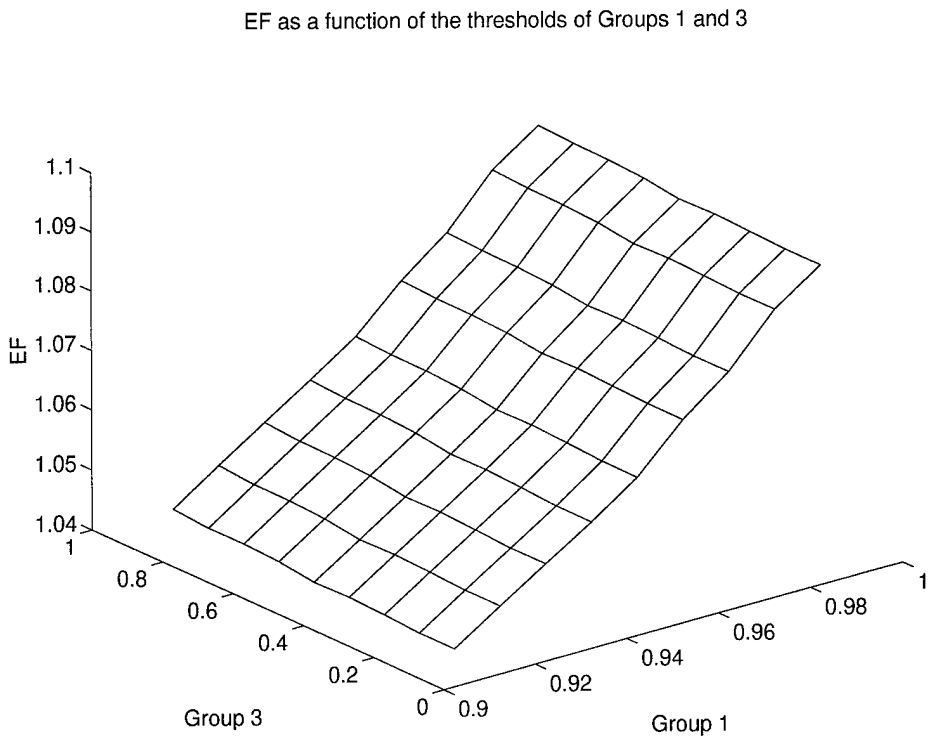

Figure 63: Plot of the *EF* as a function of the thresholds of Groups 1 and 3. For Group 1 we focused on the area from 91 % to 99 %. Notice that the increase of the *EF* is minimal.

for a conservative choice of the threshold and set 99 % of the coefficients of levels 3 and 4 equal to zero. After obtaining the optimized threshold values for Groups 1 and 2 we studied the effects of the choice of the threshold values of levels 5 and 6 seperately. Figure 64 (a) shows a plot of the *EF* as a function of the threshold values of Levels 5 and 6. Figures 64 (b)–(c) shows profiles of the same plot. In summary we found that the optimum choice of threshold values were: level 1: 100 %, level 2: 100 %, level 3: 99 %, level 4: 99 %, level 5: 87 %, level 6: 75 %. We point out that as it is obvious from Figure 64 that the improvement in *CNR* does not show a big variation with the choice of threshold value for Levels 5 and 6. Even if the threshold value for that level is not close to optimum, one would obtain a significant improvement in *CNR*.

Results on Simulated Masses

In this subsection the improvement of the visibility of masses in synthetic phantoms using the thresholding algorithm are presented. In Figure 65a an 128 by 128 pixel image containing a mass is shown. Figures 65 (c)–(h) show the coefficients that resulted from the wavelet decomposition of that image. The image presented in that figure was cropped from a 512 by 512 pixel simulated phantom. The image of the wavelet coefficients have been window-leveled for best display. The radius of the mass was equal to 15 pixels and the noise had a standard deviation equal to 10. The processed image is shown in Figure 65 (b). The resulting *CNR* was found to be equal to 28 (*EF*=39). Another example is presented in Figure 66 (a). The *CNR* of this image was 0.1, and was also cropped from a 512 by 512 pixel image. Figure 66 (b) shows the enhanced image. It is obvious that even in this extreme case there is a significant improvement in the visibility of the mass. For this case the *EF* was found to be equal to 25.

Psychophysics Experiments

The 2AFC method was used to evaluate the enhancement of the visibility of masses. The resulting True Positive Curves for a radiologist are plotted as function of the *CNR* (see Figure 67). We note that both True Positive Curves have a sigmoid shape starting from 100 %, for low *CNR*s (i.e., the radiologist is able to see everything) and ending, for high *CNR*s, to 50 % (i.e., the radiologist has no clue as to where the mass is and he randomly picks an image). We can clearly see that the transition region for all three radiologists has been shifted to higher *CNR*s. This indicates a real improvement in the visibility of the masses.

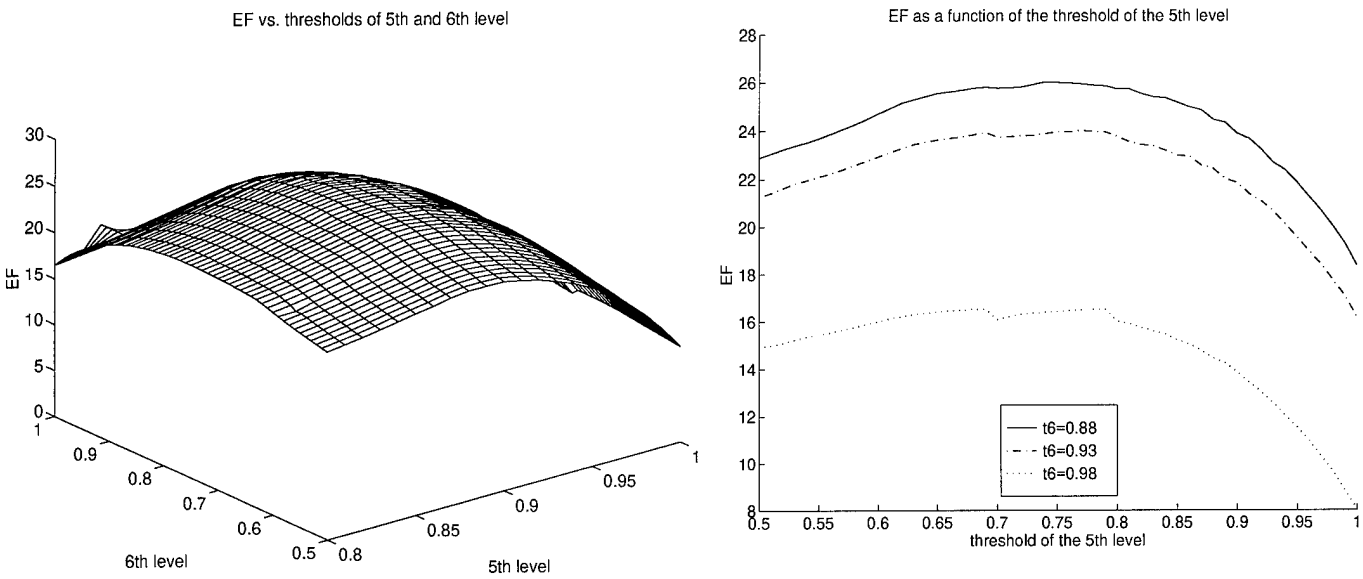

Figure 64: (a) A plot of the *EF* as a function of the thresholds of Level 5 and Level 6; (b) a plot of the *EF* as a function of the threshold of level 5 (profile of (a)); (c) a plot of the *EF* as a function of the threshold of level 6 (profile of (a)).

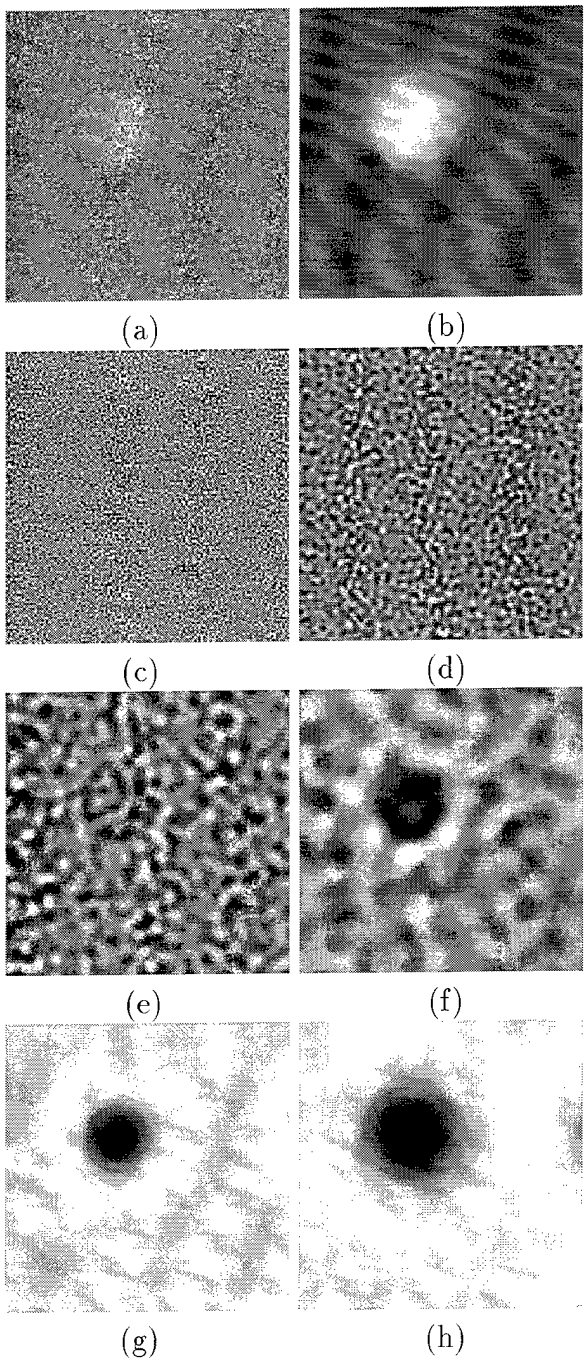

Figure 65: (a) Original image. (b) Processed image. (c)–(h) Six levels of wavelet decomposition.

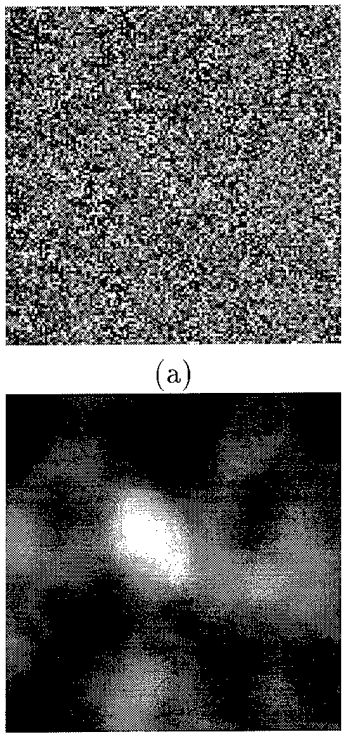

(a)

(b)

Figure 66: (a) A simulated phantom containing a mass. The *CNR* was 0.1. (b) The resulting image after the enhancement. The *CNR* was equal to 25.

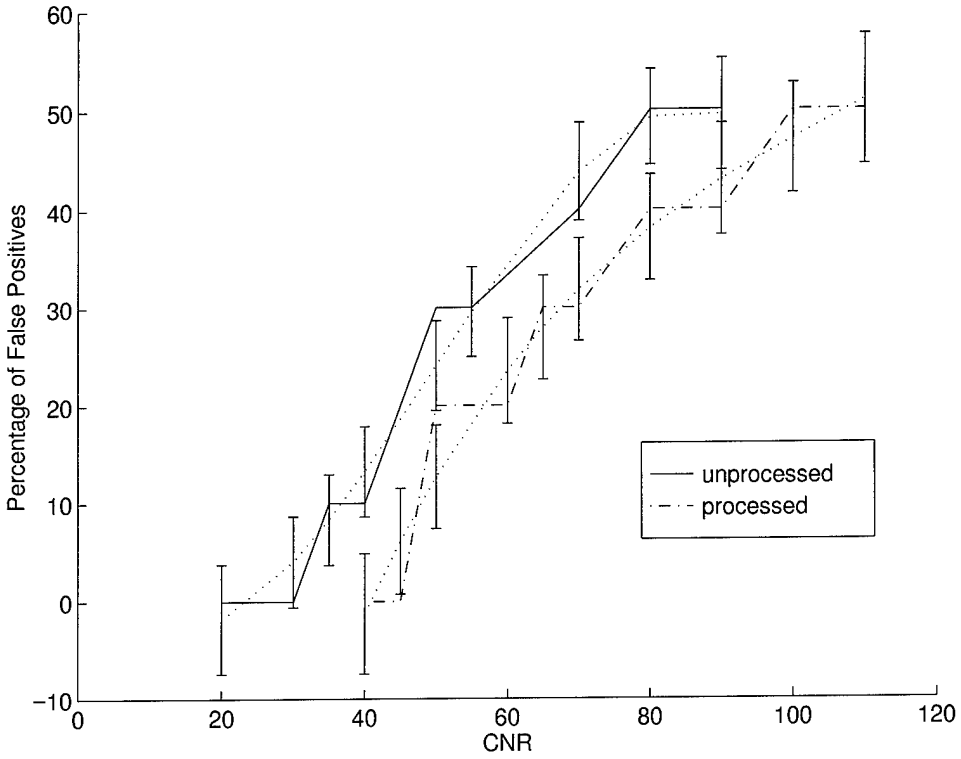

Figure 67: The ROC curves for a radiologist for unprocessed and processed images with the use of the wavelet thresholding method. The improvement on the visibility of the masses is obvious.

2.6.5 Summary

Substantial progress was made in the development of techniques to assist in the quantitative evaluation of wavelet based image processing algorithms. We showed that synthetic images can provide a useful tool towards benchmarking the effectiveness of multiscale enhancement algorithms. However the conclusions reached about the effectiveness of these methods largely depend on the realism of the synthetic data. Our method capitalized on our previous results to introduce a more realistic model of image formation. During the next year we plan to incorporate a model for the appearance of tissue, such as presented by Karssemeijer in his work for calcification detection in digital mammograms.

Finally, we reported on the development of objective ways to assess the performance of wavelet image processing algorithms. An important consideration in our enhancement algorithms was the selection of threshold values. We studied methods for estimation of an optimum threshold value and carried out an empirical threshold selection scheme. Our experiments showed that by deleting wavelet coefficients within the high frequency channels (e.g., levels 1 and 2) we achieved considerable improvement of the contrast to noise ratio. Aggressively thresholding wavelet coefficients within the lower spatial frequency channels had the effect of removing some of the features of the image (e.g., edges which appear exactly within these levels). It is therefore concluded that a more clever scheme is needed that will not threshold wavelet coefficients with respect to spatial locality but will use spatial/frequency information when modifying coefficients for denoising and enhancement.

3 Conclusions

During the past year, we have made significant progress in the development of a methodology for accomplishing adaptive contrast enhancement by multiscale representations. Our studies have demonstrated that features extracted from multiresolution representations can provide an adaptive mechanism for the local emphasis of salient and subtle features of importance to mammography. The improved contrast of mammographic features make these techniques appealing for computed aided diagnosis (CAD) and screening mammography. Screening mammography examinations are certain to grow substantially in the next few years, and analytic methods that can assist general radiologists in reading mammograms shall be of great importance.

In the paragraphs below, we summarize our progress and identify future directions of research to be carried out during the next year of our investigation.

We have described some underlying criteria to be followed when designing a database of digitized mammograms. Respecting these criteria we constructed a database of 105 abnormal cases (420 images) with a total of 118 biopsy proven masses. All cases were supplied by Shands Hospital at the University of Florida, an ACR accredited and FDA certified institution. Mammograms were digitized with a Lumiscan 75 scanner (Sunnyvale, California) at 116-micron pixel resolution, 12-bit gray scale resolution and optical density range of 0.05–3.00. All abnormalities were annotated hierarchically by a radiologist from Shands Hospital experienced in reading mammograms using an inhouse tool called `XMam` described previously in our 1994 annual report. Annotations include the location, shape, margins, density, size, surrounding glandular pattern, mammography finding and diagnosis based on the standardized American College of Radiology Breast Imaging Reporting and Data System. In addition, we developed a subjective evaluation of the detectability of a lesion and evaluated all lesions based on this scale. The current database consists of 78 malignant masses (66.1 %) and 40 benign masses (33.9 %) distributed according to subtlety as follows: 28.8 % obvious, 28 % relatively obvious, 25.4 % subtle, 14.4 % very subtle, and 3.4 % extremely subtle.

We computed the coefficients for filters of low order splines used as smoothing functions in a fast hierarchical digital filtering implementation of a discrete dyadic wavelet transform for both one and two-dimensional processing. A mirror extended input signal to a filter bank implementation of the discrete dyadic wavelet transform enabled us to take advantage of the symmetry/antisymmetry of both signals and filters for an efficient implementation of a dyadic transform. There are no restrictions on the size of the input signal which makes this scheme attractive for extracting arbitrary rectangular regions from digital

mammograms. The presented algorithm is iterative across scales: a noniterative scheme suitable for high speed (interactive) parallel processing can be derived easily by using the described approach on each dyadic scale independently.

We have shown the limitation of traditional discrete wavelet transforms (DWT) for characterizing band-limited features, including subtle findings in mammographic images. To more reliably isolate noise and identify features through scale space, we formulated and developed sub-octave wavelet transforms. If the number of sub-octave bands in each octave is a power of 2, we showed that the sub-octave wavelet transform of a function can be implemented by a single pair of analysis and synthesis wavelets. FIR filters for a class of wavelets designed for a DWT can be used to implement sub-octave wavelet analysis. A method of wavelet shrinkage for noise suppression was presented. An algorithm for the generalized case of adaptive gain processing was developed and shown to enhance features without amplifying noise. These efforts have significance in supporting interactive processing while yielding increased sensitivity of mammographic findings.

Our future efforts will include developing feature clustering techniques and carrying out statistical analysis of multiscale coefficients for more efficient removal of noise and enhancement of features. We will also explore iterative methods for identifying coherent structures of masses (selected from our mammographic database) that are persistent through scale space representations derived from our method of sub-octave wavelet analysis.

We have always advocated the use of linear phase filters for mammographic image processing and analysis. Such filters enable control over phase shifts and limit the introduction of artifacts during non-linear processing. By virtue of their symmetry (antisymmetry), complex Daubechies wavelets were designed to serve this advantage in image analysis.

We described a denoising algorithm based on complex Daubechies wavelets. The algorithm was aimed at removing noise while preserving mammographic features. We designed a simple method to classify waveform types and replaced wavelet coefficients of features with (mathematically) ideal waveform basis. The DC components of the analysis were modified using some unique properties of complex Daubechies wavelets.

We have shown that regions corresponding to masses can be identified reliably through frame representations of a continuous multiscale analysis. We showed that subtle features characteristic of mammographic findings required a finer parameterization of scale space than provided by traditional methods of wavelet analysis carried out at dyadic scales.

Basis functions for carrying out continuous multiscale analysis were designed to be symmetric and have zero-phase providing closed contour boundaries (via zero-crossings) of emergent features within each level of scale.

Spatial locality was preserved via a frame representation enabling segmentation of masses and adaptive contrast enhancement. We suggest that masses in dense mammograms can be reliably characterized and identified via geometric constraints (size and shape) within a best scale. This shall be pursued during the next year of research.

Substantial progress was made in the development of techniques to assist in the quantitative evaluation of wavelet based image processing algorithms. We showed that synthetic images can provide a useful tool towards benchmarking the effectiveness of multiscale enhancement algorithms. However the conclusions reached about the effectiveness of these methods largely depend on the realism of the synthetic data. Our method capitalized on our previous results to introduce a more realistic model of image formation. During the next year we plan to incorporate a model for the appearance of tissue, such as presented by Karssemeijer in his work for calcification detection in digital mammograms.

Finally, we reported on the development of objective ways to assess the performance of wavelet image processing algorithms. An important consideration in our enhancement algorithms was the selection of threshold values. We studied methods for estimation of an optimum threshold value and carried out an empirical threshold selection scheme. Our experiments showed that by deleting wavelet coefficients within the high frequency channels (e.g., levels 1 and 2) we achieved considerable improvement of the contrast to noise ratio. Aggressively thresholding wavelet coefficients within the lower spatial frequency channels had the effect of removing some of the features of the image (e.g., edges which appear exactly within these levels). It is therefore concluded that a more clever scheme is needed that will not threshold wavelet coefficients with respect to spatial locality but will use spatial/frequency information when modifying coefficients for denoising and enhancement.

These results are encouraging and continue to support that wavelet based image processing algorithms can play an important role in improving the imaging performance of digital mammography. In summary, we have exceeded the goals as described in our Task III and Task IV Statement of Work for and our research and development plans remain on schedule.

References

[1] A. G. Haus and M. J. Yaffe, Eds., *A categorical course in physics: technical aspects of breast imaging*, 79th Scientific Assembly and Annual Meeting of the Radiological Society of North America (RSNA), Oak Brook, IL, 1993.

[2] S. A. Feig and R. E. Hendrick, "Risk, benefit and controversy in mammographic screening", in *A categorical course in physics: technical aspects of breast imaging*, A. G. Haus and M. J. Yaffe, Eds. 79^{th} Scientific Assembly and Annual Meeting of the Radiological Society of North America (RSNA), 1993, pp. 119–135.

[3] R. A. Smith, "Epidemiology of breast cancer", in *A categorical course in physics. Technical aspects of breast imaging*, A. G. Haus and M. J. Yaffe, Eds. 79^{th} Scientific Assembly and Annual Meeting of the Radiological Society of North America (RSNA), 1993, pp. 21–33.

[4] G. T. Barnes and G. D. Frey, Eds., *Screen film mammography. Imaging considerations and medical physics responsibilities*, Madison, Wisconsin, 1991. Medical Physics Publishing.

[5] P. C. Johns and M. J. Yaffe, "X-ray characterization of normal and neoplastic breast tissues", *Physics in Medicine and Biology*, vol. 32, no. 6, pp. 675–695, 1987.

[6] M. J. Yaffe, R. J. Jennings, R. Fahrig, and T. R. Fewell, "X-ray spectral considerations for mammography", in *A categorical course in physics: technical aspects of breast imaging*, A. G. Haus and M. J. Yaffe, Eds. 79^{th} Scientific Assembly and Annual Meeting of the Radiological Society of North America (RSNA), 1993, pp. 63–72.

[7] I. Brodie and R. A. Gutcheck, "Radiographic information theory and application to mammography", *Medical Physics*, vol. 9, 1982.

[8] T. N. Wiesel, "Postnatal development of the visual cortex and the influence of environment", *Nature*, vol. 299, no. 5883, pp. 583–591, 1982.

[9] A. F. Laine, S. Schuler, J. Fan, and W. Huda, "Mammographic feature enhancement by multiscale analysis", *IEEE Transactions on Medical Imaging*, vol. 13, no. 4, pp. 725–740, 1994.

[10] A. Laine, J. Fan, and S. Schuler, "A framework for contrast enhancement by dyadic wavelet analysis", in *Digital Mammography*, A. G. Gale, S. M. Astley, D. R. Dance, and A. Y. Cairns, Eds., Amsterdam, The Netherlands, 1994, pp. 91–100, Elsevier.

[11] A. Laine, J. Fan, and W. Yang, "Wavelets for contrast enhancement of digital mammography", *IEEE Engineering in Medicine and Biology Magazine*, vol. 14, no. 5, pp. 536–550, 1995.

[12] J. Fan and A. Laine, "Multiscale contrast enhancement and denoising in digital radiographs", in *Wavelets in Medicine and Biology*, A. Aldroubi and M. Unser, Eds., Boca Raton, Florida, 1996, pp. 163–189, CRC Press.

[13] S. Mallat and S. Zhong, "Characterization of signals from multiscale edges", *IEEE Transactions on Pattern Analysis and Machine Intelligence*, vol. 14, no. 7, pp. 710–732, 1992.

[14] C. Kimme-Smith, "Clinical considerations for a mammography database", in *Biomedical Image Processing and Biomedical Visualization,* Proceedings of SPIE, San Jose, CA, 1993, vol. 1905, pp. 546–547.

[15] R. Rangayyan, R. Paranjape, L. Shen, and J.E. Leo Desautels', "Design of a common database for research in mammogram image analysis", in *Biomedical Image Processing and Biomedical Visualization,* Proceedings of SPIE, San Jose, CA, 1993, vol. 1905, pp. 550–551.

[16] R. Nishikawa, "Design of a common database for research in mammogram image analysis", in *Biomedical Image Processing and Biomedical Visualization,* Proceedings of SPIE, San Jose, CA, 1993, vol. 1905, pp. 548–549.

[17] D.R. Dance, "Design of a common database for research in mammogram image analysis", in *Biomedical Image Processing and Biomedical Visualization,* Proceedings of SPIE, San Jose, CA, 1993, vol. 1905, pp. 538–539.

[18] N. Karssemeijer, "A common database for research in mammographic image analysis", in *Biomedical Image Processing and Biomedical Visualization,* Proceedings of SPIE, San Jose, CA, 1993, vol. 1905, pp. 542–543.

[19] S. Astley, "Creating a database of digital mammograms", in *Biomedical Image Processing and Biomedical Visualization,* Proceedings of SPIE, San Jose, CA, 1993, vol. 1905, pp. 535–537.

[20] D.E. Powell and C.B. Stelling, *The Diagnosis and Detection of Breast Disease*, Mosby, St. Louis, MO, 1994.

[21] P. Kegelmeyer, "The importance of shared language for performance metrics", in *Biomedical Image Processing and Biomedical Visualization,* Proceedings of SPIE, San Jose, CA, 1993, vol. 1905, pp. 544–545.

[22] R. R. Coifman and M. V. Wickerhauser, "Entropy-based algorithms for best basis selection", *IEEE Transactions on Information Theory*, vol. 38, no. 2, pp. 713–718, 1992.

[23] B. Jawerth and W. Sweldens, "Overview of wavelet based multiresolution analyses", *SIAM Review*, vol. 36, no. 3, pp. 377–412, 1994.

[24] S. Mallat and W. L. Hwang, "Singularity detection and processing with wavelets", *IEEE Transactions on Information Theory*, vol. 38, no. 2, pp. 617–643, 1992.

[25] I. Koren and A. Laine, "A discrete dyadic wavelet transform for multidimensional feature analysis", in *Time-Frequency and Wavelets in Biomedical Engineering.* To appear, IEEE Press.

[26] I. Daubechies, *Ten Lectures on Wavelets*, Number 61 in CBMS-NSF Series in Applied Mathematics. SIAM, Philadelphia, Pennsylvania, 1992.

[27] M. Holschneider, R. Kronland-Martinet, J. Morlet, and Ph. Tchamitchian, "A real-time algorithm for signal analysis with the help of the wavelet transform", in *Wavelets, Time-Frequency Methods and Phase Space*, J. M. Combes, A. Grossmann, and Ph. Tchamitchian, Eds., Berlin, Germany, 1989, pp. 286–297, Springer-Verlag.

[28] A. V. Oppenheim and R. W. Schafer, *Discrete-Time Signal Processing*, Prentice-Hall, Englewood Cliffs, New Jersey, 1989.

[29] O. Rioul and P. Duhamel, "Fast algorithms for discrete and continuous wavelet transforms", *IEEE Transactions on Information Theory*, vol. 38, no. 2, pp. 569–586, 1992.

[30] J. Lim, *Two-Dimensional Signal and Image Processing*, Prentice-Hall, Englewood Cliffs, NJ, 1990.

[31] I. Daubechies, "Orthonormal bases of compactly supported wavelets", *Communications in Pure and Applied Mathematics*, vol. 41, no. 7, pp. 909–996, 1988.

[32] I. Daubechies, "Orthonormal bases of compactly supported wavelets II. Variations on a theme", *SIAM Journal on Mathematical Analysis*, vol. 24, no. 2, pp. 499–519, 1993.

[33] C. K. Chui, *An Introduction to Wavelets*, Academic Press, Boston, MA, 1992.

[34] X. Zong, E. A. Geiser, A. F. Laine, and D. C. Wilson, "Homomorphic wavelet shrinkage and feature emphasis for speckle reduction and enhancement of echocardiographic images", in *Medical Imaging: Image Processing,* Proceedings of SPIE, Newport Beach, CA, 1996, vol. 2710, pp. 658–667.

[35] X. Zong, A. F. Laine, E. A. Geiser, and D. C. Wilson, "De-noising and contrast enhancement via wavelet shrinkage and nonlinear adaptive gain", in *Wavelet Applications III,* Proceedings of SPIE, Orlando, FL, 1996, vol. 2762, pp. 566–574.

[36] D. L. Donoho and I. M. Johnstone, "Ideal spatial adaptation via wavelet shrinkage", Technical Report 400, Department of Statistics, Stanford University, 1992.

[37] R. R. Coifman and D. L. Donoho, "Translation-invariant denoising", in *Wavelets and Statistics*, Anestis Antoniadis, Ed. To appear, Springer-Verlag.

[38] A. F. Laine and X. Zong, "A multiscale sub-octave wavelet transform for de-noising and enhancement", in *Wavelet Applications in Signal and Image Processing IV,* Proceedings of SPIE, Denver, CO, To appear, vol. 2825.

[39] M. Vetterli and J. Kovačević, *Wavelets and Subband Coding*, Prentice Hall, Englewood Cliffs, NJ, 1995.

[40] D. L. Donoho, "De-noising by soft-thresholding", Technical Report 409, Department of Statistics, Stanford University, 1992.

[41] D. L. Donoho and I. M. Johnstone, "Ideal denoising in an orthonormal basis chosen from a library of bases", Technical Report 461, Department of Statistics, Stanford University, 1994.

[42] S. Chen and D. L. Donoho, "Atomic decomposition by basis pursuit", Technical Report, Department of Statistics, Stanford University, 1995.

[43] R. R. Coifman and F. Majid, "Adapted waveform analysis and denoising", in *Progress in Wavelet Analysis and Applications*, Y. Meyer and S. Roques, Eds., B.P. 33, 91192 Gif-sur-Yvette Cedex, France, 1993, pp. 63–76, Editions Frontieres.

[44] J. Lu, J. B. Weaver, D. M. Healy Jr., and Y. Xu, "Noise reduction with multiscale edge representation and perceptual criteria", in *Proceedings of IEEE-SP International Symposium on Time-Frequency and Time-Scale Analysis*, Victoria, B.C., 1992, pp. 555–558.

[45] J. Lu and D. M. Healy Jr., "Contrast enhancement of medical images using multiscale edge representation", in *Wavelet Applications,* Proceedings of SPIE, Orlando, FL, 1994, vol. 2242, pp. 711–719.

[46] A. Laine, S. Song, J. Fan, W. Huda, J. Honeyman, and B. Steinbach, "Adaptive multiscale processing for contrast enhancement", in *Biomedical Image Processing and Biomedical Visualization,* Proceedings of SPIE, San Jose, CA, 1993, vol. 1905, pp. 521–532.

[47] W. Lawton, "Applications of complex valued wavelet transforms to subband decomposition", *IEEE Transactions on Signal Processing*, vol. 41, no. 12, pp. 3566–3568, 1993.

[48] J.-M. Lina and M. Marrand, "Parameterizations of Daubechies wavelets", *Physical Review E*, vol. 48, no. 6, pp. 4160–4163, 1993.

[49] J.-M. Lina and M. Marrand, "Complex Daubechies wavelets", Technical Report, PHYSNUM-ANS-15, University of Montreal, 1993.

[50] Y. Meyer, *Wavelets and operators*, Cambridge University Press, New York, NY, 1992.

[51] S. Mallat and Z. Zhang, "Matching pursuits with time–frequency dictionaries", *IEEE Transactions on Information Theory*, vol. 41, no. 12, pp. 3397–3415, 1993.

[52] R. R. Coifman and M. V. Wickerhauser, *Wavelets and adapted waveform analysis*, Wavelets: Mathematics and Applications, Studies in Advanced Mathematics CRC Press, Boca Raton FL, 1992.

[53] W. T. Freeman and E. H. Adelson, "The design and use of steerable filters", *IEEE Transactions on Pattern Analysis and Machine Intelligence*, vol. 13, no. 9, pp. 891–906, 1991.

[54] E. P. Simoncelli, W. T. Freeman, E. H. Adelson, and D. J. Heeger, "Shiftable multiscale transforms", *IEEE Transactions on Information Theory*, vol. 38, no. 2, pp. 587–607, 1992.

[55] M. Antonini, M. Barlaud, P. Mathieu, and I. Daubechies, "Image coding using wavelet transform", *IEEE Transactions on Image Processing*, vol. 1, no. 2, pp. 205–220, 1992.

[56] S. Mallat, "A theory for multiresolution signal decomposition: the wavelet representation", *IEEE Transactions on Pattern Analysis and Machine Intelligence*, vol. 11, no. 7, pp. 674–693, 1989.

[57] M. J. Shensa, "The discrete wavelet transform: wedding the à trous and Mallat algorithm", *IEEE Transactions on Signal Processing*, vol. 40, no. 10, pp. 2464–2482, 1992.

[58] H. B. Barlow, "Pattern recognition and the responses of sensory neurons", *Annals of New York Academy of Sciences*, vol. 156, pp. 872–881, 1969.

[59] R. Shapley, R. C. Reid, and R. Soodak, "Spatiotemporal receptive fields and direction selectivity", in *Computational Models of Visual Processing*, M. S. Landy and J. A. Movshon, Eds., Cambridge, MA, 1991, pp. 109–118, MIT Press.

[60] D. Marr and E. C. Hildreth, "Theory of edge detection", *Proceedings of the Royal Society of London*, vol. 207, pp. 187–217, 1980.

[61] A. Witkin, "Scale space filtering", in *Proceedings of the International Joint Conference on Artificial Intelligence*, Karlsruhe, Germany,, 1983, pp. 1019–1022.

[62] M. Unser, A. Aldroubi, and S. J. Schiff, "Fast implementation of the continuous wavelet transform with integer scales", *IEEE Transactions on Signal Processing*, vol. 42, no. 12, pp. 723–736, 1994.

[63] Y. Xing, W. Huda, A. F. Laine, and J. Fan, "Simulated phantom images for optimizing wavelet-based image processing algorithms in mammography", in *Mathematical Methods in Medical Imaging III,* Proceedings of SPIE, San Diego, CA, 1994, vol. 2299, pp. 207–217.

[64] A. F. Laine, W. Huda, B. G. Steinbach, and J. C. Honeyman, "Mammographic image processing using wavelet processing techniques", *European Radiology*, vol. 5, pp. 518–523, 1995.

[65] J. L. Marroquin, "Probabilistic solution of inverse problems", Technical Report, MIT Artificial Intelligence Laboratory, AI Memo No. 860, 1987.

[66] R. Szeliski, *Bayesian modeling of uncertainty in low-level vision*, Kluwer Academic Publishers, Boston, MA, 1989.

[67] D. J. C. MacKay, "Bayesian interpolation", Unpublished Memo, 1991.

[68] J. Morlet and A. Grossmann, "Decomposition of hardy function into square integrable wavelets of constant shape", *SIAM Journal on Mathematical analysis*, vol. 15, no. 4, pp. 723–736, 1984.

[69] A. G. Haus and M. J. Yaffe, Eds., *A categorical course in physics: technical aspects of breast imaging*, 80th Scientific Assembly and Annual Meeting of the Radiological Society of North America (RSNA), Oak Brook, IL, 3rd edition, 1994.

[70] M. J. Yaffe, "Digital mammography", in *Syllabus: A Categorical Course in Physics*, 1994, pp. 275–286.

[71] H. E. Johns and J. R. Cunningham, *The Physics of Radiology*, C. C. Thomas, Springfield, IL, 1983.

[72] G. T. Barnes, "Mammography equipment: compression, scatter control, and automatic exposure control", in *Syllabus: A Categorical Course in Physics*, 1994, pp. 75–84.

[73] H. H. Barrett and W. Swindell, *Radiological Imaging*, Academic Press, New York, 1981.

[74] G. W. Snedecor and W. G. Cochran, *Statistical Methods*, The Iowa State University Press, Ames, IA, 1982.

[75] A. E. Burgess, "Comparison of receiver operating characteristics and forced choice observer performance measurement methods", *Medical Physics*, vol. 22, pp. 643–655, 1995.

[76] Z. Jing, Y. Zheng, W. Huda, A. F. Laine, J. Fan, and Y. Xing, "Quantitative evaluation of wavelet-based image processing algorithms", in *Wavelet Applications in Signal and Image Processing II,* Proceedings of SPIE, San Diego, CA, 1994, vol. 2303, pp. 569–578.

[77] N. Karssemeijer, "Stochastic model for automated detection of calcifications in digital mammograms", *Image and Vision Computing*, vol. 10, pp. 369–375, 1992.